Development of Novel Bioengineering Tools
for Investigating Cell Mechanotransduction in vitro

By

Weixi Zhong

A dissertation submitted in partial satisfaction of the

requirements of the degree of

Joint Doctor of Philosophy

with University of California, San Francisco

in

Bioengineering

in the

Graduate Division

of the

University of California, Berkeley

Committee in charge:

Professor Song Li, Co-Chair
Professor Gerard Marriott, Co-Chair
Professor Valerie Weaver
Professor Liwei Lin

Fall 2016

Development of Novel Bioengineering Tools
for Investigating Cell Mechanotransduction in vitro

Copyright © 2016

By

Weixi Zhong

Abstract

Development of Novel Bioengineering Tools
for Investigating Cell Mechanotransduction in vitro

By

Weixi Zhong

Doctor of Philosophy in Bioengineering

University of California, Berkeley

Professor Song Li, Co-Chair
Professor Gerard Marriott, Co-Chair

This dissertation presents research conducted on the design and development of three bioengineering tools for studying cell mechanotransduction on a live imaging platform, and for measuring response to stimuli in real time. These three tools are categorized in the following two areas: 1) dynamically tunable hydrogel substrate to probe cell behavior, and 2) fluorescent imaging markers to measure cell response to external stimuli.

Cells live in a complex environment filled with neighboring cells, biochemical signals, and the extracellular matrix (ECM). The ECM is not to be overlooked as simply a structure for cells to live and thrive on. It is a rich treasure trove of information, not only because it harbors a diverse array of chemokines and signaling molecules, but also for its own properties. The ECM provides mechanical cues to direct a variety of cellular behaviors. The study of mechanotransduction is, therefore, aimed at elucidating the biochemical and physical processes through which these mechanical cues are able to bring about certain cell responses.

Although the mechanotransduction of cells has been studied to some extend on a population level, we are only beginning to analyze these pathways on a single cell basis. Cell populations can be fairly heterogeneous, and study at the population level often misses the complexity and nuances of cellular response. Furthermore, treatments are often applied to elicit cell behavior hours, if not days, before a response is measured in a population of fixed cells. Cells, on the other hand, can respond to local events on the order of seconds. Without methodologies of study that correspond to this time scale, a lot of details are missed. As such, more imaging tools need to be developed to both probe and measure cell response to mechanical cues on a single cell level in real time.

In this dissertation, we aim to develop and characterize three bionegineering tools for real time live probing and response measurement on the time scale of seconds. NISO-crosslinked hydrogels allow for temporal, spatial, and magnitude control of stiffness change in the cell's own substrate. This system is easily incorporated into live imaging platforms, taking advantage of the commonly available 405nm laser line on many fluorescence microscopes to elicit the change in

1

the gel. With the use of confocal microscopy, precise spatial control over area of change is possible. While NISO provides a method of externally controlling the mechanical properties of the extracellular environment, the fLOV2-based fluorescent markers and nesprin tension sensor developed in the subsequent chapters provide further means to measure the response to such external stimuli. fLOV2 is a small plant-derived fluorescent protein, less than half the size of popular GFP-family proteins. Its small size and photophysical properties give it certain distinct advantages. Paired with mRuby2 as a FRET acceptor, the fLOV2/mRuby2 coupling rivals current FRET pairs in many aspects and its reduced size present opportunities for FRET sensors in which steric hindrance is of concern. The nesprin tension sensor aims to advance current understanding of mechanotransduction via physical pathways by directing the study into the nucleus. Together, this set of tools is a powerful kit for furthering understanding of the mechanisms of cell mechanotransduction.

Dedicated to my labmates.

Table of Contents

List of Figures

List of Tables

Acknowledgements

I have been exceedingly lucky to have the opportunity to do research in this university, in these two labs I have been a part of, and with these wonderful people who have been my companions and friends through the last five years of my graduate career. I would like to thank my research advisors Song Li and Gerard Marriott for their guidance and support over these years. Despite the different fields of study of these two labs, with the help of my two advisors I was able to find a niche of my own. It has led me to discover and learn about aspects of bioengineering I could never have hoped to approach on my own, and I am immensely glad of how much it has broadened my research horizons. I would also like to thank my qualifying exam committee members and my dissertation committee members: Professor Dave Schaffer, Professor Valerie Weaver, and Professor Liwei Lin. Their advice throughout this process have been invaluable in helping me pick my route through graduate school.

In academia, your lab is your family, and the Li and Marriott lab members have truly become like family to me. Thank you guys for making each in lab more than work. I would like to especially thank Chutima Petchprayoon and Alex Hoepker for teaching the basics for my research projects. I knew so little when I started each project and you were both so patient. I could not have learned this much without your solid foundation.

Finally, I'd like to thank my family and friends. My parents have always supported my interests and it was their gentle prodding that led me towards this path. They are a doctor and a chemist, after all. Last but definitely not least, Swarnali, without your encouragement through the years, I could not have gotten this far. I'm rooting for you!

CHAPTER 1

Introduction

1.1 Motivation

Throughout development cells experience a variety of different physical environments, and these varying settings provide cues to guide cells in their regular functions. How cells sense and respond to these cues is a field of study all on its own. The study of cellular mechanotransduction has only become more complex as we learn more about the interactions between cells and their surroundings. From the attachment of integrins to the extracellular matrix, to the formation of actomyosin filbers and the increase in cytoskeletal contractility, the intracellular response is multifaceted and multi-tiered.

Decades of study have only begun to establish the role of mechanical cues in directing cell morphology, migration, differentiation, and even pathology.[1] Studies using cell stretching methods showed that cells are highly sensitive to physical change in their substrate. Neuronal cells can exhibit improved growth or head towards apoptosis depending on the rate and degree of stretch applied.[2,3] Mechanical stretch can lead 3T3 fibroblast to more firmly establish their footing by activating integrin to grow and stabilize focal adhesions.[4] Studies using Mesenchymal Stem Cells have shown that the static stiffness of the cell seeding substrate is able to direct cell fate down one of several lineages based on the specific stiffness.[5] Recent research has shown that surface morphology of the growth substrate can even aid in the reprogramming of induced pluripotent stem cells.[6]

As we delve deeper in the detailed mechanisms of force transmission into and across the cells, more specific and refined experimental tools are required to gain new understanding of each step in the mechanotransduction process. While we have learned a lot in the past several decades, much remains a mystery. The nucleus, specifically, remained a scarcely explored new frontier. The ability of data collecting methods and measurement platforms to provide quantitative results therefore becomes a bottleneck to further knowledge. In this dissertation, several tools for analyzing physical mechanisms of mechanotransduction are developed an analyzed.

1.2 Dissertation Outline

Each chapter of this thesis has focused on a different aspect of developing *in vitro* tools and platforms for investigating cellular mechanotransduction.

Chapter 2 applies a novel crosslinker's photoswitchable nature to synthesize cell culture matrices with temporally, spatially, and incrementally controlled stiffness change. NISO is a photoresponsive molecule that undergoes a conformation change upon excitation with near UV light. While its optical properties have been utilized in imaging, the mechanical properties as a result of its physical switch have not been previously explored. Here, we apply NISO to the crosslinking of hydrogels, developing a cell seeding surface capable of quickly changing

stiffness during live imaging for a study of real time cell response to small mechanical perturbations in its local environment.

Chapter 3 developes imaging applications for a plant-derived fluorescent protein, fLOV2. fLOV2 is much smaller than the GFP-family of fluorescent proteins in mass and provides the advantage of red-shifted emission and increased Stokes shift when compared to its close cousin iLOV. Here we attempt to establish fLOV2 as a valuable fluorescent marker for *in vitro* use. The bulk of the chapter looks into pairing fLOV2 with the GFP-family red fluorescent protein mRuby2 as a new FRET pair. The photophysical properties of fLOV2 makes it a competitive candidate even in a field with many new fluorescent protein mutants being developed each year. A brief exploration of fLOV2's potential in fluorescence anisotropy measurements further emphasize this small protein's versatility.

Chapter 4 looks into the development and characterization of a new tension sensor, aiming to direct mechanotransduction research into the nucleus. With nesprin selected as the tension bearing protein of choice, both a well established FRET pair (mTFP1/Venus) and the new FRET pair developed in chapter 3 are tested in their ability to measure the transmission of tension into the nucleus from the cytoskeleton.

1.3 References

1. Alberts, B., Johnson, A., Lewis, J., Raff, M., Roberts, K., & Walter, P. *Molecular Biology of the Cell.* Ed. 4. (Garland Science, 2002).

2. Smith, D. H., Wolf, J. A. & Meaney, D. F. A New Strategy to Produce Sustained Growth of Central Nervous System Axons: Continuous Mechanical Tension. *Tissue Eng.* 7, 131–9 (2001).

3. Morrison, B., Saatman, K. E., Meaney, D. F. & McIntosh, T. K. In vitro central nervous system models of mechanically induced trauma: a review. *J. Neurotrauma* 15, 911–928 (1998).

4. Katsumi, A., Naoe, T., Matsushita, T., Kaibuchi, K. & Schwartz, M. A. Integrin activation and matrix binding mediate cellular responses to mechanical stretch. *J. Biol. Chem.* 280, 16546–16549 (2005).

5. Tse, J. R. & Engler, A. J. Stiffness gradients mimicking in vivo tissue variation regulate mesenchymal stem cell fate. *PLoS One* 6, e15978 (2011).

6. Downing, T. L. et al. Biophysical regulation of epigenetic state and cell reprogramming. *Nat. Mater.* 12, 1–10 (2013).

CHAPTER 2

A Novel Dynamic Hydrogel For Studying Cellular Mechanotransduction

2.1 Dynamic Hydrogels in the Study of Mechanotransduction

Scientific understanding of cellular interaction with their surrounding environment is rapidly advancing, with recent research highlighting the importance of mechanical interactions between cells and their extracellular matrix (ECM).[1] Many studies have found substrate stiffness to be a key determinant in cell fate in both normal and pathological development. In general, cells have been found to behave differently on softer versus stiffer materials, with stronger attachment and faster migration elicited by stiffer substrates.[2-4] Furthermore, stem cell differentiation in vitro is highly regulated by substrate stiffness. Mesenchymal stem cells (MSC) differentiate into neurogenic, myogenic, and osteogenic lineages when cultured on soft (<1 kPa), intermediate (8-17 kPa), and stiff (25-40 kPa) substrates, respectively.[5,6] As a result of these findings, there is an increasing demand for the ability to better control and modify the mechanical properties of cell culture substrate in vitro. Hydrogels have emerged as a class of materials that allows the experimenter to define both the biochemical and physical properties of the microenvironment in which cells grow and interact, in a physiologically relevant range.[7]

Hydrogel use in cell culture began with static substrates with easily pre-defined mechanical properties. While an improvement over tissue culture polystyrene, static hydrogels do not recapitulate the changing environment in which cells reside *in vivo*. Without dynamic control of physical properties, it is difficult to observe cell response at the threshold of change, which is often a determinant stage in pathological states such as cancer development.[8] Many dynamic hydrogel systems have been designed to fulfill this need. Hydrogels have been developed with the ability to increase in stiffness through slow and continuous or photo-activated crosslinking.[9,10] Gels that decrease in stiffness have been made with proteolytic or photocleavable crosslinkers.[11,12] Additionally, gels that can revert between two states exist and respond to stimuli such as temperature and pH changes.[13,14] Although these gel systems have made great leaps in the dynamic control of hydrogel elasticity, a system that combines the advantages of all these gels with robustly reversible, repeatable, and finely controlled dynamic tuning will be exceptionally valuable in further understanding of cellular response to a constantly changing environment.

2.2 NISO

Spironaphthoxazine (NISO) is a photoresponsive compound capable of repeated rapid and reversible switching between spiro (SP) and merocyanine (MC) states under photostimulation (Figure 2.1).[15] The SP and MC states are isomers differing in both structural and optical properties. Because of this, NISO has been used as an optical switch probe in bioengineering applications such as protein interaction inhibition and high contrast optical lock-in detection imaging.[16,17] However, the mechanical change due to the structural differences between the SP

and MC states is previously unexplored. In the SP state, NISO is a set of rigid connected rings with zero degree of freedom to rotate. In the MC state, due to the opening of a central ring, the molecule becomes more flexible (Figure 2.1a). The reverse reaction switching from MC to SP state is favored and occurs on its own with a time constant of approximately 30 seconds. However, the reverse switch can be sped up using green light due to the new absorption peak in the MC state (Figure 2.1e). The change in absorption between the SP and MC states also provides a unique opportunity of monitoring NISO switch in real times. The new peak in the absorption spectrum results in a visible color change.

When functionalized with appropriate reactive groups on both ends, NISO can serve as a switchable crosslinker for a variety of polymer networks, allowing for stiffness change in the bulk material in response to photostimulation (Figure 2.1b-c). NISO-crosslinking holds the advantage over other dynamic hydrogels of combining fine spatial, temporal, and level control all in one. Reversibility and repeatability of photostimulation also provides the flexibility of creating a time-varying function of mechanical change within a single gel. In addition, optical regulation of mechanical property allows for easy integration of stimulus events into live-imaging platforms such as confocal microscopy for observation of both short and long timescale cellular behavior and response.

2.3 Materials and Methods

2.3.1 NISO Synthesis

Step 1 – Synthesis of 5-hydroxy-2,3,3-trimethyl-3H-indole (compound 1)

(1)
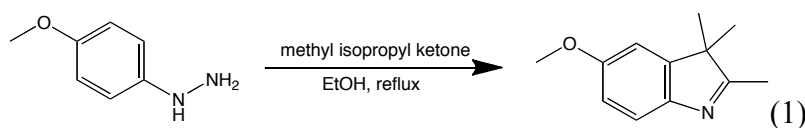
1 equivalent of (4-methoxy)-phenyl hydrazine hydrochloride was dissolved in absolute ethanol in a round reaction flask. While stirring, 1.1 equivalent of methyl isopropyl ketone was added by pipette. The reaction was heated to 90ºC under reflux for 5.5 hours to overnight under N_2 pressure. The reaction was cooled to room temperature before checking for product using thin layer chromatography (TLC).
The crude product was concentrated *in vacuo* and purified by column chromatography using 40-63um diameter silica gel with 60 Å pores. A gradient of solvents from 5:1 to 3:1 to 2:1 hexane:EtOAc was used to elute the product . Each collected fraction was checked by TLC for presence of product. Fractions containing product were combined and concentrated *in vacuo*. The product was desiccated under vacuum until mass was stable. Product was stable at room temperature and appeared as a reddish orange solid when dry.

Step 2 – Synthesis of 5-hydroxy-2,3,3-trimethyl-3H-indole (compound 2)

(2)
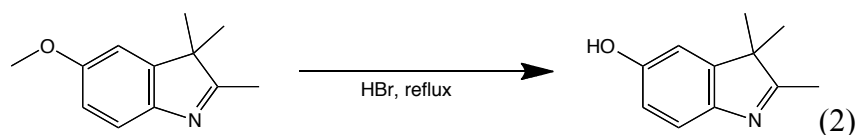
1 equivalent of 5-methoxy-2,3,3-trimethyl-3H-indole (compound 1) was dissolved in 30 equivalents of 48% aqueous hydrobromic acid. The reaction was heated to 140°C under reflux for 2 hours under N_2 pressure. After cooling for 20 minutes, the crude product was neutralized with saturated sodium bicarbonate to neutral pH while stirring. The neutralized solution was partitioned with dichloromethane in a separation funnel to extract product in aqueous phase. The product was further dried over sodium sulfate, filtered, checked using TLC, and finally dried *in vacuo* until mass stable. The product appeared as a brown solid.

Step 3 – Synthesis of 5-hydroxy-1,2,3,3-tetramethyl-3H-indolium iodide (compound 3)

(3)
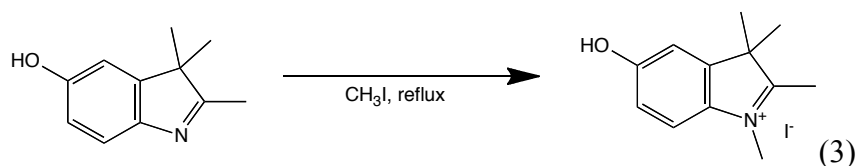
1 equivalent of 5-hydroxy-2,3,3-trimethyl-3H-indole (compound 2) was dissolved in dichloromethane and 8 equivalents of methyl iodide was added. The reaction was heated to 60°C under reflux and proceeded overnight under N_2 pressure. After overnight reaction, 1 volume of hexane was added to precipitate product, which was filtered and air dried. After transfer to scintillation vial, product was desiccated under vacuum until mass stable. Product was stable at room temperature once dried and appeared as a yellowish brown powder.

Step 4 – Synthesis of 1-nitroso-2,7-dihydroxynaphthalene (compound 4)

(4)
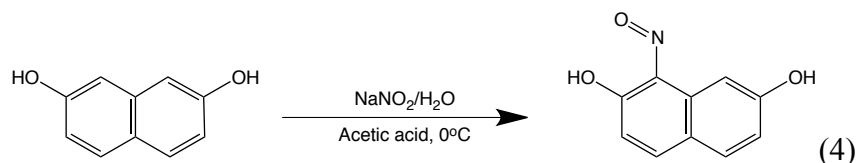
1 equivalent of 2,7-dihydroxynaphthalene was dissolved in glacial acetic acid and placed in an ice bath while stirring. 1 equivalent of sodium nitrite was dissolved in a minimal amount of water and added to 2,7-dihydroxynaphthalene solution dropwise. Water was added to the solution to a final ratio of 5:1 acetic acid:water. After stirring on ice for 10 minutes, a further 0.05 equivalent of aqueous sodium nitrite was added to the reaction. The reaction mixture was stirred on ice for 2 hours. 1 volume of water was added to the reaction, which was then filtered. The precipitate was washed with water and air dried. After transfer to scintillation vial, product was desiccated under vacuum until mass stable. Product appeared as a dark reddish brown powder.

Step 5 – Synthesis of NISO
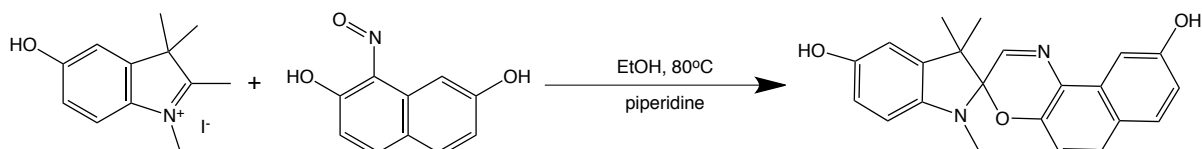
1 equivalent of 1-nitroso-2,7-dihydroxynaphthalene (compound 4) was dissolved in ethanol under stirring. 1 equivalent of 5-hydroxy-1,2,3,3-tetramethyl-3H-indolium iodide (compound 3) and 1 equivalent of piperidine were added directly to the ethanol solution while stirring. The reaction was heated to 80ºC under reflux and proceeded under N_2 pressure for 5 hours. The crude product was cooled and concentrated *in vacuo*, then purified by column chromatography using a 10:1 to 7:3 to 1:1 hexane:ethyl acetate solvent system. Each collected fraction was checked by TLC for presence of product. Fractions containing product were combined and concentrated *in vacuo*. The product was desiccated under vacuum until mass stable. The product appeared as a dark blue solid.

Step 6 – Synthesis of DA-NISO
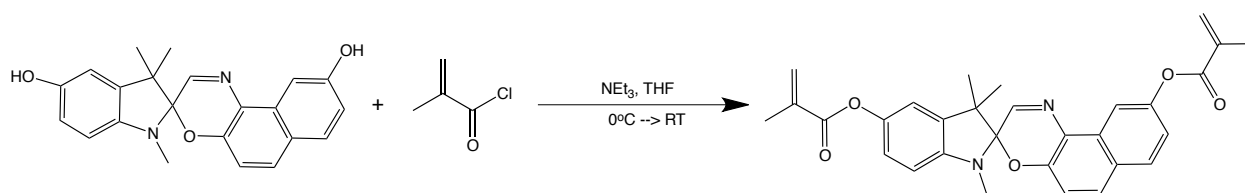
1 equivalent of NISO was dissolved in anhydrous tetrahydrofuran in an ice bath. 2.2 equivalents of triethylamine was added to the reaction and the atmosphere was flushed with nitrogen. After stirring for 5 minutes, a solution of methacryloyl chloride diluted in 1 volume of anhydrous tetrahydrofuran was added dropwise to the reaction. The reaction mixture was stirred on ice and allowed to warm to room temperature overnight. After overnight reaction, 1 volume of hexane was added and the mixture was filtered and the filtrate collected and concentrated *in vacuo*. The crude product was further purified by column chromatography using a 10:2 to 10:1 hexane:ethyl acetate solvent system. Each collected fraction was checked by TLC for presence of product. Fractions containing product were combined and concentrated *in vacuo*. The product was desiccated *in vacuo* until mass stable. The product appeared as a yellow viscous solid, with a molecular weight of 496 g/mol. The final product was verified by NMR.

After completion of synthesis, DA-NISO was aliquoted by dissolving in a small amount of acetone and distributing less than 5mg each to imcrocentrifuge tubes. Aliquots were then evaporated in a chemical fume hood to apparent dryness and placed under vacuum under mass was stable. The finished aliquots were stored at -20°C.

Maleimide-functionalized NISO (bis-maleimide-NISO, or BM-NISO), was synthesized in house courtesy of Chutima Petchprayoon.

2.3.2 NISO-Crosslinked Hydrogels

PEG-NISO
PEG-NISO hydrogels were made using multi-armed thiolated PEG of 10kDa and 2kDa molecular weight with either BM-NISO or linear PEGDA (250Da) as crosslinkers. The hydrogels were made in pH7 2mM Tris buffer between polylysine coated coverslips. Due to its

lower solubility in water, BM-NISO was first dissolved in a small amount of DMF. After gelation, the product was then washed in 1x PBS 3 times to remove DMF.

PMA-NISO

PMA-NISO gels were made in an aqueous emulsion free radical polymerization reaction. To 3.83mL of DI water was added, while stirring, 250µL pure methyl acrylate monomers in liquid form (5% by volume), 15mg of DA-NISO dissolved in 750µL of DMSO, 85µL of 0.1M potassium bromate (to a final concentration of 15mM), and 85µL of 0.45M sodium bisulfite (to a final concentration of 67.5mM). The reaction was stirred for 1 to 1.5 hours, during which the growing polymer appeared as a white solid and grew in mass over time. The precipitated polymer was removed from the aqueous solution and dried under vacuum. The polymer was then dissolved in a minimal volume of acetone and cast into rectangular molds in sheets. The molded polymer was air dried for 3 hours, then placed under vacuum overnight to fully remove solvent. Sheets of polymer are then cut into smaller strips for tensile testing. The control PMA gel was made similarly without NISO or with a molar equivalent of PEGDA instead of NISO. For 2xNISO gels, the above protocol was used with double the mass of NISO without increasing volume of DMSO.

PA-NISO

To make PA-NISO gel on glass-bottom cell culture dishes, the glass surfaces were first functionalized to facilitate gel attachment. Each dish is sonicated with a 70% ethanol solution for 30 minutes then blow dried with a compressed air line. The dishes were then treated with oxygen plasma and silanized within 5 minutes of treatment.

A silanization solution was made according to the following formula: 94% volume methanol, 5% volume DI water, final concentration of 5.7µM acetic acid, and 1% volume 3-(trimethoxysylyl)propyl methacrylate (TMSPMA). The silane solution without TMSPMA was made prior to oxygen plasma treatment. TMSPMA was added immediately after oxygen plasma treatment, and the solution was mixed and added to the glass bottom dish and incubated at room temperature for 5 minutes. Each dish was then washed 3 times with methanol and placed in an oven at 50°C for 4 hours to complete the silanization reaction. The dishes were cooled to room temperature before gel formation.

The coverslips used to form the top surface of gels were first coated with Gelslick to facilitate lifting off after the gel has formed. Briefly, a small droplet was placed on the surface of the coverslip and spread and wiped off using a kimwipe. This was done twice for each coverslip. Gelslick coating was always done immediately before making gels. Coverslips were recycled and reused by soaking in a 2N NaOH solution for 2 hours to remove coating, then rinsed quickly in DI water. The coverslips were then placed in 70% ethanol and sonicated for half an hour before being placed on a rack to air dry.

Silicon wafer chips used in micropatterning PA-NISO gels were passivated by vacuum silanization (see section 2.4.4). After each use, chips were soaked in DMSO to remove residues and observed under a reflective microscope for cleanliness. Silicon wafer chips with remaining residue were discarded. Attempts to clean with further steps were unsuccessful due to damaged features.

The volume of individual gel solution was calculated to match the area of coverslips (12mm diameter circular) and silicon wafer chips (10mm square) used to form the top surface in order to get a thickness of 70μm. PA-NISO hydrogels were made in DMSO due to DA-NISO's low solubility in water. PA-NISO gels were made using acrylamide monomers as the building blocks of the backbone of the polymer, bis-acrylamide or 250Da PEGDA as the primary crosslinker, and DA-NISO as a small portion of crosslinkers. PA gels were polymerized in a free-radical polymerization reaction using the photoinitiator 2-Hydroxy-4′-(2-hydroxyethoxy)-2-methylpropiophenone, from here on referred to by its previous proprietary name Irgacure 2959, as has been published.[18] In later samples, a different monomer, ACA (N-acryloyl-6-aminocaproic acid), was also included to enable surface modification via EDC (1-ethyl-3-(3-dimethylaminopropyl)carbodiimide hydrochloride) and sulfo-NHS (N-hydroxysulfosuccinimide). In control gels without NISO, bis-acrylamide or 250Da PEGDA were used as the only crosslinkers.

Specifically, PA-NISO hydrogels contained the following formula. Acrylamide monomer stock was made at 50% weight/volume in DMSO and stored at 4°C. Bis-acrylamide crosslinker stock was made at 25% weight/volume in DMSO and stored at 4°C. ACA monomer stock was made at 2M in DMSO and stored at 4°C. DA-NISO crosslinker stock was made at 400mM in DMSO and stored at -20°C for a maximum of 2 weeks before a new aliquot was made. Irgacure 2959 stock was made fresh each time at 10% weight/volume in DMSO. Gel mixes were made in varying ratios and labeled according to their formula. Irgacure 2959 was always used at a final concentration of 4% weight/volume. For example, a gel made with 10% acrylamide monomer, containing total crosslinker at a molar ratio of 20% of acrylamide monomer, with those crosslinkers divided into a ratio of 9:1 bis-acrylamide:DA-NISO is labeled as 10-20-9:1. The control gel made with only bis-acrylamide as crosslinker would be 10-20-B, and the same control gel made with PEDGA was labeled 10-20-P.

Get formulas were mixed at 10% excess volume and aliquoted to a PCR tube for every 2 gels. The PCR tubes were then placed in small scintillation vials with septum caps and nitrogen purged 5 times each through the septum. Nitrogen purged vials were protected from light and used within half an hour. For every two gels, the correct amount was carefully distributed to the center of a TMAPMA-treated and cooled down glass bottom dish and quickly covered with the Gelslick side of a coverslip or the feature side of a silicon wafer chip. The glass bottom dishes were then placed on top of a 365nm UV lamp facing up. The lamp was turned on for 5 minutes. The gels were allowed to finish reacting for a further 5 minutes before the coverslip or chip was lifted off.

After the coverslip or silicon wafer chip was removed, the gel was then washed 3 times with DMSO and 3 times with 1x PBS for 5 minutes each. Gels were immediately used or stored at 4°C overnight before surface modification and cell culture.

2.3.3 Mechanical Testing

Compressive and tensile testing of NISO-crosslinked gels were conducted using an ElectroForce 3200 mechanical testing machine by TA Instruments, courtesy of the shared Stem Cell Center at UC Berkeley.

Compressive testing
For compressive testing of PEG-NISO hydrogels, a 250g "small load" load cell was used. PEG-NISO hydrogels were loaded between flat plates with the load cell beneath the bottom plate. Hydrogels were placed on the bottom plate and the force load was zeroed. The top plate was lowered until force it registered, then slowly raised up back until force was once again zero. The height and diameter of the hydrogels were measured after loading. Excess PBS was added between the plates to prevent hydrogels from drying during test cycles. Gels were compressed to 90% of initial thickness over a period of 60 seconds. The absolute compression rate was different for each gel due to the variability in gel thickness. Gels were made to the approximate dimensions of 4mm in diameter and 2.5mm in height. Repeat compression cycles included 20 seconds of relaxation in between.

Tensile testing
For tensile testing of PMA-NISO gels, a 50lb "large load" load cell was used. PMA-NISO gels were loaded into grips, with the load cell located below the bottom grip (Figure 2.2b). The insides of the grips were padded with PDMS to prevent ripping of gels. Each gel was loaded first into the bottom grip and force load was zeroed. The top grip was opened and lowered until the gel reach between the two plates of the grip and tightened. The top grip was then slowly raised until the gel was straightened and force on the load cell read zero. The thickness and width of the gel strip were measured prior to loading. However, gel length was measured between the edges of the grips after loading for an accurate representation.

Each gel strip was then stretched by 10% of its initial load length over 10 seconds. The gel was allowed to relax for 50 seconds after each stretch for a total of 1 minute per cycle. Each gel underwent 30 cycles of stretch and relaxation, with the gel under a 395nm LED excitation during odd numbered cycles. On odd numbered cycles, the LED was turned on 10 seconds prior to the beginning of stretching to ensure NISO is in MC state for the entire duration of stretch. The LED was turned off at the end of stretching. The brightness of the LED was controlled by a power modulator and set to different levels for measurements of power-dependent NISO switching. The LED output at each power level was measured with a power meter. The Young's modulus was calculated for each individual cycle using a MATLAB program written by the author of this dissertation.

The Young's modulus was calculated using the displacement and force output data using the following equation, where E is the Young's modulus, σ_t is the true stress, and ε_t is the true strain.

$$E = \frac{\sigma_t}{\varepsilon_t}$$

Eqn. 1

The true stress was further defined by the following equation, where F is the force measured by the load cell, and A is the cross-sectional area of the gel at each data point, assuming there was no volume change as the gel is being stretched.

$$\sigma_t = \frac{F}{A}$$

<div align="right">Eqn. 2</div>

The true strain was defined by the following equation, where l_0 is the initial length of the gel and l is the current length of the gel at each data point.

$$\varepsilon_t = \ln\frac{l}{l_0}$$

<div align="right">Eqn. 3</div>

The stress-strain curve was first graphed to the elastic (i.e. linear) region of the curve. Since stretching was only done to 10%, the majority of gels remained within their elastic range throughout the duration of stretch. The Young's modulus was then calculated using the slope of the elastic region of the stress-strain curve.

AFM

Atomic force microscopy (AFM) was used to measure PA-NISO hydrogel stiffness. An MFP-2D AFM from Asylum Research was used for these measurements, courtesy of Professor Lydia Sohn in the Mechanical Engineering department at UC Berkeley. An AFM tip with a pyramid shaped silicon nitride probe was used for taking measurements. The spring constant of the cantilever was calculated to be 93pN/nm.

PA-NISO samples were prepared on glass coverslips, similarly to the protocol for glass bottom dishes, and soaked in PBS overnight prior to AFM testing. AFM measurements were conducted in water with the AFM tip submerged the entire time. For each set of 405nm excitation switch test, an external laser was used to activate a region of the gel approximately 3mm in diameter. Immediately after activation for 60 seconds, the AFM deflector was recalibrated to center the laser for measurement of the activated stiffness. After this measurement, the gel was observed for return to SP state by its color change before the non-activated measurement was taken. Between each measurement, the cantilever was moved so that the same spot was not measured. Although all the movements remained within the large area of photoactivation. Each measurement took 16 data points in a 4 by 4 square arrangement spread across a 10μm by 10μm square of the gel surface. Force-displacement data was fitted using the Hertz model on the IgorPro software provided with the AFM.

2.3.4 Patterning PA-NISO

Silicon wafer chips with microposts and microgrooves were prepared by photolithography methods in the Biomolecular Nanotechnology Center at UC Berkeley, courtesy of QB3, the California Institute for Quantitative Biosciences. Briefly, silicon wafers were cleaned with hydrofluoric acid prior to photolithography. SU-8 negative photoresist was poured onto the surface and spun until evenly distributed to the correct thickness. The wafer was then pre-baked at 65°C for 1 minute and 95°C for 3 minutes to prepare for UV exposure. The wafer was then exposed to UV through a photomask on an aligner. The transparent regions of the mask allow UV exposure of the SU-8 underneath, which then crosslinked to form the desired features. The exposed wafer was then baked once again at 65°C for 1 minute and 95°C for 3 minutes, during which time the features became visible to the naked eye. The wafer was then developed using an SU-8 developer, then washed with isopropanol. Finally, the wafer was heat dried to complete the process.

To passivate the surface of the SU-8, the wafer was treated to vapor silanization. The wafer was placed in a vacuum chamber with a few droplets of trimethylchlorosilane in an open vesicle for 15 minutes, the vacuum was turned off with the chamber remaining sealed for another 6 hours to ensure adequate and complete silane coverage of the wafer surface. Finished wafers were cut into 1cm square chips using a diamond tip glass cutter. Chips that have been used for gel molding were cleaned and resilanized for reuse.

2.3.5 Hydrogel Modifications for Cell Culture

PA gels were sterilized by soaking in 70% ethanol for 20 minutes in the cell culture hood. Each gel was then washed 3 times in 1x PBS. If necessary, gels can be sealed and stored in 4°C overnight at this step. Although longer storage without degradation is possible, it is not recommended.

The carboxyl groups on ACA monomers were activated using a combination of EDC and sulfo-NHS. A solution of 20mM EDC and 50mM sulfo-NHS in 100mM pH6 MES buffer was prepared fresh each time and sterile filtered using 20μm syringe filters. The sterile solution was then added to PA gels and incubated at room temperature for 30 minutes. Gels were quickly rinsed once with 1x PBS before the addition of fibronectin. Fibronectin from human plasma (Sigma Aldrich) was prepared at 200μg/mL and added at 100μL per gel. The fibronectin coating was incubated for 2 hours at 37°C. Prior to seeding of cells, fibronectin was rinsed off and fresh media was added to equilibrate the gel for 30-45 minutes at 37°C.

2.3.6 Cell Culture

NIH 3T3 fibroblast cells were maintained in growth medium (DMEM with 10% FBS and 1% penicillin/streptomycin) in sterile incubators set to 37°C with 5% carbon dioxide and controlled humidity. Cells were passaged every 2-3 days at approximately 75% confluence at a ratio of 1:20. Cells seeded onto PA-NISO hydrogels were passaged at 5,000 cells per glass bottom well in 35mm glass bottom wells with a 20mm diameter glass bottom.

PA-NISO toxicity study
To ensure that PA-NISO gels were not toxic to cells in culture conditions, an alamarBlue (ThermoFisher) cell health test was conducted to ensure normal metabolism in cells grown on PA-NISO gels.

PA-NISO and PA control gels were made immediately prior to toxicity tests. 3 gels each of NISO and control gels were used for each experimental condition, and another 3 wells of glass-only without any gel was also used as control. For photoexcitation, a 405nm LED lightbed was placed beneath a 24-well plate. The following conditions were used for the first experiment: power level 0, 1, 2, 5, and 10 for 10 continuous minutes. The light output was measured to be 0, 2, 4, 10, 20 mW/cm^2 for the 5 previously stated power levels. For the second experiment, the following 3 conditions were added, all at power level 5: 20 continuous minutes, 1 continuous hour, and 10 minutes of 10 seconds on and 90 seconds of cycles. For the third experiment, the 1 hour condition was removed due to its high toxicity.

Cells were seeded at 10,000 cells per well in a 24-well plate 24 hours prior to photoexcitation. AlamarBlue reagents were added at 24 hours after photoexcitation. In the first experiment, media was collected and read at the following times points: 1 hour, 2 hours, 6 hours, 26 hours. In the second and third experiments, media was collected and read at 18 hours. The media was read in a 96 well plate on a fluorescent plate reader for fluorescence using an excitation of 560nm and emission of 590nm, and for absorbance at 570nm. Statistical analysis was conducted using 2-way ANOVA with Bonferoni multiple comparisons test.

2.3.7 Confocal Imaging

Cells were imaged on a Zeiss LSM700 laser scanning confocal microscope with an incubation chamber set to 37°C and 5% carbon dioxide. Prior to imaging, the microscope was turned on and the incubation chamber was warmed up for half an hour both to prepare for cell health and to equilibrate objectives to 37°C. A 63x oil immersion objective and a 20x air objective were used for imaging of all samples. NISO activation on the microscope was achieved using a 405nm laser at 10% power. Brightfield images of PA-NISO hydrogels during NISO activation was collected using the 639nm laser line.

The 12 hour PA-NISO photoswitching was conducted using a 10-40-9:1 PA-NISO gel. The gel was excited with 405nm laser every 10 minutes for 12 hours.

2.4 Results and Discussion

NISO was synthesized with both maleimide and methacrylate end groups to react with a few different types of monomers and polymers. Bis-maleimide functionalized NISO (BM-NISO) is able to quickly and specifically react with sulfhydryl groups at neutral pH, allowing for controlled crosslinking of many commercially available polymers as well as peptides containing cysteines. At a more basic pH, maleimide is also able to react with primary amines.

Although methacrylate is the reactive functional end groups on the other NISO crosslinker, it was named di-acrylate NISO (DA-NISO) to emphasize its ability to be incorporated into acrylic polymers, including those made of monomers of acrylamide, methyl acrylate, and methyl methacrylate.

2.4.1 PEG-NISO Hydrogels

PEG hydrogels were initially used for ascertaining the ability of NISO to act as a dynamic crosslinker. PEG-NISO hydrogels were simpler and faster to make when compared to the other gels used. Preliminary mechanical testing used PEG-NISO hydrogels also suggest a decrease in compressive modulus after excitation with near-UV light. However, it was ultimated not used in cell experiments.

2.4.2 PMA Gels Display Switch-like Stiffness Change

PMA gels subject to repeated tensile stretch with and without 395nm LED excitation indicate that NISO indeed has an effect on polymer stiffness (Figures 2.2-2.5). 395nm is within the

excitation range of SP state of NISO and was expected to excite and switch NISO from SP state to MC state. However, there was initial concern that repeated excitation may affect the PMA polymer itself regardless of NISO presence due to photodamage. To ascertain that this was not the case and to show that NISO is capable of changing the bulk stiffness of the polymer it is used to crosslink, both PMA and PMA-NISO were tested under 395nm LED excitation.

Random selection and analysis of the stress-strain relationship of individual stretch tests showed that the 10% stretch did not go beyond the elastic region of the polymer, e.g. the slope of the stress-strain graph remained linear throughout the stretch test.

Test results show that PMA control gels do not change in tensile modulus whether the 395nm LED is on or off. When the LED power level was varied from 3.34 mW/cm^2 to 19.3 mW/cm^3, the modulatable range on this specific LED, the change in power did not affect the result (Figure 2.1a, Figure 2.2). When looking at the individual stretch cycles at each power level, there was no switching behavior at any power level and tensile modulus remained relatively steady for all trials through the entire trial (Figure 2.2).

PMA-NISO with 1x NISO and 2x NISO were also tested and both groups showed statistically significant decreases in bulk gel stiffness when excited with 395nm LED (Figures 2.2, 2.4, 2.5). Moreover, for both groups, as the LED power was increased the amount of stiffness change increased as well. This result was anticipated. The increase in LED power reflects a larger number of photons emitted. The number of photons hitting the sample is theoretically directly correlated to the percentage of total NISO molecules that will absorb and switch from SP to MC state. The more NISO molecules change from rigid SP conformation to the looser MC conformation, the more the stiffness should decrease in the bulk gel.

A detailed look at the individual stretch cycles show that, at higher LED power levels, the switch between SP and MC states is distinct and fairly reliable across all 30 stretch cycles. As LED power level lowered, however, the switching behavior became less stable. Although there is still visible change from stiff in SP state and soft in MC state and back, the amount of switch from cycle to cycle can vary quite a bit. On some cycles in the two lowest power levels, there was not any change at all (Figures 2.4, 2.5). Some of this variability could be attributed to the margin of error in the measurement method itself. However, it is logical to expect lower reliability along with less stiffness change as light output is decreased.

Even though all the gels in each group were made in the same batch reaction and distributed to individual gel casts, the gels displayed different base stiffness. This was true for PMA gels as well as PMA-NISO gels. This difference makes it difficult to assess the amount of stiffness change seen in PMA-NISO gels. Due to this complication, the stiffness change was evaluated as both absolute change in kPa as well as percent change of base stiffness (Figure 2.2 b,c). There is a fairly linear increase in stiffness change with increase in LED power using both methods. Interestingly, the 2x NISO samples did not show significantly higher change in stiffness compared to the 1x NISO sample despite having twice the amount of NISO molecules.

In addition, the 2x NISO sample showed a less linear relationship between LED power level and the degree of stiffness change. This may be due to complications in properly incorporating NISO into the polymer during polymerization. The 2x NISO samples may have surpassed the capacity of the specific aqueous emulsion reaction formula used to accommodate NISO, which is highly insoluble in water. It is possible that NISO in the 2x sample was not well distributed and perhaps not reacted into the bulk polymer on both ends. With one dangling end, there is no effect on stiffness from switching. In order to incorporate 2x NISO polymer, perhaps a new reaction scheme is required.

A solution polymerization scheme was briefly explored for both PMA and PMMA, incorporating DA-NISO. Benzene was used as the reaction solvent and AIBN (azobisisobutyronitrile) was used as the free radical initiator. The product of this type of reaction appeared more evenly distributed with a more clear appearance than that from emulsion reactions. A brief attempt was made to electrospin this polymer product in HFIP (hexafluoroisopropanol). Fiber formation was unpredictable and NISO did not switch after electrospinning and this aspect of the project was not continued.

Ultimately PMA-NISO gels were not used for cell culture applications due to its hydrophobicity and the resulting propensity to turn slightly opaque in aqueous conditions. Polyacrylamide (PA) was chosen instead for its extensive application in cell culture experiments and the ability to incorporate DA-NISO into its polymerization process. Nevertheless, mechanical testing results obtained from PMA-NISO gels give an indication of NISO's ability to affect bulk gel stiffness and this ability was expected to translate to a PA hydrogel platform as well.

2.4.3 PA-NISO Hydrogel

Troubleshooting Hydrogel Synthesis
Polyacrylamide (PA) hydrogels have been a popular platform for creating a wide range of surface environments for cells growth. PA gels can be made in a wide range of stiffnesses and be surface modified with a variety of ECM molecules to accommodate many different cells types and their needs. As such, PA hydrogels were chosen as the platform of choice for testing cell growth and response on a NISO-crosslinked hydrogel.

Traditionally PA hydrogels have been made with several different photoinitiators, but all in aqueous solutions. The method used by previous research in this lab involved initiation with APS (ammonium persulfate) and TEMED (N,N,N′,N′-Tetramethylethylenediamine). Due to DA-NISO's low solubility in water, this method was not useable for this research. Initial attempts to alter the protocol using a mixture of water and DMSO as reaction solvent gave mixed results. Less than 10% of DMSO was not able to properly dissolve DA-NISO and the resulting gels had visible specks of precipitated NISO. When DMSO ratio was too high, however, it appeared to impede the reaction and gel formation was either very slow or did not occur at all. The free radical polymerization using this method is highly sensitive to the presence of oxygen. Protocol dictates that the reaction mixture is degassed before gel formation. The lack of gel formation, therefore, may be explained by the slower reaction leading to polymer chains ending early caused by exposure to oxygen.

Another previously published method involved the UV-activated initiator Irgacure 2959.[18,19] Irgacure 2959 is more friendly to organic solvents and is UV initialized, so there is much less concern over reaction initiation before the solution is evenly mixed, resulting in lumpy gels. Ultimately, after testing many formulas, the reaction was switched to a completely DMSO one. All components of the reaction are soluble in DMSO and it did not appear to hinder the polymerization. Naturally, extra wash steps were taken to ensure DMSO was completely removed from the hydrogel prior to cell culture.

However, the drawback appears to be that since NISO does absorb in the same range as the photoinitiator, the UV light used to polymerize gels could not penetrate too far into the solution. As a result, only thin gels were able to be made without defects. The thickest gels made were 150μm thick. Ultimately, 70μm was settled on as the thickness to be used to provide a deep hydrogel to attenuate the stiffness of the glass surface underneath, and simultaneously allowing for inverted confocal imaging as confocal microscopes have a very short working distance between objective and imaging plane.

The standard #1.5 coverslip measures approximately 160-190μm thick. Most high resolution objectives are designed for use with #1.5 coverslips for optimal image quality. However, experience showed that the variability in coverslip thickness and gel thickness combined together sometimes created the problem that the gel surface was unable to be imaged at all. All gels made for cell culture was then switched to glass bottom dishes using either #1 (130-160μm) or #0 (90-130μm) coverslips. Despite the less optimal glass thickness, imaging through a hydrogel already compromised image resolution and the change in glass should not have a noticeable effect.

Silanization
Although using DMSO as the reaction solvent solved the problem of polymerization in the presence of NISO, it created an entirely new problem in the silanization process. Previous protocol called for silanizing the glass surface with APTES (3-aminopropyltriethoxysilane) or APTMS (3-aminopropyltrimethoxysilane) to create a layer of primary amines on the glass surface for further conjugation. Glutaraldehyde was then conjugated to the primary amines, leaving a free aldehyde group to react with the secondary amines on acrylamide monomers, ensuring gel attachment to the glass surface.[20] However, this reaction requires an acidic environment so that protonation of the aldehyde may occur to fascilitate further reaction steps. A mixture of water and DMSO resulted in gels that peeled off the glass surface in spots. The completely DMSO polymerization mixture did not attach to the glass surface at all. An alternate surface modification scheme for the glass surface was required.

Silanization with TMSPMA removed the extra step of reacting with glutaraldehyde. TMSPMA activated the glass surface with methacrylate groups, which can directly polymerize into the backbone of polyacrylamide polymer chains. The standard protocol called for incubation at 110°C. This temperature, however, was too high for glass bottom cell culture dishes, which are made mostly of polystyrene and melted at high temperatures. After experimentation, an altered protocol with a longer incubation at 50°C produced similar silanization results without compromising the cell culture dishes.

Surface modification
Following in the footsteps of previous PA gel surface modification, initial attempts were made to conjugate ECM proteins, specifically fibronectin, onto the gel using sulfo-SANPAH (sulfosuccinimidyl 6-(4'-azido-2'-nitrophenylamino)hexanoate). Although well documented for use with PA hydrogel, the reaction mechanism of sulfo-SANPAH is not well controlled. There are more than 3 pathways it can possibly react with PA gels. Furthermore, previous research has shown that sulfo-SANPAH conjugated collagen peeled after cell culture.[21] A similar phenomenon was experienced in these experiments. Moreover, sulfo-SANPAH appeared to conjugate fewer ECM molecules to PA-NISO gels compared to PA control gels, suggesting there may be side reactions between the NISO molecule and sulfo-SANPAH that reduce the number of available NHS esters for reaction with ECM proteins.

ACA was chosen as an alternate surface modification route.[21] ACA is able to be incorporated into the PA polymer backbone via its end acrylic group, and the free carboxyl group on the other end can then be used for reaction with an amine.

With the switch to ACA, surface coating improved, but some problems in cell attachment persisted. It was finally determined that the sterilization process may have denatured fibronectin. A brief attempt was made to use RGD peptides instead of the full fibronectin protein for cell attachment. The 3 amino acid sequence RGD is the minmal required peptide derived from fibronectin for integrin binding. However, it was found that without sterilizing in 70% ethanol, fibronectin performed significantly better than 2 different RGD peptides tested. The surface modification protocol was then modified to accommodate this need. Fibronectin, EDC, and sulfo-NHS were sterile filtered after the hydrogel was first sterilized, and the entire conjugation reaction was performed under sterile conditions.

Micropatterning of PA-NISO hydrogels
Following previous protocols, an attempt was initially made to use PDMS molds for micropatterning PA hydrogels instead of chips of the silicon wafer itself. This method gave very poor results. It was likely that PDMS, being a porous material, allowed for easy diffusion of oxygen into the reaction mixture compared to a glass coversip or silicon wafer chip. The sensitivity of the free radical polymeriation reaction to oxygen resulted in poor or no gel formation under a PDMS stamp. Degassing PDMS stamps for 30 minutes prior to making gels sometimes improved results. However, due to the need for handling between removal from vacuum and gel formation, results were inconsistent and it was difficult to perfectly time this step. Attempts made to seal or coat PDMS stamps to prevent oxygen diffusion through were ultimately unsuccessful in improving gel formation. Using silicon wafer chips, although more time intensive in preparation, produced clear and sharp features in PA hydrogels (Figure 2.7).

NISO switching under the microscope
Prior to cell culture experiments, it was first necessary to determine the ability of NISO to switch under microscopy conditions. A 10-40-9:1 PA-NISO hydrogel was observed in brightfield during photostimulation over a period of almost 12 hours (Figure 2.6). NISO switching was observed via change in transmittance of light at 639nm. Due to its absorption peak in the green wavelengths, MC state NISO should appear darker at 639nm and therefore measure lower in

light transmittance. Although this measurement does not directly report on the change in stiffness, it is a reliable readout of NISO's ability to switch between states.

Over 12 hours, the PA-NISO gel switched more than 70 cycles and did not lose switching response throughout. Over time, there was a decrease in the change of the amount of light transmittance in each 405nm excitation cycle, which suggests fewer NISO molecules responding to excitation. This may be due to NISO molecule degrading over repeated cycles photostimulation. Nevertheless, after over 70 cycles of switching, NISO retained most of its switching ability.

This experiment also demonstrated the precise local control over NISO switching. Only a region of interest excited by 405nm displayed switching behavior while a control region of the same gel remained the same with unchanging transmittance throughout (Figure 2.6b-d). This control over local activation of NISO provides the opportunity for targeted stiffness change in probing cellular response to mechanical cues in a small area beneath, at the edge of, or away from the cell.

Cells attach and migrate on micropatterned PA-NISO hydrogels
Micropatterned PA-NISO hydrogel were capable of growing cells. Cells seeded on PA-NISO gels spread and were able to migrate (Figure 2.7). Figure 2.7a shows a 3T3 fibroblast spread on microposts on a 10-40-9:1 PA-NISO gel. Specifically, the cell appears to be attached to the gel only at the top of microposts. This cell seeding platform allows for even more precise control over NISO activation locally.

Cells growing on a microgroove patterned 10-30-2:1 PA-NISO gel elongated along the edge of the grooves and migrated on top of the grooves (Figure 2.7b-d). This platform provides an opportunity to study directed migration. While cells growing on an isotropic surface have many directions to choose from when migrating, cells on microgrooves are likely to migrate along the alignment of the grooves. This restriction to a 1D migration pattern simplifies analysis and makes it possible to determine exact cellular response to NISO switching at cell-edge.

AFM measurement of PA-NISO switch
AFM measurement of PA-NISO stiffness change was attempted in a manner similar to tensile testing for PMA-NISO gels. The AFM used was not equipped with a 405nm laser line and an external laser was used for gel excitation. This proved to be an unforeseen obstacle as the external laser often offset the calibration of the AFM internal laser used to detect tip deflection. Adjustments in testing protocol were able to account for this offset and quickly recalibrate before new measurements. However, this may have reduced the measured effect of NISO switching as the reverse switch from MC to SP state had begun while a few seconds were taken to recalibrate laser settings. As such, these measurements can only be considered preliminary and a more sophisticated measurement setup is required to record repeated switch cycles similar to that done for PMA-NISO.

Most PA-NISO switch testing done with AFM failed due to technical difficulties in obtaining any measurement at all. Only one set of data contained both analyzable SP and MC state data in continuous trials (Figure 2.8). Nevertheless, this set of data give some indication of PA-NISO

switching in a similar manner to PMA-NISO switching. Repeated testing on the same 10-40-9:1 PA-NISO hydrogel with alternate on off 405nm excitation show that the gel appears to decrease in stiffness when excited with 405nm light. This effect is seen particularly clearly in trials 6-13. Trial 11 in this stretch was missing due to calibration and measurement problems, resulting in two consecutive data points without 405nm activation.

Looking only at the on and off trials within this subset, it was clear that trials with 405nm activation have significantly lower stiffness (Figure 2.8b). This change, however, is only 5% of base stiffness. This level of percent change is small as compared to the 20% stiffness change seen in PMA-NISO gels. Nevertheless, previous research has shown that cells are capable of sensing stiffness change of less than 1kPa across their length *in vitro*, corresponding with physiological stiffness gradients, which can be as low as 1kPa/mm.[22] In light of this knowledge, the ability of PA-NISO to switch between 19kPa and 18kPa should, in theory, be enough to elicit a response from cells *in vitro*.

The trials at the beginning and the end of this set of data seem to indicate that there was a permanent decrease in stiffness with the initialization of testing and after repeated testing. IT is possible that photostimulation caused permanent damage to the bulk gel or a subset of NISO molecules within the gel. However, this may be due to the difficulties in taking measurements. Soft hydrogels often present adhesion problems for AFM tips and many trials resulted in error because of this. Moreover, AFM measurements in submerged conditions created more errors and failed trials. For future studies, perhaps an automated AFM system equipped with a native 405nm laser line is required to ensure seamless transition between switch cycles and error-free measurements.

Toxicity of 405nm excitation on 3T3's
One of the proposed applications of PA-NISO hydrogels is to conduct repeated and cyclical activation near or around cells seeded on these gels. As such, the toxicity of this testing method and the gel system itself must be assessed. AlamarBlue cell metabolism assays were conducted to measure cell health and/or death while growing on the PA-NISO gel system and in the presence of 405nm light activation.

The first test was used to establish an appropriate time point for measuring output of the alamarBlue assay. The second and third assays were measured at 18 hours after adding alamarBlue reagents as a result. Trial 2 included 10 minute continuous excitation by 405nm LED light bed across an output range of 0 to 20 mW/cm^2, as well as longer term excitation at 20 minutes and 1 hour, and a cyclic test at 10mW/cm^2 (Figure 2.9a). The 10mW/cm^2 continuous excitation for 1 hour condition killed off the majority of the cells on all 3 surfaces and was removed for trial 3.

In trial 2, for the glass surface, the 1 hour 10mW/cm^2 continuous excitation was statistically significantly less healthy compared to all other photoactivation conditions. No other conditions differed from one another. The PA-NISO gels had similar results. Suprisingly, the 20 mW/cm^2 condition for PA-bis control was statistically significantly less healthy than the 0 condition and the 20 mW/cm^2 condition but did not differ when compared to the other conditions. It is uncertain what happened to this set of samples. It is possible that NISO helps absorb the 405nm

light and attenuates the effect when compared to the PA-bis control, which would explain why this condition had more effect on PA-bis cells than PA-NISO cells. However, the glass-grown cells did not feel this effect at all.

As a separate observation, PA-NISO in general had lower health values. Since the health measurement is dependent upon a variety of factors, including cell density, it is possible that the source of this general difference was lower seeding on PA-NISO gels. This supposition is supported by the fact that the untreated PA-NISO condition is also lower health. While all conditions were seeded similarly, cells may attach less densely on PA-NISO gels. This set of gels were surface modified using the sulfo-SANPAH method rather than the later improved ACA method. This reflects previous observations that sulfo-SANPAH did not adequately coat the PA-NISO gel surface. On the other hand, it was possible that PA-NISO gels did not promote cell growth and in general inhibited healthy survival. To assess this possibility, the alamarBlue assay was repeated for trial 3 with samples of each surface type set aside for plating density assay. These samples were fixed and stained for DAPI 24 hours after seeding.

In trial 3, PA-NISO seeded cells appeared even less healthy as a group. However, the seeding density assay showed that, in this instance, there was less than half the cells on PA-NISO gels than compared to glass or PA-Bis gels. It appeared that PA-NISO modification using sulfo-SANPAH was highly variable and not reliable from batch to batch. With this caveat in mind, each surface (glass, PA-B, PA-N) was assessed with comparison to the untreated condition within the surface group. Similar to trial 2, no treatment conditions within the glass group or the PA-NISO group differed significantly from one another. The PA-bis results were also largely the same. Though, surprisingly, the cycle condition measured healthier than all other conditions, including the untreated one.

In general, these results suggest that photostimulation of NISO hydrogels is not harmful to 3T3's. While the 1 hour continuous excitation killed off most of the cells, we do not anticipate conducting any experiments where cells will be exposed to high levels of 405nm light for as long as an hour.

PA-NISO stiffness switch effect on cells
Current data is inconclusive on the effect of PA-NISO switching on 3T3's seeded on these gels, and further study must be conducted to characterize this function.

2.5 Conclusion

In this chapter, the molecule NISO was developed as a novel crosslinker for hydrogels in an attempt to establish it as a dynamic platform for studying cell mechanotransduction. While characterization has shown that NISO is capable of switching bulk gel stiffness reversibly and repeatedly in multiple types of polymers, more experiments remain to be conducted to precisely calibrate the range of this function. Specifically, it is highly desirable to be able to correlate the change in color observed in the MC state with the degree of stiffness change in the bulk gel, as calibrated per each gel formula. As such, a more versatile AFM platform is a must to simultaneously control 405nm laser output as well as measure hydrogel absorbance while taking

AFM measurements. This is absolutely possible on newer generations of automated AFM's and would be a topic of interest in future collaborations.

Once better characterized, the next step is to fully assess the ability of this platform to interact with cell in vitro and elicit a physical as well as biochemical response. Since the stiffness change seen in these hydrogels is on such a small level and occurs so quickly, it may be difficult to observe physical changes as cells are migratory even without NISO activation. A better approach may be to monitor intracellular signaling activities as immediate reactions to NISO-induced surface stiffness change. The following two chapters delve into developing tools that may very well serve this exact function.

2.6 References

1. Vogel, V. & Sheetz, M. Local force and geometry sensing regulate cell functions. *Nat. Rev. Mol. Cell Biol*. 7, 265–75 (2006).

2. Discher, D. E., Janmey, P. & Wang, Y.-L. Tissue cells feel and respond to the stiffness of their substrate. *Science* 310, 1139–43 (2005).

3. Schwarz, U. S. & Gardel, M. L. United we stand: integrating the actin cytoskeleton and cell-matrix adhesions in cellular mechanotransduction. *J. Cell Sci*. 125, 3051–60 (2012).

4. Lo, C. M., Wang, H. B., Dembo, M. & Wang, Y. L. Cell movement is guided by the rigidity of the substrate. *Biophys* J 79, 144–152 (2000).

5. Engler, A. J., Sweeney, H. L., Discher, D. E. & Schwarzbauer, J. E. Extracellular matrix elasticity directs stem cell differentiation. *J Musculoskelet Neuronal Interact* 7, 335 (2006).

6. Engler, A. J., Sen, S., Sweeney, H. L. & Discher, D. E. Matrix elasticity directs stem cell lineage specification. *Cell* 126, 677–689 (2006).

7. DeForest, C. A. & Anseth, K. S. Advances in bioactive hydrogels to probe and direct cell fate. *Annu. Rev. Chem. Biomol. Eng*. 3, 421–44 (2012).

8. DuFort, C., Paszek, M. & Weaver, V. Balancing forces: architectural control of mechanotransduction. *Nat. Rev. Mol. Cell Biol.* 12, 308–319 (2011).

9. Young, J. L. & Engler, A. J. Hydrogels with time-dependent material properties enhance cardiomyocyte differentiation in vitro. *Biomaterials* 32, 1002–9 (2011).

10. Hahn, M. S., Miller, J. S. & West, J. L. Three-Dimensional Biochemical and Biomechanical Patterning of Hydrogels for Guiding Cell Behavior. *Adv. Mater*. 18, 2679–2684 (2006).

11. Patterson, J. & Hubbell, J. a. Enhanced proteolytic degradation of molecularly engineered PEG hydrogels in response to MMP-1 and MMP-2. *Biomaterials* 31, 7836–45 (2010).

12. Kloxin, A. M., Kasko, A. M., Salinas, C. N. & Anseth, K. S. Photodegradable hydrogels for dynamic tuning of physical and chemical properties. *Science* (80). 324, 59–63 (2009).

13. Tang, Z., Akiyama, Y., Yamato, M. & Okano, T. Comb-type grafted poly(N-isopropylacrylamide) gel modified surfaces for rapid detachment of cell sheet. *Biomaterials* 31, 7435–43 (2010).

14. Ikonen, L., Kerkelä, E. & Metselaar, G. 2D and 3D self-assembling nanofiber hydrogels for cardiomyocyte culture. *BioMed Res. Int*. 2013, (2012).

15. Petchprayoon, C., Yan, Y., Mao, S. & Marriott, G. Rational design, synthesis, and characterization of highly fluorescent optical switches for high-contrast optical lock-in

detection (OLID) imaging microscopy in living cells. *Bioorg Med Chem* 19, 1030–1040 (2011).

16. Sakata, T., Yan, Y. & Marriott, G. Optical switching of dipolar interactions on proteins. *Proc Natl Acad Sci U S A* 102, 4759–4764 (2005).

17. Marriott, G. et al. Optical lock-in detection imaging microscopy for contrast-enhanced imaging in living cells. *Proc Natl Acad Sci U S A* 105, 17789–17794 (2008).

18. Williams, C. G., Malik, A. N., Kim, T. K., Manson, P. N. & Elisseeff, J. H. Variable cytocompatibility of six cell lines with photoinitiators used for polymerizing hydrogels and cell encapsulation. *Biomaterials* 26, 1211–8 (2005).

19. Tse, J. R. & Engler, A. J. Preparation of hydrogel substrates with tunable mechanical properties. *Curr. Protoc. Cell Biol.* Chapter 10, Unit 10.16 (2010).

20. Kraning-Rush, C. M., Carey, S. P., Califano, J. P. & Reinhart-King, C. A. Quantifying traction stresses in adherent cells. *Methods Cell Biol* 110, 139–178 (2012).

21. Yip, A. K. et al. Cellular response to substrate rigidity is governed by either stress or strain. *Biophys. J.* 104, 19–29 (2013).

22. Tse, J. R. & Engler, A. J. Stiffness gradients mimicking in vivo tissue variation regulate mesenchymal stem cell fate. *PLoS One* 6, e15978 (2011).

2.7 Figures

Figure 2.1   NISO switches conformation with the excitation of light (a). The conformation switch also causes a visible color change in the hydrogel (d) due to the change in absorption spectrum between the two states of NISO (e). For this thesis, NISO was synthesized with two different end functional groups for crosslinking (b,c).
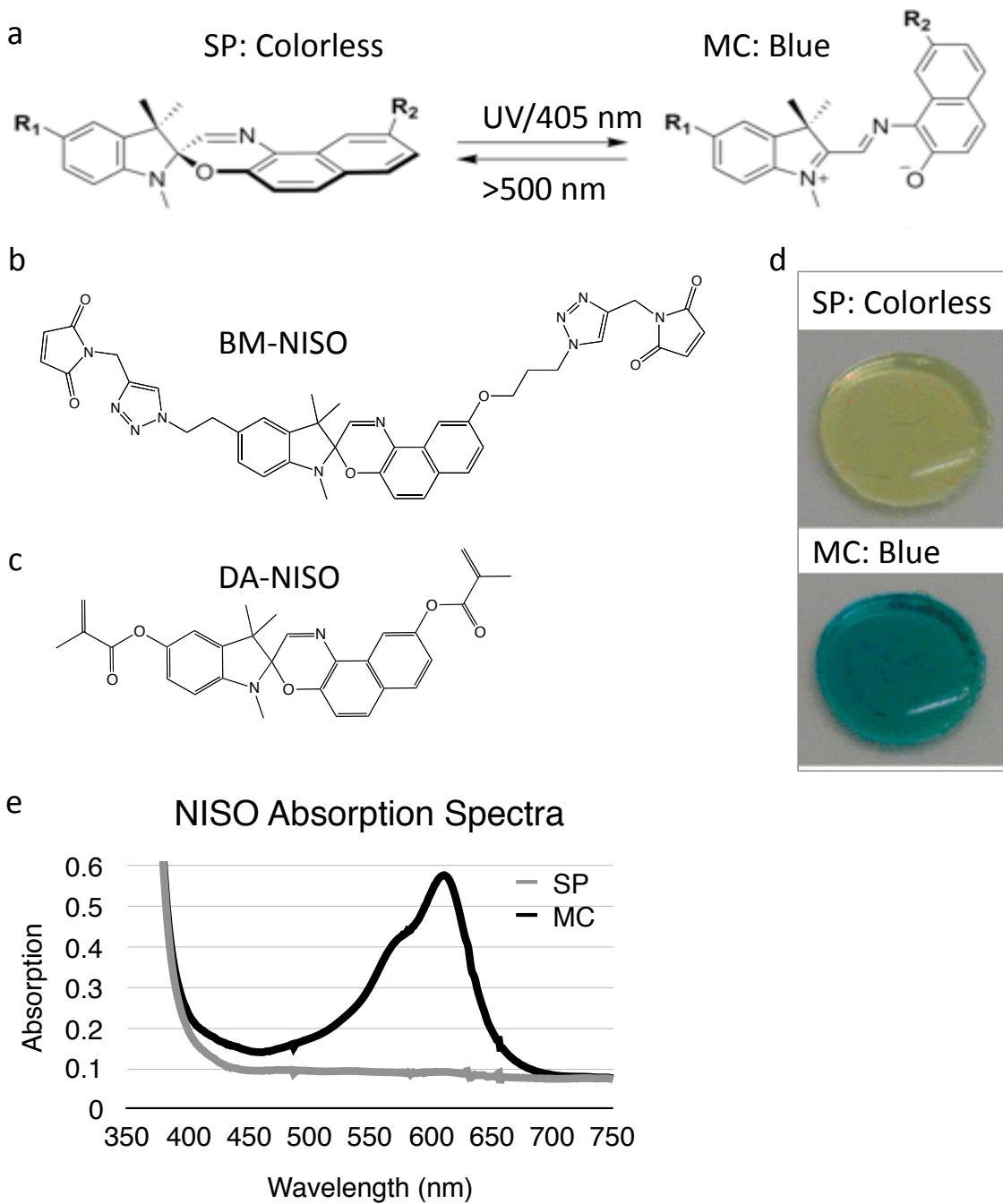
Figure 2.2   Tensile testing with 305nm LED excitation for PMS control gels and PMA-NISO gels. PMA control gel did not change stiffness with 395nm LED excitation (a), while PMA-NISO, both 1x and 2x NISO samples, reliability lower in stiffness upon excitation (b,c). Furthermore, the amount of stiffness reduction appears to increase with increased LED power (c,d). The stretch setup is shown in e.
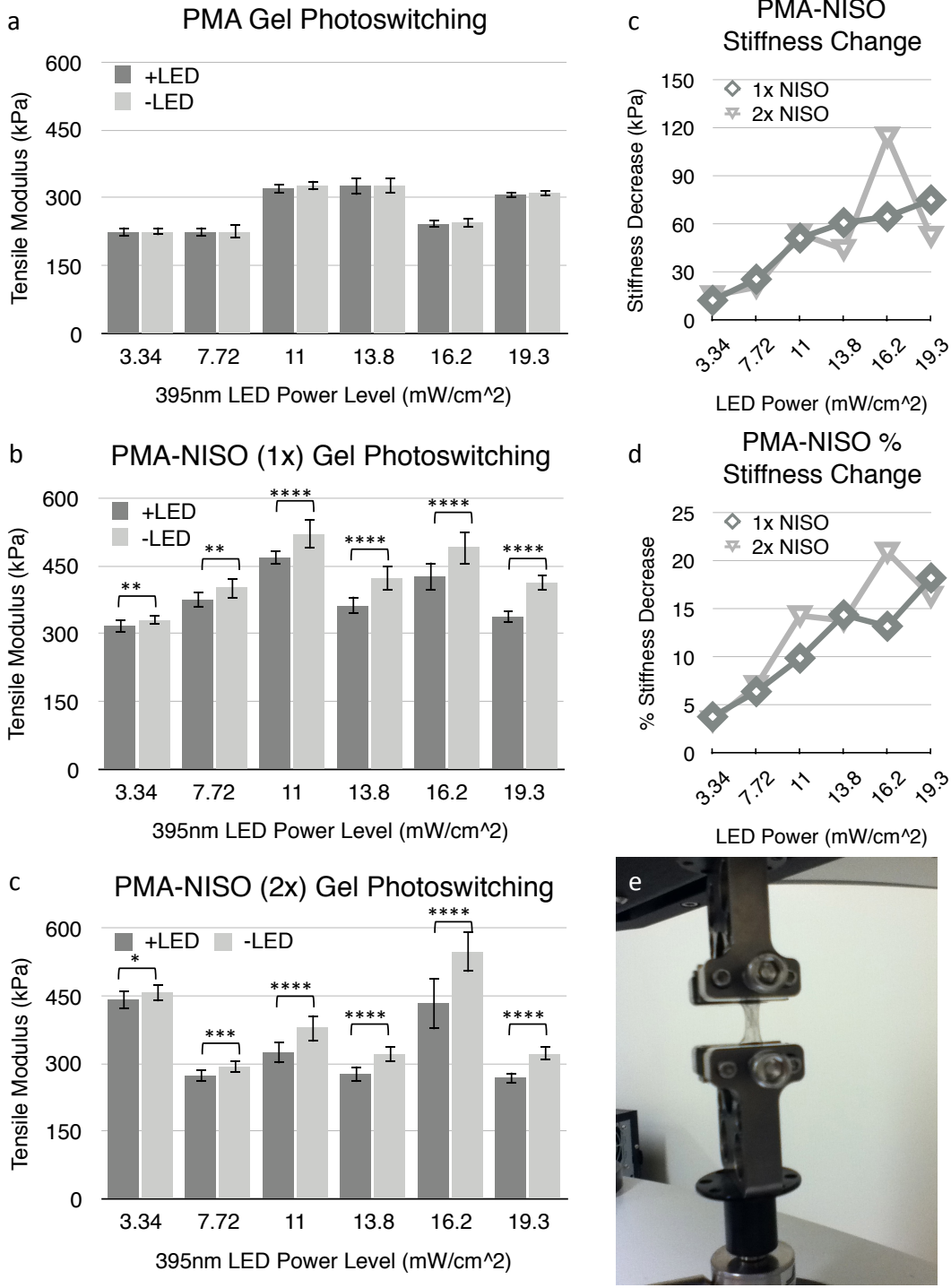
Figure 2.3 Tensile testing of PMA-only control gels shows no change in stiffness between data taken with or without 395nm LED excitation. Furthermore, changing LED power level has no effect on the results. This indicates that the LED excitation is not changing the stiffness of the PMA polymer itself through any effects of heat or light damage. Any significant change seen in PMA-NISO gels can be attributed to NISO's photoresponsive properties.
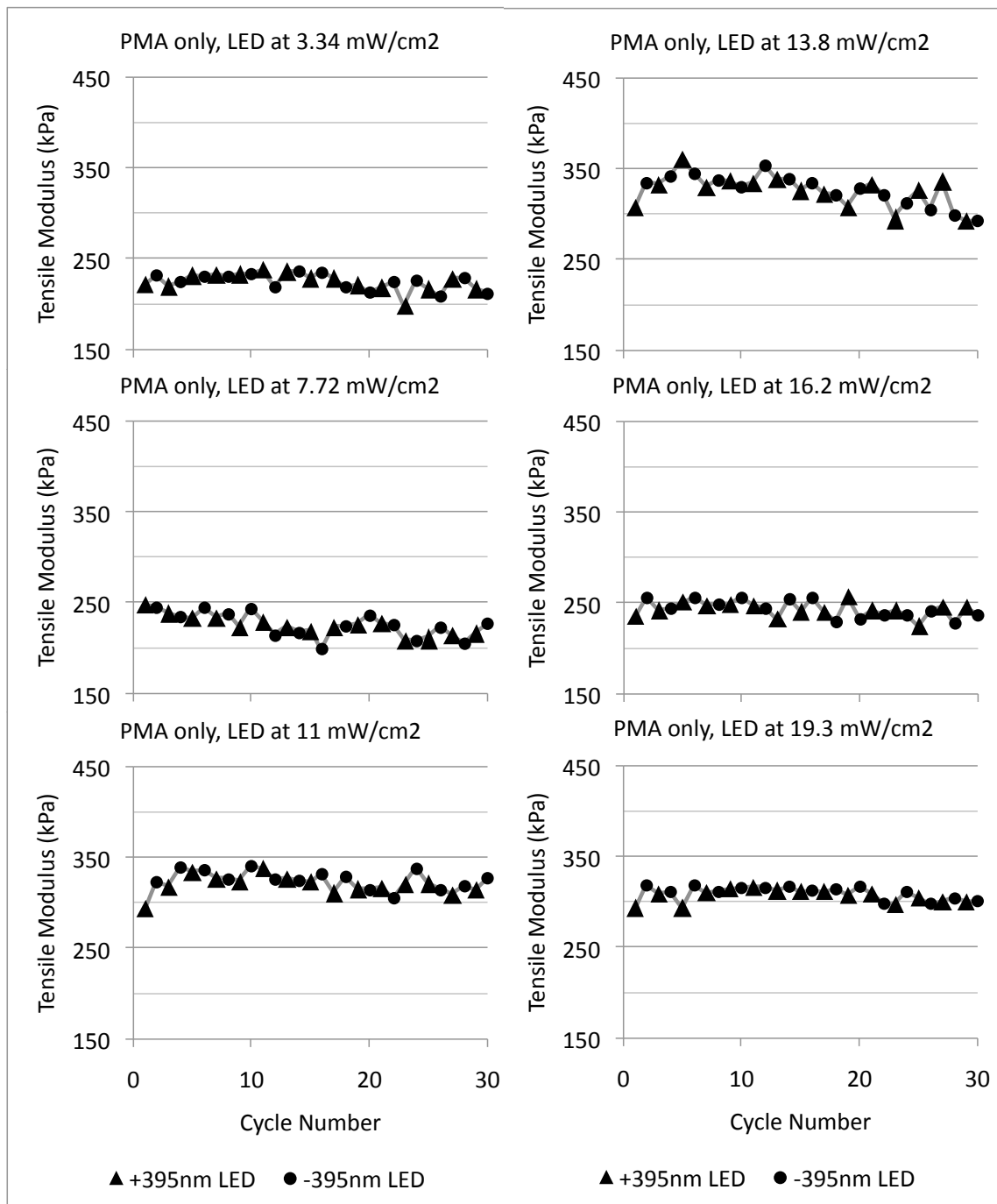
Figure 2.4 PMA-NISO (1x) reliably switches between softer in MC state and stiffer in SP state at higher power levels of 395nm LED excitation. Furthermore, there is a trend of decreased stiffness change as power level is decreased. However, at the lowest 2 levels, switching of stiffness appears less reliable, perhaps due to the margin of error in measurement being bigger than the switch itself.
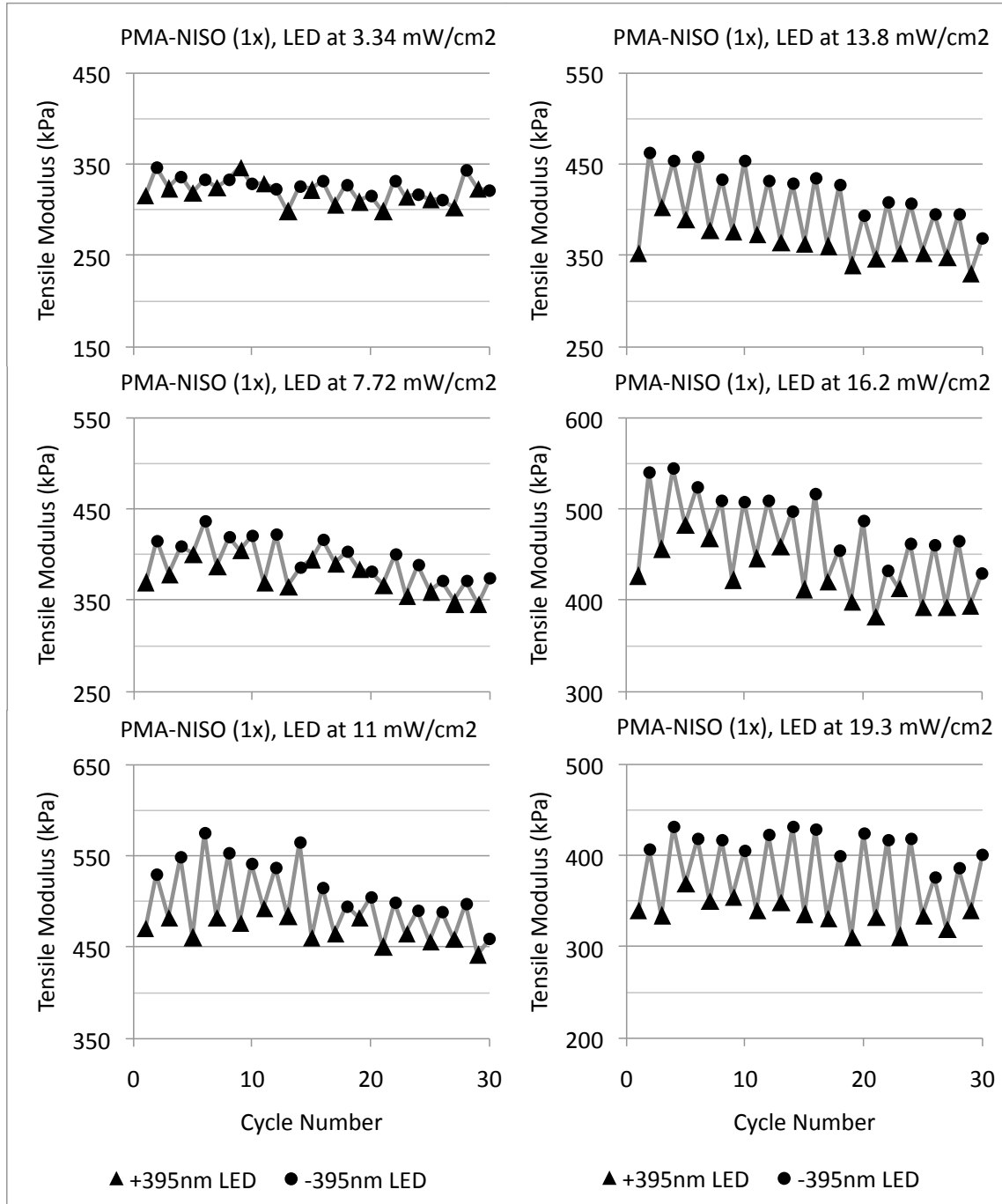
Figure 2.5 PMA-NISO (2x) displays similar stiffness switching capabilities as PMA-NISO (1x). However, the doubling of NISO concentration in the polymer does not show a significant increase in the amount of stiffness change overall. The data at 16.2 mW/cm^2 appears to show a larger change in the 2x NISO, but this effect is not replicated in the other samples.
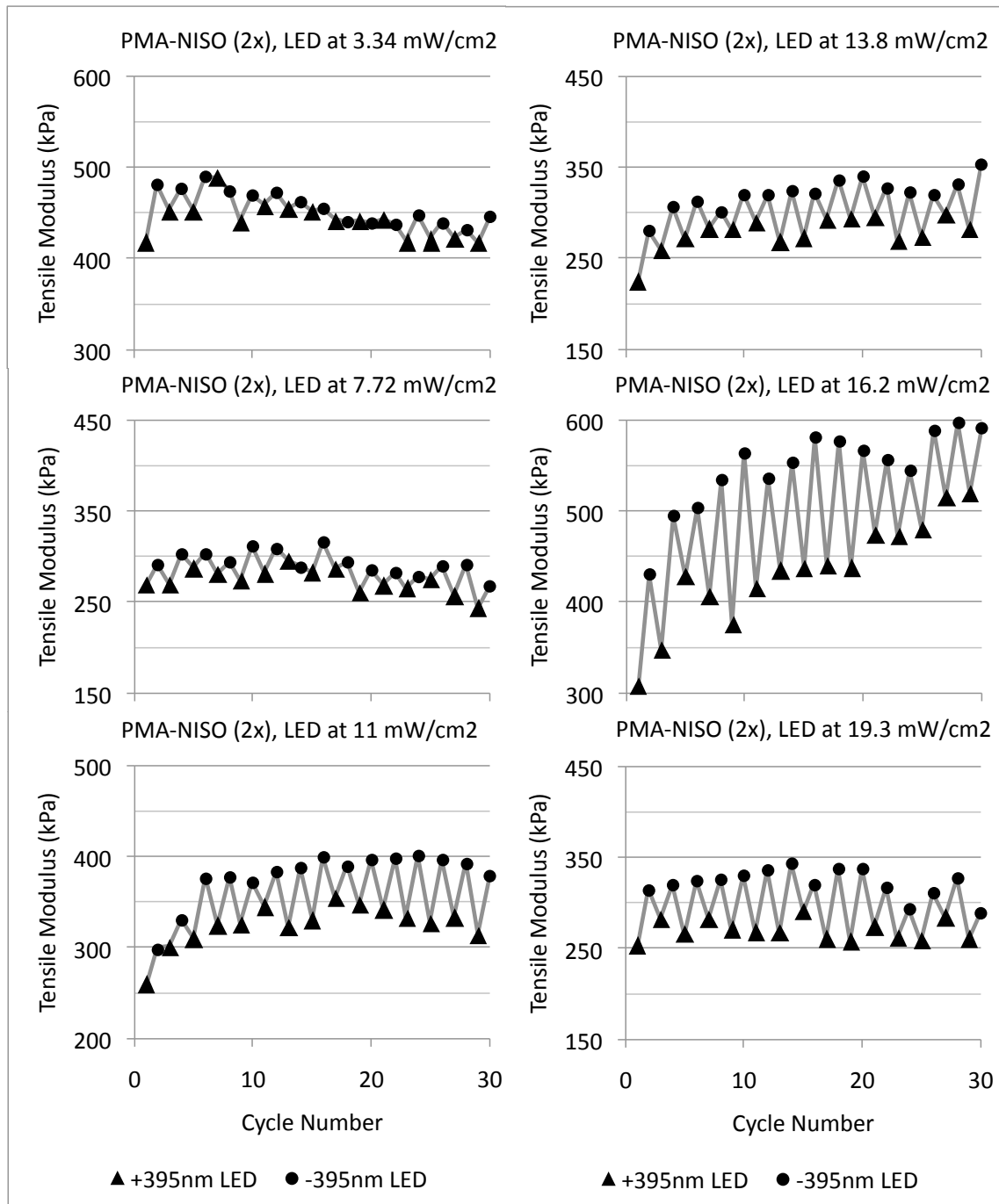
Figure 2.6 PA-NISO repeated switching between SP and MC states over 12 hours with a switch cycle every 10 minutes (a). Comparing the first 2 and last 2 cycles show that even after 70+ cycles of switching, NISO is still reliability switching. However, there does appear to be a reduction in the amount of switch as seen in the reduced change in light transmission through the hydrogel. This may be due to some amount of NISO molecules being stuck in MC state after repeated excitation. Comparing the excited region to a control region without 405nm excitation, it is clear that NISO switch can be very locally controlled (c,d). Only the excited region shows switching behavior (black arrow in d) while elsewhere the hydrogel remains unchanged.

PA-NISO Switch Over 12 Hours

Light Transmittance vs Time (hours)

First and Last 2 Switch Cycles

Light Transmittance vs Time (minutes)

- — First 2 cycle (no 405nm) ——First 2 cycles
----- Last 2 cycles (no 405nm) ——Last 2 cycles

c -405nm

d +405nm

50 μm

29
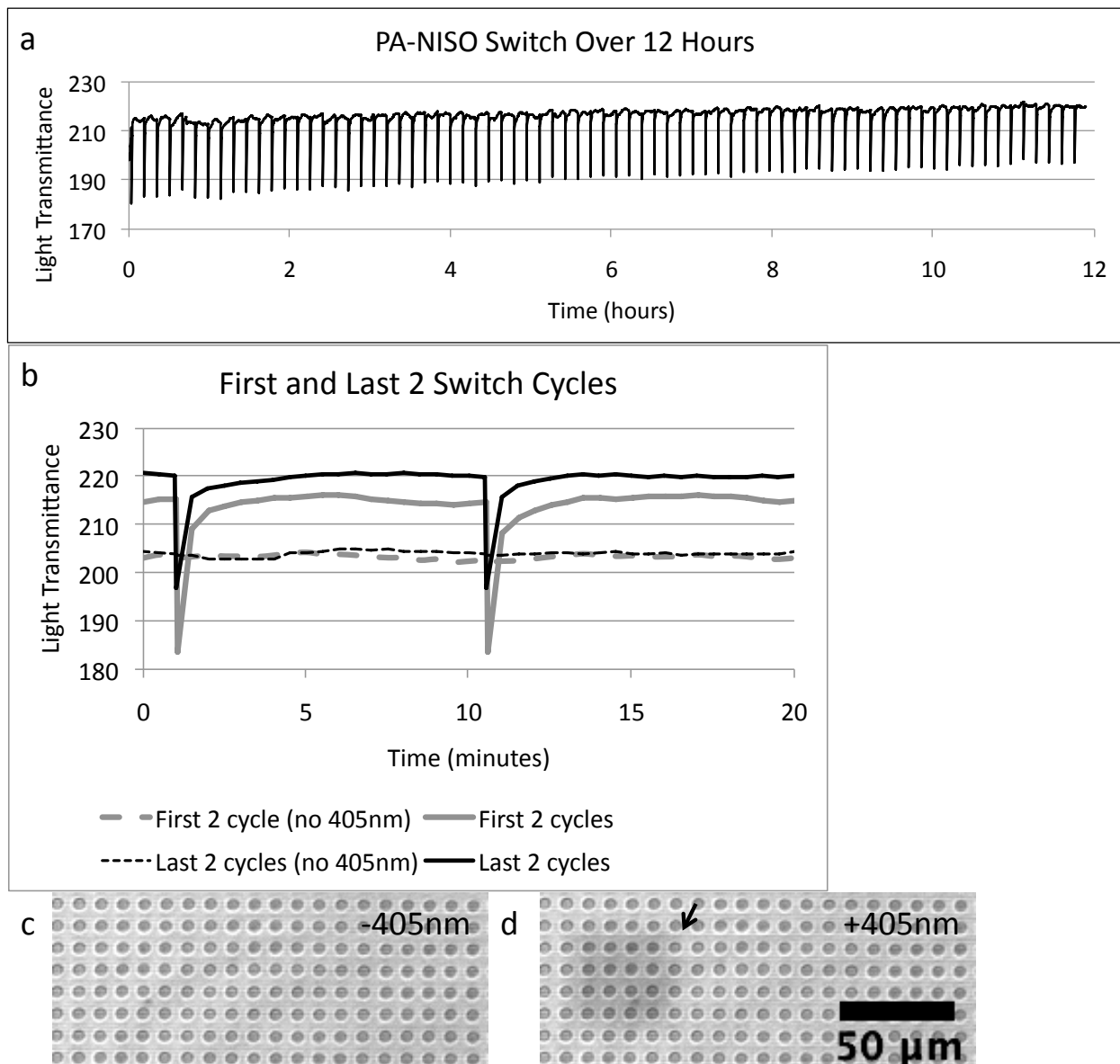
Figure 2.7 3T3's attach and spread on micro-patterned PA-NISO. 3T3 cell spreads in all directions on a field of microposts on PA-NISO (a). Whereas, on microgrooves, cells grow in a spindle shape with the shape of the grooves and migrate along the grooves over time (b-d). The three clearly migratory cells are shown with white arrows.
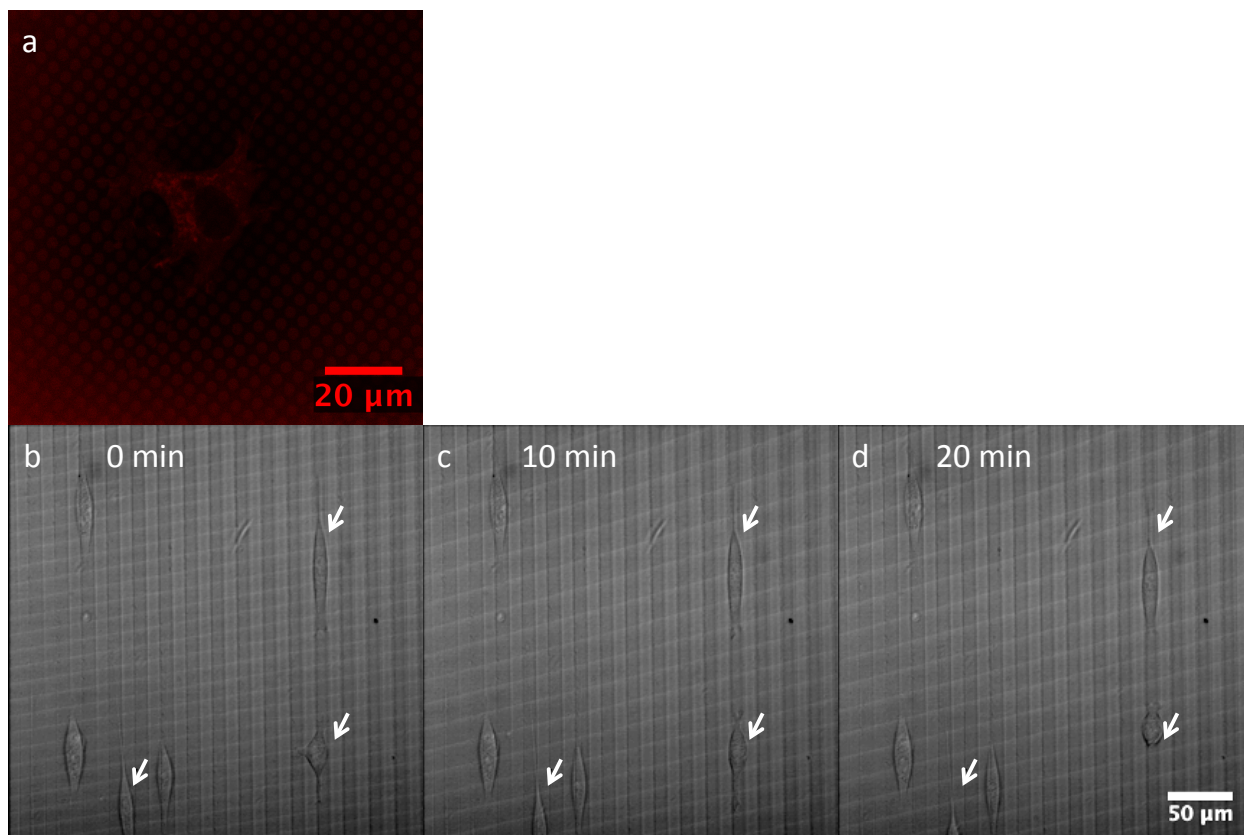
Figure 2.8 PA-NISO hydrogel stiffness measured by AFM with and without 405nm laser excitation (a). The same hydrogel is repeatedly measured over times. Several trials are missing due to uninterpretable AFM data. There appears to be come permanent change to the gel seen at the beginning and end of trials. However, the middle 7 trials showed some level of switching. These 7 trials are further compared by separating into trials with and without 405nm excitation (b).
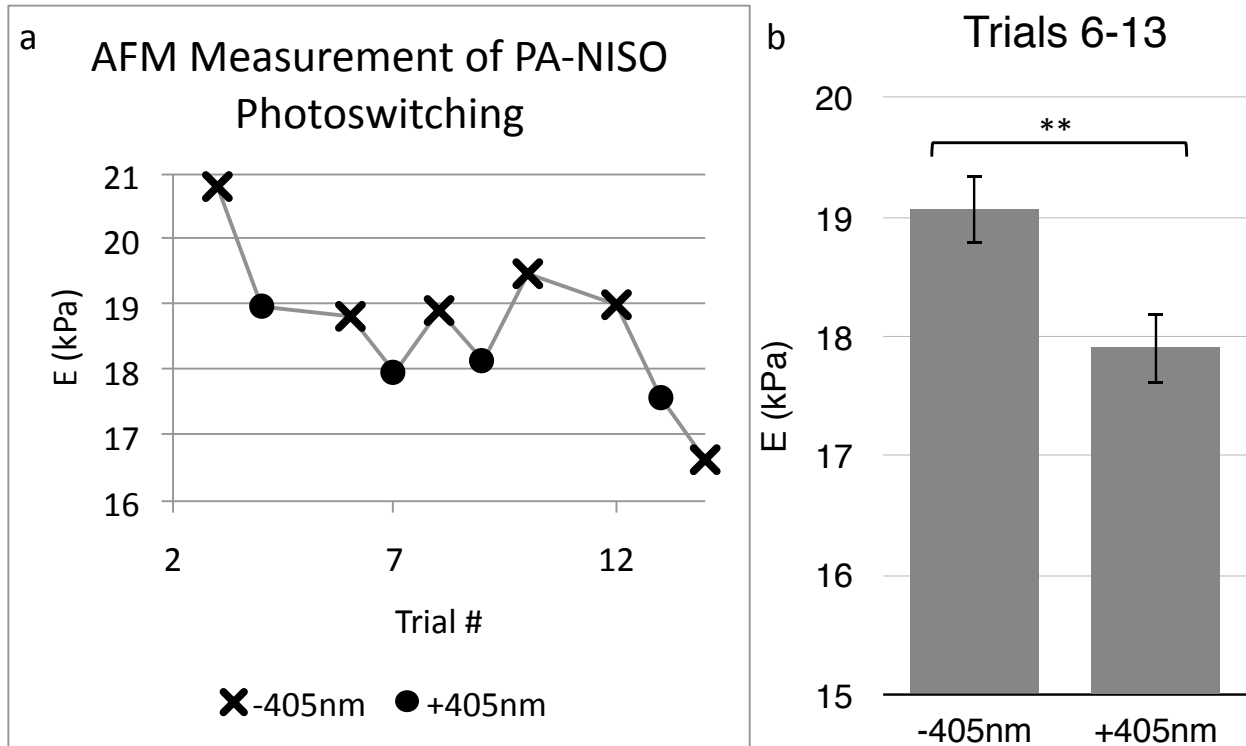
Figure 2.9 AlamarBlue 3T3 cell health assay for PA-NISO photoactivation was conducted with both glass and PA-Bis controlled across a series of different photoactivation conditions. Both assays show photoactivation on a limited scale do not damage cell health.
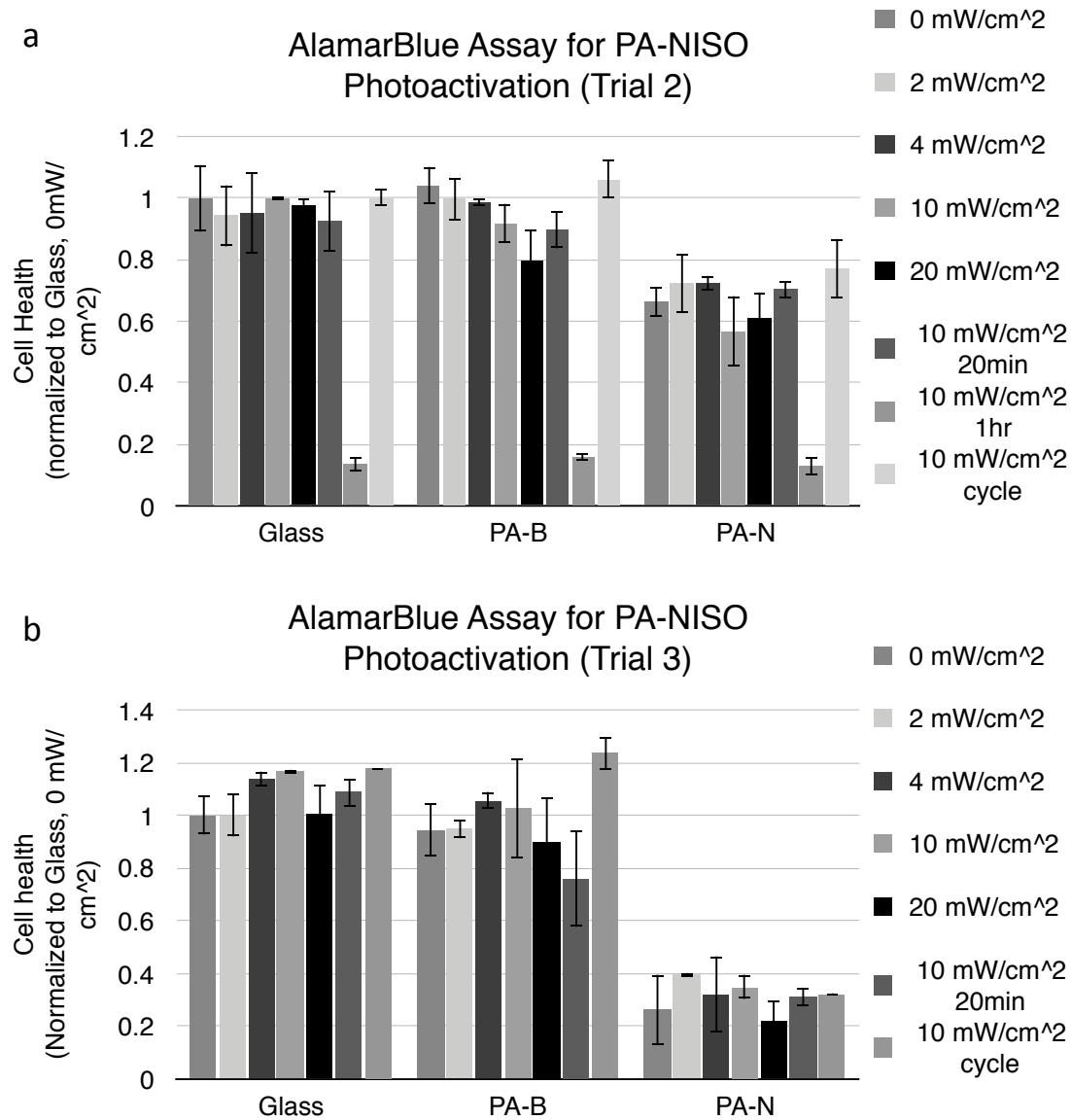
CHAPTER 3

fLOV2 as a Fluorescent Marker for Intracellular Studies

3.1 Emergence of Fluorescent Proteins as Analytical Tools in Cell Biology

A written record of fluorescence existed as early as the sixteenth century, observed by the botanist Nicolas Monardes as a blue color in the infusion of wood from a Mexican tree. Many followed and expanded upon the knowledge of this phenomenon, including but not limited to Robert Boyle, Isaac Newton, Sir David Brewster, and Sir John Herschel.[1] Sir John Herschel famously made the observation of fluorescence in a quinine solution, which remains a popular method of classroom demonstration in the present day. It was not until 1852, however, that George Stokes introduced the term "fluorescence" in a formal treatise summarizing his research, and it has remained in the scientific lexicon ever since.[2] However, Stokes himself continued to refer to it as "dispersive reflection" in this first paper. Stokes identified the property that the dispersed light in this phenomenon is always of a longer wavelength compared to the incident light hitting the sample. Thus this was termed the Stokes shift after him.

Further application of quantum theory led to the understanding that Stokes shift arises in the natural decay process of an excited electron.[3] Figure 3.1 is a simple Jablonski diagram showing the ground, first, and second energy states of an electron. With the absorption of a photon of the appropriate energy, an electron in the fluorophore is excited to the S_1 state, or very rarely to the S_2 state. Due to the existence of multiple vibrational levels in each state, excitation can occur across a wide spectrum of wavelengths. However, the electron quickly relaxes to the lowest vibrational level within a picosecond and emission only occurs from the lowest vibrational level of the excited state. This internal conversion of energy prior to emission is what causes the energy difference between the incident light and the emitted light, explaining the existence of the Stokes shift. Return to ground state via the emitting of a photon may also occur to multiple vibrational levels of the ground state. Excitation and return to multiple vibrational levels creates an interesting mirror effect in the absorption and emission spectra of a typical fluorescent molecule due to the similarity in energy differences between vibrational levels regardless of being in ground or an excited state. This is in seen in multiple fluorescence proteins explored in this chapter. Historically, fluorescence had been studied in small molecules, however, since the discovery of proteins with fluorescent properties, they have taken over in many aspects of biological research. This brief introduction concerns only fluorescent proteins and therefore does not touch upon bioluminescent proteins such as luciferin.

Fluorescent proteins have a number of advantages over their small molecule predecessors in cell signal imaging applications. Small molecule fluorophores, while wide-ranging in their photophysical properties, are limited by their cell membrane permeability and by the types of intracellular processes they can interact with and therefore track within the context of living cells. Furthermore, these fluorescent small molecules are often the product of a complex series of synthesis steps. Fluorescent proteins, however, can be genetically encoded and expressed within the cell itself, thus becoming directly incorporated into the cell's own machinery. The reaction which generates the fluorophore within the fluorescent protein is autocatalyzed under biological

conditions and requires no external intervention.[4] This allows fluorescent tags to be fused onto any number of target proteins, greatly expanding the number of cellular processes and protein interactions that can be dynamically monitored using fluorescence-based microscopy techniques.

The first discovery of a fluorescent protein was published in 1962 of green fluorescent protein (GFP) isolated from the *Aequorea victoria* jellyfish by Osamu Shimomura but remained under the radar for several decades.[5] However, with advancements in molecular cloning, fusion proteins sensors became a possibility. Fluorescent protein based sensors exploded into widespread use in biological sciences in the 1990's following the GFP gene's first successful sequencing and cloning in 1992 by Douglas Prasher, and subsequent expression in *E. coli* and *C. elegans* in 1994 by Martin Chalfie.[6,7] The success of these experiments opened the door for many others to improve upon the wild type GFP. Roger Tsien led the first wave of fluorescent protein innovations by creating a GFP mutant with a single excitation peak and increased fluorescent output.[8] Since then, numerous variants of GFP and its homologs have been synthetically engineered, covering a range of absorption and emission spectra, as well as improved photophysical properties.[9,10] In 2008, Shimomura, Chalfie, and Tsien jointly received the Nobel Prize in Chemistry for their discovery and development of GFP and its family of fluorescent proteins.

The availability of such a wide range of fluorescent proteins increased access to the study of more complex cellular processes taking advantages of fluorescence properties such as fluorescence anisotropy and Förster resonance energy transfer (FRET).

Other fluorescent proteins such as iLOV have been introduced into the repertoire of intracellular tools but have not been met with widespread adoption and use compared to the GFP family of proteins.[11,12]

3.2 FRET

Förster resonance energy transfer (FRET) was first described by Theodore Förster in 1946 as characterized by a nonradiative energy transfer from an excited donor fluorophore to a nearby acceptor fluorophore with absorption matching that of the energy being transferred via a weak dipole-dipole interaction.[13] This energy transfer from the donor to the acceptor effectively quenches the donor's fluorescence emission while causing emission from the acceptor protein, typically termed sensitized emission. Although FRET was first extensively studied between small molecules, this section will mainly discuss FRET between fluorescent proteins for the purposes of biological sensors.

As indicated in the name, FRET is an energy transfer from a donor protein to an acceptor protein. As such, the emission spectrum of the donor must overlap to some degree with the absorption spectrum of the acceptor for the energy transfer to be successful. A larger spectral overlap is indicative of a higher efficiency in energy transfer. A second criterion dictates that the emission dipole of the donor molecule and the absorption dipole of the acceptor molecule must not be perpendicular to each other. The energy transfer occurs via a dipole-dipole interaction, and if the two dipoles are perpendicular to each other, their oscillations cancel each other out and there is no energy transfer. The third criterion for FRET is a rule of distance. Förster theorized

that the efficiency of energy transfer decays in a sigmoidal fashion in relation to distance between donor and acceptor and this was proven in.[13] A general rule of thumb is a maximum of 10nm of separation between the two molecules. However, in reality the operating distance is much shorter and varies based on exact FRET pair.

FRET efficiency
It has been shown quantitatively that FRET efficiency, as defined by the percentage of energy transfer, has an inverse sixth power relationship with the distance between the two fluorophores as described by the following equations.[14,15] The first equation describes the relationship between FRET efficiency and the distance R between fluorophores, with R_0 being the Förster Radius, the distance at which efficiency is 50%.

$$E = \frac{R_0^6}{R_0^6 + R^6}$$

Eqn 1.

The theoretical value of R_0 in Å can be calculated with the following equation, where κ^2 is the orientation factor of the fluorophore dipoles, ϕ_D is the donor quantum yield, n is the refractive index of the medium, and J is the overlap integral between donor emission and acceptor absorption.

$$R_0 = \left[\frac{9000\ln(10)\kappa^2 \phi_D}{4(2\pi)^5 N n^4} J \right]^{\frac{1}{6}} = 0.2018\left(\kappa^2 \phi_D n^{-4} J\right)^{\frac{1}{6}}$$

Eqn 2.

The overlap integral J is calculated by the following equation with λ being wavelength in nm, $F_D(\lambda)$ is the emission spectrum of the donor normalized to integrate over wavelength to the value of 1, and $\varepsilon_A(\lambda)$ is the absorption profile of the acceptor scaled to its molar extinction coefficient with units of $M^{-1}cm^{-1}$

$$J = \int F_D(\lambda)\varepsilon_A(\lambda)\lambda^4 d\lambda$$

Eqn 3.

Practical considerations for FRET pairs
Aside from the absolute necessities of FRET, several factors also influence whether a FRET pair is practically useful in research. The Förster radius R_0 is a very important value in evaluating a FRET pair. Figure 3.1 shows a theoretical efficiency profile of a FRET pair with an R_0 of 5nm, which is comparable to many presently available protein FRET pairs. On this graph, 2 example regions are selected to highlight the importance of the inter-fluorophore distance of a FRET pair in a sensor. FRET sensors use proximity of the two proteins as a measure for specific activities within the cell, therefore they must be sensitive to change in distance. However, this sensitivity is greatly affected by how the inter-fluorophore distance of the FRET pair compares to Förster radius. Due to the sigmoidal shape of the efficiency curve, there is an optimal range of inter-fluorophore distance around R_0 in which a change in distance between donor and acceptor will provide the maximal measureable FRET change, creating a more sensitive FRET sensor. Away from R_0, the same change in distance will give a much smaller FRET efficiency change and be more susceptible to influence by noise in the data (Figure 3.1).

Many FRET sensors are intramolecular in design, meaning the two fluorescent proteins are part of the same recombinant protein with sensor regions of peptides between and around them that change conformation to bring the donor and accepter closer together or farther apart when the sensor peptides are bound or activated in some way. The existence of the sensor regions creates

steric hindrance and conformational limitations around the fluorescent proteins and increases the minimal distance between them. If this pushes the inter-fluorophore distance of the FRET pair too far past R_0, measurement of change will be more difficult and noisy. A FRET pair with a larger R_0 allows more space for sensor regions while maintaining optimal inter-fluorophore distance.

To increase the Förster radius, one can simply look at Eqn 2 and 3. The two variables one has control over when choosing FRET pairings are ϕ_D and ε_A. While κ^2 also has an effect, it's more difficult to predict. Maximizing both ϕ_D and ε_A will ensure a comparatively large R_0.

While the donor emission and acceptor absorption spectra overlap determines whether FRET will occur, the Stokes shift of both fluorescent molecules help determine the level of noise in the FRET measurement. Due to the nature of fluorescence as previously described, energy is lost between excitation and emission, causing the emitted light to be of longer wavelength than the exciting light. This difference, measured as the difference between the excitation spectrum maximum and the emission spectrum maximum, is termed the Stokes Shift. FRET is often measured via ratio of acceptor sensitized emission to donor emission. A large Stokes shift in both donor and acceptor help improve spectral separation in FRET measurements. Overlap exists between the absorption and emission spectra of any fluorophore. Combined with the donor emission and acceptor absorption overlap necessary for FRET to occur, this leads to bleed-through in both directions in measurements of donor or acceptor emission channels. While acceptor bleed-through into donor channel is often easily resolved by using the appropriate filter, the long emission tail existent in most fluorophores makes the opposite much more difficult. The donor emission must be estimated and subtracted from the fluorescence measurement in the acceptor channel to gather more accurate data. A large stokes shift in the acceptor will aid in reducing the donor bleed-through into the acceptor channel and generate more easily interpreted FRET data.

Scientific publications utilizing FRET have significantly increased in number since the dawning of the new century. While the photophysical phenomenon of FRET had been known since the early 20th century, it was not until recently that a wide array of fluorescent proteins were designed and made available for biological applications.[16] In order for FRET to occur between two fluorescent proteins, there must be extensive compatibility on several fronts, and the expanded library of available proteins made it possible to select and match appropriate pairs. In further discussions of this chapter,

3.3 fLOV2

Although the GFP-family of fluorescent proteins has seen popular use in elucidating various cellular mechanisms, there are several unavoidable limitations due to the structural nature of these proteins. With a molecular weight of 27kDa, GFP is bulky enough to interfere with certain intracellular functions. For example, in the fluorescent tagging of actin monomers, the expression level of GFP-actin must be carefully controlled. G-actin itself is only a bit bigger than GFP in mass and shape, and it must polymerize tightly in the formation of F-actin filaments. Over expression of GFP-actin dramatically impairs actin function.[17] When it comes to FRET, the β-barrel of GFP-type proteins surround the central fluorophore and ensure a minimal distance of

roughly 3nm between the donor and acceptor if both proteins are GFP homologs.[18] However, this minimal distance does not take into account the various linkers and sensing elements that modulate the interactions between donor and acceptor in a FRET sensor. More often, the inter-fluorophore distance between the two fluorophores in a FRET pair is much longer. As previously described, the use of FRET as a protein activity sensor is highly sensitive to donor and acceptor separation distance.

fLOV2 is a small (~12kDa) mutated fluorescent derivative of the LOV2 domain of the common oat plant (*Avena sativa*). LOV, or Light/Oxygen/Voltage sensitive, domains exist in many species of plants, fungi, and bacteria. In their native function, they serve to aid in the organism's reaction to light.[19] LOV domains primarily bind the cofactor flavin mononucleotide (FMN), which is in itself a blue light absorbing chromophore, to become a green-fluorescing complex. When combined with modulating domains such as the Jα helix, the LOV domain functions as a photoreactive switch that affects many downstream pathways. In Avena sativa, LOV domain functions control downstream processes such as stomata opening for gas exchange and chroloplast movement for optimal photosynthesis.[20]

In the laboratory setting, the LOV domain has been used as a photoswitch to control cellular movement *in vitro* using blue light.[21] By joining Rac1 to LOV2-Jα, Wu et al. were able to successfully mask the activity of a constitutively active Rac1. In the dark state, the LOV2-Jα-Rac1 conformation blocks the binding site of Rac1. Using blue light to excite the complex, the Jα helix is released from LOV2 and Rac1 becomes active, resulting in the ability to "walk" a cell in any direction by locally activating Rac1.[21] Further research by the same group generated a LOVTRAP that locally sequestered any protein of interest to be released upon excitation with blue light.[22] These results, although interesting, do not make use of the LOV domain's intrinsic capabilities as a fluorescent protein.

In the aim of fully utilizing the fluorescent properties of the LOV domain, much research has been conducted to stabilize and optimize LOV2 fluorescence. In its original state, LOV2 temporarily photobleaches in the blue wavelgnths, rendering it unstable as a fluorescent protein.[23] By mutating cysteine 39, which forms the bleached intermediate, to an alanine, Salomon et al. stabilized the absorption properties of LOV2 and increased its fluorescence, paving the way to its use as a fluorescent tag.[24] Further mutagenesis and enhancements created the iLOV variant from the LOV2 domain of the plant *Arabidopsis thaliana*, which exhibited increased quantum yield and further reduced photobleaching.[11,25] iLOV and its derivatives are currently the most prominent LOV-derived fluorescent proteins available for research use. fLOV2, developed from *Avena sativa*, aims to be a competitor to iLOV with its red-shifted emission, with peak at 513nm compared to iLOV's 495nm, and otherwise similar photophysical properties.

fLOV2 holds a further advantage over GFP since LOV domains are able to correctly mature and function in an anaerobic condition as its cofactor FMN is readily available in all organisms, aerobic or not, while GFP requires an oxygen-rich environment to react and generate its central fluorophore.[26] This advantage is not explored in this text. Nonetheless, it may of interest to others seeking to expand the use of fLOV2 as a genetically encoded fluorescent reporter in anaerobic organisms.

3.4 Materials and Methods

3.4.1 FRET Pair DNA Constructs

DNA constructs of fLOV2/mRuby2 FRET pair were designed in SnapGene viewer software and synthesized using molecular cloning techniques as described below. Plasmids containing constructs referred to in this chapter and primers used in generating these constructs are listed in Table 3.1 and Table 3.2, respectively.

From here on, for sake of clarity, when referring to the FRET pair as donor/acceptor, it will appear as fLOV2/mRuby2. However, due to the ordering of proteins in the constructs used in this research, the proteins themselves will be described as mRuby2-fLOV2.

mRuby2-pBAD (PL0100) was a gift from Michael Davidson (Addgene plasmid # 54771).[27] fLOV2 (PL0200) was a gift from Alexander Hoepker based on his previous work mutating the LOV2 domain for improved fluorescence.

The minimal mRuby2-fLOV2 fusion construct (PL0201), "minimal" referring to the short 6 amino acid spacer between the two fluorescent proteins, was synthesized from PL0100 and PL0200. An NheI restriction site in PL0100 was first removed using site-directed mutagenesis with primers PR05 and PR06. The mRuby2 gene with leading 6xHis tag, T7 tag, and TEV site was amplified using primers PR01 and PR02 and cloned into PL0200 using NcoI and NheI, resulting in PL0201 with bacterial expression. The corresponding mammalian expression construct PL0301 was generated by cloning PL0201, with primers PR07 and PR08, into the pcDNA3.1 vector using KpnI and XhoI.

The thrombin cleavable mRuby2-fLOV2 (PL0202), from here on referred to as mRuby2-thr-fLOV2, was generated by inserting the thrombin cleave site LVPRGS into PL0201 via whole plasmid mutagenesis with phosphorylated primers PR03 and PR04.[28] The corresponding mammalian expression construct PL0302 was generated by cloning PL0202, with primers PR07 and PR08, into the pcDNA3.1 vector using KpnI and XhoI.

The spring-linked mRuby2-fLOV2 (PL0303), from here on referred to as mRuby2-coil-fLOV2, was generated by inserting the flagelliform sequence from PL0400 between the mRuby2 and fLOV2 genes. PL0400 VinculinTS was a gift from Martin Schwartz (Addgene plasmid # 26019).[29] Due to difficulty in designing specific primers for the surrounding base pairs, the flagelliform insert was synthesized by Integrated DNA Technologies with flanking BamHI and NheI restriction sites. This sequence was then cloned into PL0301 using those two restriction sites to generate PL0303.

3.4.2 Molecular Cloning

Primer Design
The gene or DNA fragment of interest was identified and an appropriate insertion site in the plasmid vector was located with restriction site(s) that do not appear in the segment of interest. Primers were designed in the SnapGene viewer software with the following criteria in mind:

primer included at least 18 base pair overlap with template, primer had 40-60% GC content, primer included a GC clamp on the 3' end consisting of 5 bases with 2 or 3 bases of G or C to promote strong bonding to template, primers with restriction sites on the 5' end not binding to template included a 5 base pair lead to promote optimal restriction enzyme binding on cloning products, and primer pairs had melting temperatures within 2ºC of each other. Primers were synthesized by Integrated DNA Technologies.

Polymerase Chain Reaciton (PCR)
The VENT DNA polymerase kit (New England Biolabs) was used for short inserts up to the length of 6000 base pairs. Approximately 500ng of DNA template and 1uM of each primer was used for 4 reactions on a temperature gradient around the calculated optimal annealing temperature. Nuclease-free water, 10x polymerase buffer, DNA template, primers, salts, dNTP's, and VENT polymerase were mixed in a reaction solution on ice according to VENT kit instructions to a final volume of 200uL. The reaction solution was distributed to 4 PCR reaction tube at 50uL per reaction. Polymerase chain reactions were conducted in a BioRAD C1000 Touch Thermal Cycler according to VENT kit instructions. Briefly, the DNA template was denatured at 95ºC for 3 minutes, then the following 3 steps were repeated for 25 cycles: 30 second denaturation at 95ºC, 30 second annealing on a gradient according to calculations, and 1 minute of extension at 72ºC per kilo base pair of product. At the end of the cycles, a further 5 minutes of extension is added. Finally, the thermal cycler is set to hold temperature at 4ºC until further processes are ready.

The KAPA HiFi HotStart ReadyMix (Kapa Biosystems) was used for longer inserts up to 20,000 base pairs and for site-directed mutagenesis. Approximately 4ng of DNA template and 0.3uM of each primer was used for 2 reactions at two temperature points higher than the calculated optimal annealing temperature due to the high salt content of the KAPA reaction buffer. Polymerase chain reactions were conducted in a BioRAD C1000 Touch Thermal Cycler according to kit instructions. Briefly, the DNA template was denatured at 95ºC for 2 minutes, then the following 3 steps were repeated for 18 cycles: 20 second denaturation at 98ºC, 30 second annealing, and 30 seconds of extension at 72ºC per kilo base pair of product. At the end of the cycles, a further 6 minutes of extension is added. Finally, the thermal cycler is set to hold temperature at 4ºC until further processes are ready.

PCR product was verified via gel electrophoresis. Agarose gels were prepared at 0.75% or 1% based on length of PCR product. The PCR products were run on the gel with a DNA ladder and quickly visualized on a UV table for size reference. The best looking lane of each set was chosen to be purified and used in subsequent steps. The PCR product was purified out of the agarose gel using the QiaQuick DNA extraction kit (Qiagen). The purified DNA product was measured on a Nanodrop for concentration and purity.

Restriction Digest and Ligation
FastDigest (Fermentas) restriction enzymes were used for restriction digest of the required restriction sites to create sticky ends. For each digest, up to 1ug and up to 2uL of DNA was digested with 1uL of each enzyme in a 20uL reaction solution of FastDigest buffer. The reaction was incubated at 37ºC for 10 minutes to 2 hours depending on the enzymes involved, and subsequently heat inactivated at 80ºC for 10 minutes and cooled to room temperature before

proceeding with ligation. For vector digestion, FastAP Alkaline Phosphatase (Thermo Scientific) was included in the digest reaction to prevent reformation of initial vector. When using site-directed mutagenesis and unpuried PCR products, DpnI was used to digest methylated template DNA to ensure only PCR products were transformed into competent cells in the following step.

Quick Ligase (New England Biolabs) was used to insert the PCR product into the desired vector at ratios of 3:1 to 10:1 vector:insert molar ratios or simply to rejoin two ends of site-directed mutagenesis PCR product. In a 30uL reaction, 14uL of vector and insert from the digestion step were added at the correct ratio to 15uL of 2x QuickLigase buffer and 1uL of Quick Ligase. The reaction solution was mixed well and incubated at room temperature for 10 minutes.

Transformation
The ligated product was chilled on ice and transformed into XL1-blue competent E. coli cells and streaked onto the appropriate antibiotic-containing LB-agar plate for colony growth overnight at 37ºC. Briefly, the competent cells were thawed on ice and incubated on ice for 30 minutes after adding plasmid. The cells were then placed in 42ºC heat shock for 45 seconds. Finally, the cells were cooled on ice for 1-2 minutes before adding SOC medium and shaking at 37ºC for the initial outgrowth of 45 minutes to allow antibiotic resistance build up before streaking onto antibiotic-containing plates. Colonies were picked the next day for small 5 mL liquid culture outgrowth overnight in LB media containing the appropriate antibiotic, shaking at 37ºC. The liquid cultures were purified by mini-prep and sequenced to verify product. A small fraction of each liquid culture was frozen in 25% glycerol for future use.

3.4.3 Protein Expression

Previously sequence-confirmed plasmids were transformed into BL21 competent *E. coli* cells and streaked onto the appropriate antibiotic-containing agar plate for colony growth overnight. Multiple colonies were collected next day for expression. The colonies were inoculated into progressively larger liquid cultures of 3mL, 20mL, and 1L of TB containing the appropriate antibiotic at 37ºC. The smaller cultures were added to the next size when the solution became sufficiently cloudy that the outline of a finger could not be seen through the vial. The OD600 of the final 1L culture was measured at intervals until it reached the growth phase at approximately 0.4-0.8. At this point, the temperature was lowered to 16ºC and the protein expression induction drug was added. In these experiments, the vector pSKB3 was used for protein expression and IPTG was added at 500uM for induction. The culture was allowed to express overnight at 16ºC.

Protein Purification
The proteins were designed with a 6x histidine tag on the N-terminus for purification using NiNTA affinity columns. The buffers listed in Table 3.3 were prepared ahead of time and kept at 4ºC. The day before purification, all buffers and MilliQ water were degassed to prevent bubble formation in the NiNTA column. The overnight expression culture of BL21 was centrifuged at 4300rpm at 4ºC for 15 minutes. The supernatant was carefully decanted into bleach for disposal. The pellet was resuspended in lysis buffer and placed on a shaker in 4ºC for 30 minutes. Then solution was then homogenized twice in the Avestin C3 homogenizer (UC Berkeley MacroLab) using the homogenizer prep buffer for machine prep. The homogenized sample was centrifuged at 14,500rpm at 4ºC for 20 minutes to remove debris. The supernatant was filtered through a

40um Millipore Steriflip filter unit before purification on the NiNTA column. The NiNTA column was first prepared by washing with 6 volumes of MilliQ water, then equilibrated with 6 volumes of column prep buffer, pushed through using a syringe pump at 2mL/minute. The homogenized and filtered protein sample was loaded into a syringe and allowed to settle while column is being prepared to reduce air bubbles. The protein sample was loaded into the column while preventing introduction of air bubbles and washed with 6 volumes of wash buffer; flow through was collected for comparison in SDS-PAGE. The column was then eluted with 6 volumes of elution buffer, collecting 500uL-1mL fractions. The column was finally washed with 6 volumes of MilliQ water and store at 4ºC for future purification of the same protein. The purified protein was desalted to remove imidazole and exchanged into either base buffer or final exchange buffer. Protein concentration of all collected samples was approximated using the Bradford assay. SDS-PAGE was used to verify protein presence and purity, using all intermediate steps of purification as comparison. When necessary, the protein was concentrated using Amicon and Millipore protein concentrating centrifuge filters. When freezing proteins, 10% glycerol was added to aid in preservation.

Assessing Fluorescent Protein Maturity in vitro
The minimal mRuby2-fLOV2 recombinant protein 0201 was assessed for maturity after purification based on absorption measurements. Protein 0201 was diluted to 100uM in base buffer and aliquoted into 9 cuvettes. These 9 samples were divided into 3 groups: maturation at 4°C, room temperature, and 37°C. All samples were protected from light. Absorption measurements were taken at t = 0, 1hr, 2 hr, 3 hr, 5 hr, 20 hr, 48 hr. At t = 48 hr, excitation and emission scans were also taken.

Maturation for mRuby2 Recominant Proteins
After the first expression attempt, all recombinant proteins containing mRuby2 were matured prior to experiments. The tube containing protein was wrapped in foil and placed on a shaker at room temperature to mature for 48 hours. At the end of the maturation period, samples were gently spun in a low power mini-centrifuge to collect any precipitated protein into a pellet. The supernatant was removed and retained for future experiments. The pellet was discarded.

3.4.4 Assessment of mRuby2-thr-fLOV2 FRET via thrombin cleavage

mRuby2-thr-fLOV2 was diluted to 5μM in final exchange buffer. Thrombin was added to 1mL of mRuby2-thr-fLOV2 to a final concentration of 800μg/mL. The samples were incubated at room temperature and immediately after adding and thoroughly mixing thrombin, the t=0 time point was taken, and subsequent time points were taken every 5 minutes until fluorescence profile no longer changed. Emission profiles were taken on an Aminco Bowman Series 2 luminescence spectrometer using a 445nm excitation and collecting emission from 480nm to 700nm. At the beginning and end of the experiment, anisotropy measurements for fLOV2 were also taken and averaged from 500nm to 550nm. FRET efficiency of mRuby2-thr-fLOV2 was calculated by comparing fLOV2 fluorescence before and after thrombin cleave, measuring between 480nm and 540nm. 540nm was used as a cutoff to discount any direct excitation of mRuby2 using 445nm. Although mRuby2 absorption at 445nm is low, it is not zero. Assuming that all proteins were cleaved at the thrombin recognition site, the integrated fLOV2 fluorescence from 480nm to 540nm at the end of the experiment can be used as the 100% fluorescence

standard ($F_{100\%}$). The same integrated fluorescence of the protein solution taken at t=0 (F_{FRET}) can be used as a point of comparison. The estimated FRET efficiency based on thrombin cleavage of mRuby2-thr-fLOV2 is therefore $E = 1-(F_{FRET}/F_{100\%})$. These calculations also assumed that the protein solution is dilute enough that random events of FRET between free-floating fLOV2 and mRuby2 proteins are negligible.

Measurement of fluorescence anisotropy
Fluorescence anisotropy of fLOV2 was calculated using multiple measurements of the same sample. The sample was excited using 445nm. For each sample, 4 measurements were taken with excitation polarized at 90° angle to each other and polarized emission collected parallel and perpendicular to both angles of polarized excitation. Although theoretically 2 measurements taken with polarized excitation with parallel and perpendicular emission should suffice, the 4 different permutations of possible filter combinations serve to eliminate instrument related sensitivity differences in measuring light at different angles.

3.4.5 Cell culture

Plasmid constructs in mammalian expression vectors were expressed *in vitro* in 293T HEK cells and 3T3 fibroblast cells. Cells were maintained in growth medium (DMEM with 10% FBS and 1% penicillin/streptomycin) in sterile incubators set to 37°C with 5% carbon dioxide and controlled humidity. Cells were passaged every 2-3 days at approximately 75% confluence at a ratio of 1:20.

Plasmid transfection
Prior to transfection with DNA plasmid of interest, cells were counted and passaged into 24 well plate wells. 3T3's were seeded at 25,000 cells per well and 293T's were seeded at 50,000 cells per well, with 500μL total media in each well. Cells were grown for 24 hours to 75-90% confluence prior to transfection. Immediately before transfection, the growth media was changed to transfection medium (DMEM with 10% FBS) at 400μL per well. Plasmids were transfected with Lipofectamine2000 (ThermoFisher) as a transfection reagent using the following protocol. For each well in a 24 well plate, 500ng of plasmid and 1.5μL of Lipofectamine2000 were used. Lipofectamine2000 and plasmids were separately mixed into 50μL each of plain DMEM or OptiMEM (ThermoFisher) for 5 minutes at room temperature, after which the two solutions were mixed together and incubated for another 20 minutes before adding to cells. The final medium contained 500ng of DNA plasmid and 1.5μL of Lipofectamine2000 in a 100μL volume added to 400μL transfection medium. The transfection medium was replaced with fresh growth medium after 6 hours.

Cells were passaged 24 hours after transfection onto 35mm dishes with a 20mm glass bottom center for confocal imaging. The glass bottom center was first coated with 0.1% gelatin for half an hour before cell seeding. 3T3's were seeded at 10,000 per dish, and 293T's were seeded at 5,000 per dish. Cells were only seeded on the glass bottom center with 500μL of growth medium. Cells were grown overnight to 3 days before conducting imaging studies.

Confocal imaging
Cells were imaged on a Zeiss LSM700 laser scanning confocal microscope with an incubation chamber set to 37°C and 5% carbon dioxide. Prior to imaging, the microscope was turned on and the incubation chamber was warmed up for half an hour both to prepare for cell health and to equilibrate objectives to 37°C. A 63x oil immersion objective and a 20x air objective were used for imaging of all samples.

Imaging of fLOV2/mRuby2 FRET pair used the following settings unless otherwise noted. fLOV2 was excited using a 405nm laser at 10%, and mRuby2 was excited using a 555nm laser at 5%. The fLOV2 channel was collected from 450nm to 550nm to eliminate mRuby2 bleedthrough. The mRuby2 channel was collected from 580nm to 700nm. Acceptor photobleaching was done using 555nm laser at 100% until channel 2 fluorescence was reduced to background level. FRET efficiency was measured using background-corrected fluorescence intensities of fLOV2 before and after bleaching.

3.5 Results and Discussion

3.5.1 fLOV2-mRuby2 FRET pair design

mRuby2 was chosen to be the FRET acceptor to fLOV2 based on various criteria. Due to the green-emitting spectrum of fLOV2 (Figure 3.1a), likely candidates for acceptor are narrowed to those proteins with excitation peaks in the range of 500-600nm. While proteins with excitation closer to 600nm are likely to provide a better emission separation, they will also have much less spectral overlap required for FRET to occur. Simultaneously, the emission peak of the acceptor protein should be above 575nm to reduce the amount of overlap. Within these guidelines, mRuby2 emerged as a viable candidate with one of the highest extinction coefficients (113,000) among the red-emitting fluorescent proteins.[27]

Further examination showed that mRuby2 was, indeed, a good theoretical match for fLOV2. Compared to mTFP1/Venus, one of many recently improved FRET pairs and one used in further FRET studies in Chapter 4 of this thesis, fLOV2/mRuby2 displays similar amount of spectral overlap of donor emission with acceptor excitation with lower emission overlap between donor and acceptor (Figure 3.3).[14] When compared to Clover, the initially published FRET donor paired with mRuby2, fLOV2's larger Stokes shift allows for use of excitation wavelengths below 450nm, which greatly reduces direct excitation of mRuby2.[27] A larger overlap integral is also expected for fLOV2/mRuby2 compared to Clover/mRuby2.

When comparing filters and channels used in fluorescence imaging of all 3 FRET pairs, fLOV2/mRuby2 greatly reduces the proportional donor bleedthrough compared to mTFP1/Venus but not Clover/mRuby2 (Figure 3.4).

Calculation of the FRET efficiency curve based on measured spectra using Eqns 1-3 gives a theoretical Förster radius of 5.9nm, using a κ^2 value of 2/3 for random orientation of donor and acceptor, the measured quantum yield of LOV2 at 0.44, and extinction coefficient for mRuby2 of $113,000 M^{-1}cm^{-1}$ at 559nm.[19,27] The exact quantum yield of fLOV2 was unable to be reliably measured, however, it is assumed to be very similar to the value cited. Although it is only an

estimate, this R_0 value of 5.9nm was tested against the measured FRET efficiency of mRuby2-thr-fLOV2 in the next section and appears to be a good approximation. More accurate quantum yield measurements are required to obtain the true Förster radius.

3.5.2 RubyLOV characterization in solution

mRuby2-fLOV2 maturation
The minimal mRuby2-fLOV2 recombinant protein 0201 expressed in BL21 *E. coli* required extra maturation after purification from cell lysates. A dilute buffered solution of the protein appeared a pale yellow to the naked eye (Figure 3.5b), in contrast to the expected strong visual presentation of mRuby2 protein. Initial absorption measurements on an UV-vis spectrometer showed no excitation peak for mRuby2. Although characteristic peaks for fLOV2 appeared to be present at 445nm and 475nm, background absorption made it difficult to discern (Figure 3.5a). However, fLOV2 fluorescence was visually verified with handheld UV lamp.

In its initial publication, mRuby2 required 150 minutes to reach half of maximum fluorescence after exposure to oxygen.[27] Perhaps due to differences in expression systems, this fast maturation was not seen in these experiments. Attempts to express protein at 25°C, 30°C, or 37°C dramatically increased the presence of expressed protein in inclusion bodies instead of in solution after cell lysis. Presence of protein in inclusion bodies was verified by visualizing fLOV2 fluorescence using a handheld UV lamp. After lysis and homogenization, fLOV2 fluorescence was found mostly in the cell debris pellet rather than the supernatant as expected. While it is possible to retrieve protein from inclusion bodies, the following successful attempt to mature mRuby2 post purification eliminated the need.

Further study showed that mRuby2 was indeed incompletely matured during expression and required incubation post purification. Samples of protein 0201 incubated at 4°C, room temperature (RT), and 37°C showed that the characteristic absorption peak of mRuby2 at 559nm slowly appeared over a period of 2 days. The samples incubated at 37°C matured the fastest and reached maximum mRuby2 absorption by 20 hours, reaching over 80% of maximum absorption by 5 hours. The samples incubated at 4°C showed very little improvement after 48 hours and appears to be incompletely mature still. Visual inspection of samples confirmed increase in mRuby2 fluorescence by the increased intensity of sample solutions' pink hue (Figure 3.5b). Following the maturation study, all future expressed mRuby2-fLOV2 samples were matured according to stated methods. The maturation results for the 37°C protein samples appear on par with published maturation time.

The maturation process of mRuby2-fLOV2 gave a preliminary indication of FRET being present in this conjugate protein. The room temperature and 37°C samples had almost identical emission profiles when excited at 450nm due to both samples having matured mRuby2 as seen on the absorption spectra (Figure 3.5c). However, the less matured 4°C sample showed a very interesting emission profile with higher fLOV2 fluorescence and lower mRuby2 fluorescence. While mRuby2 fluorescence difference may be explained by the higher concentration of matured mRuby2 in the RT and 37°C samples, it was unlikely to show such a large difference using 450nm excitation due to the extremely low excitation of mRuby2 at this wavelength. Similarly, the difference in fLOV2 fluorescence may be explained by protein degradation in the samples

incubated at higher temperatures, but this was unlikely to be the case due to similar fLOV2 absorption levels (Figure 3.5a). The logical conclusion was therefore that there is FRET occurring between fLOV2 and mRuby2. All 3 samples contained similar concentrations of fLOV2. However, the two higher temperature samples contained higher concentrations of matured mRuby2. When excited at 450nm, the majority of the absorption was due to fLOV2 excitation, but with the presence of the mRuby2 acceptor, emission came from both proteins. The RT and 37°C had higher concentrations of mature mRuby2 and therefore higher rates of FRET. This reduced fLOV2 direct emission and increased mRuby2 sensitized emission when compared to the 4°C sample (Figure 3.5c).

Further evidence and characterization of FRET properties were conducted on the thrombin cleavable protein mRuby2-thr-fLOV2.

Thrombin cleavable protein display FRET
The thrombin cleavable protein mRuby2-thr-fLOV2 was designed specifically for assays of FRET efficiency. With the inclusion of the 6 amino acid long recognition sequence (LVPRGS), the mRuby2-thr-fLOV2 protein is only 4 amino acids longer than the minimal mRuby2-fLOV2 protein. Therefore, it should reasonably simulate the close proximity interactions of donor and acceptor at the shortest distance. However, there is the consideration that such a short linker may restrict the random orientation of both proteins with respect to each other, limiting their dipoles to couple at less than optimal angles or preventing closer proximity of donor to acceptor that a longer and more flexible linker may otherwise allow.

The thrombin cleave assay showed that mRuby2-thr-fLOV2 indeed exhibited FRET. Over the course of 40 minutes, during which thrombin was added to the protein solution to physically cleave and separate mRuby2 from fLOV2, fLOV2 fluorescence gradually increased while mRuby2 fluorescence decreased when excited at 445nm (Figure 3.6). Using this data, FRET efficiency was calculated at 43%. Time points taken after 40 minutes did not further decrease mRuby2 fluorescence.

Because 445nm was used for excitation of the sample, emission of mRuby2 seen in each time point measurement was most likely a result of sensitized emission due to FRET between fLOV2 and mRuby2. The change in emission profile further confirmed the presence of FRET in the conjugate protein. While linked with a 10 amino acid spacer, the donor and accepter fluorophores were at an estimated 6nm apart based on the structure of the protein; the 10 amino acid spacer is approximately 3.5nm long assuming loose linear arrangement based on calculations of bond lengths and angles, the distance from the C terminus of mRuby2 to its central fluorophore is approximately 2nm, and the distance from the N terminus of fLOV2 to its central fluorophore is approximately 0.5nm. This distance lies within the optimal range of most FRET pairs and certain within the optimal range of fLOV2/mRuby2 based on previous calculations. This distance is confirmed by using Eqn 1. With a calculated Förster radius of 5.9nm and the measured FRET effiency of 43%, the distance between donor and acceptor fluorophores in mRuby2-thr-fLOV2 is estimated to be 6.1nm. However, given a solution of 5uM of protein, if the reaction proceeded to completion, there would be 10uM total of protein, with an estimate of 11.9nm or more between any two proteins, assuming even dispersal. This gives under

1% calculated FRET efficiency between any two free-floating fLOV2 and mRuby2 molecules. Direct excitation of mRuby2 at 445nm is also very low.

Given these circumstances, a comparison of fLOV2 fluorescence in mRuby2-thr-fLOV2 before and after thrombin cleavage should provide a reasonably accurate estimate of FRET efficiency of this fluorophore pair in this conformation within 1-2%. The measurement taken at t = 40 minutes showed a small amount of mRuby2 emission (Figure 3.6b) and this could be attributed to possibly both direct excitation and chance events of FRET in solution. To help eliminate the contribution of these factors, future testing can be conducted at a lower wavelength, such as 405nm, and with a lower concentration of protein. An initial protein solution of 2uM would better ensure that free-floating donor and acceptor proteins after cleavage have very little chance of coupling.

fLOV2 potential as fluorescence anisotropy tag
Though not fully explored in this chapter, preliminary results of fLOV2 characterization indicate that fLOV2 has the potential to be useful as a fluorescence anisotropy marker of protein interactions due to its small size and long fluorescence lifetime.

Measurement of fluorescence anisotropy can be a very powerful tool for analyzing protein-protein interaction within the cell due to its sensitivity to protein size. Using a polarized light source, only fluorophores whose dipole moments align with the orientation vector of the incident light will become excited. Given enough time, the excited fluorophores will diffuse and rotate to change from an identically oriented population to a randomly oriented one. This process is known as depolarization. The randomly oriented population is described as isotropic, or identical in every direction, as opposed to polarized, or biased towards a certain direction. However, chances are, the excited fluorophore population will not be fully depolarized by the time light is emitted, resulting in polarization in the emitted light as well. Anisotropy is, therefore, a measurement of polarization. Both anisotropy and polarization are used to describe the same concept, however, the mathematical representations are somewhat different.[30] In the following discussion, anisotropy will be used as the primary measurement.

The fluorescence anisotropy of the emitted light is highly dependent upon two factors, fluorescence lifetime and the rotational correlation time. A fluorophore's fluorescence lifetime is defined as the time it takes for emitted fluorescence to decay to 1/e (0.37) of the measured value at t = 0, and the rotational correlation time is the average time for a molecule to rotate 1 radian, or 57.3°. If the fluorescence lifetime is much longer than the rotational correlation time, the anisotropy will be low as the proteins will have had time to rotate into a more randomly oriented population before the photon is emitted. Inversely, if the rotational correlation time is much longer than the fluorescence lifetime, anisotropy will be high.

The rate of rotation of a molecule is, in turn, dependent on the molecule's size and shape, as well as the temperature and viscosity of its surrounding medium. Logically, if a molecule is large, it will diffuse and rotate more slowly than a smaller molecule due to its bigger moment of inertia. Similarly, the shape of the molecule also affects its moment of inertia. Temperature directly affects the energy of a molecule and therefore how quickly it rotates. And lastly, the viscosity of the solution determines the amount of drag on the moving molecule, with higher viscosity

slowing it down. The depolarization process is also affected by factors such as light scattering and resonance energy transfer (e.g. FRET).[30]

Given this background on the theory of anisotropy, it is easy to understand how this measurement may apply to protein interactions. When bound to a target protein through an attached recognition peptide, a fluorescent marker is no longer free-floating and has, in a physical sense, become a larger combined entity with the target protein. This causes rotation time to increase and therefore increasing anisotropy in the measurement of fluorescence emission. The larger the anisotropy change after binding, the more sensitive the system is to small subpopulation interactions between the fluorescent tag and the target protein. Fluorescence anisotropy has also been used in combination with FRET to better resolve direct versus sensitized emission, since sensitized emission is bound to be highly depolarized.[31] However, fLOV2 is unlikely to hold an advantage in this specific application of FRET, as it would not require a donor with a low anisotropy.

When compared to GFP type proteins, fLOV2 is highly advantageous as an anisotropy tag. GFP and its homologs are bulky, and this places on them certain limitations when it comes to applications in fluorescence anisotropy. EGFP is approximately 27kDa with barrel length and diameter of 4.2nm and 2.4nm, respectively. In an aqueous solution, the fluorescence anisotropy of EGFP alone was measured to be 0.292±0.009.[32] For reference, the max possible anisotropy value is 0.4. mRuby2 fluorescence anisotropy measured after the thrombin cleave experiment was calculated to be 0.3. It must be noted that this value was calculated using mRuby2 still attached to the 6xHistidine tag and the TEV cleavage domain included on the N terminus of *E. coli* expressed proteins for purification purposes, mRuby2 alone is likely to have a slightly smaller anisotropy measurement. The similarity in the values is expected due to their common origin. Given a measured fluorescence lifetime of 2.57ns for EGFP and a rotational correlation time of 10.6ns in an aqueous solution, there is not enough time for EGFP to depolarize within the lifetime of the fluorophore, resulting in the large measured anisotropy.[18] Another factor that must be considered, however, is that the intracellular environment is somewhat more viscous than water, estimated at 1.5cP, with local viscosity varying from similar to that of water (1cP) to as high as 400 cP in live cells.[33,34] With increased viscosity comes increase in rotational correlation time and therefore a high anisotropy of EGFP alone.

In order to use a fluorescent protein as an anisotropy-based tag, it must be attached to a target recognition peptide, or perhaps even a small protein. This further increases the baseline anisotropy of EGFP and its homologs. With the initial measurement of 0.29 being so close to the maximum anisotropy of 0.4, these increases leave very little room for sensitivity in the sensor and makes it more susceptible to influence by noise in the data. fLOV2, however, is much smaller with an approximate molecular weight of 12kDa and fluorescence lifetime of 4.6ns. It is both smaller and longer lived than GFP, both factors contributing to a smaller baseline anisotropy. fLOV2's anisotropy is measured to be 1.8 in an aqueous solution, providing more flexibility for binding detection.

3.5.3 RubyLOV expression in vitro

Both minimal mRuby2-fLOV2 and mRuby2-thr-fLOV2 expressed easily in 293T's. A third protein, mRuby2-coil-fLOV2, was designed to include a peptide spring and also expressed well in 293T's. This third protein was designed as a precursor to a FRET-based tension sensor. The "coil" inserted between the FRET pair was previously used by Grashoff et al. in a vinculin tension sensor.[29] Originating from a spider silk protein, the flagelliform peptide has naturally spring-like properties. It consists of repeats of a 5 amino acid sequence (GPGGA) that form tight coils of 10 amino acids per turn. In their 2010 paper, Grashoff et al. used a 8x repeat (40 amino acids) of this format between mTFP1 and Venus to create a FRET tension sensor sensitive to 1-6pN of force. Although not explored in this chapter, this spring-like peptide provide innumerable possibilities in the mechanosensing of intracellular processes.

All three fLOV2/mRuby2 proteins were expressed unattached to any functional target proteins and were therefore evenly distributed throughout the cell as soluble proteins. Upon each transfection, generally 5-10% of cells expressed the transfected proteins. Many variations of the transfection protocol were attempted without significant improvement in expression level. It is possible that the inclusion of a Kozak consensus sequence may improve expression level, however, this was not explored for these proteins.[35] It was, however, attempted in the experiments described in Chapter 4 with successful increase in expression and measurable fluorescence level.

Whole cell acceptor photobleaching was conducted on expressing cells, mainly 293T's. Based on the structure of the constructs, it was expected that minimal mRuby2-fLOV2 would exhibit the largest amount of FRET, and mRuby2-thr-fLOV2 the least, with mRuby2-coil-fLOV2 somewhere in between based on the length of their spacers between the two fluorescent proteins. The minimal mRuby2-fLOV2 has the two proteins separated by 6 amino acids, mRuby2-thr-fLOV2 has a 10 amino acid spacer, and mRuby2-coil-fLOV2 has a 40 amino acid tightly wound peptide spring with 2 amino acids on each end. Although, mRuby2-coil-fLOV2 would initially seem longer than mRuby2-thr-fLOV2 due to the large spring construct between the two proteins, the 40 amino acid coil actually only has an estimated zero-force length of 1.3nm.[29]

There was significant variability of measured FRET within expressing cells of each protein. This may be due to unstable and/or uneven expression. Nevertheless, measurements of FRET of the three constructs expressed in 293T's approximately agreed with the relative relationships of the inter-fluorophore distances of the three proteins (Figure 3.7). The minimal mRuby2-fLOV2 had a FRET efficiency of 47.3±9.4%. The mRuby2-coil-fLOV2 protein had a FRET efficiency of 51.0±19.5%. The difference in FRET efficiencies of these two is not statistically significant. However, both were significantly higher in FRET efficiency when compared to mRuby2-thr-fLOV2, which had a FRET efficiency of 28.3±4.1%, which was expected based on their structures. Figure 3.8 shows the fluorescence change in fLOV2 before and after acceptor photobleaching in a representative cell of each FRET construct.

Interestingly, the FRET efficiency of mRuby2-thr-fLOV2 measured in 293T cells was much lower than that measured in solution (43%). This may be a result of many factors. The intracellular environment may be affecting both the protein conformation and the fluorophore

properties. This change in environment could result in a change in quantum yield of the donor and/or extinction coefficient of the acceptor, both leading to changes in FRET efficiency. It may also be that at the time of measurement, mRuby2 was not fully matured, which would throw off the expected 1:1 ratio of matured donor to acceptor in all three recombinant proteins. Prior tests indicated that mRuby2 maturation at 37°C occurred in the time frame of less than 10 hours. Given the time line of experimentation from transfection to imaging, mRuby2 should be fully matured, unless protein expression is significantly delayed post-transfection. It is more likely that environmental changes have affected the dynamics of the fLOV2/mRuby2 FRET pair. This must be confirmed with FLIM measurements

An additional noteworthy observation is that the mRuby2-coil-fLOV2 FRET pair seemingly shows a higher FRET efficiency than the previously published TSMod (mTFP1-coil-Venus) on which this construct is based. TSMod exhibited a zero-force FRET efficiency of ~23.5%.[29] The significance of this difference cannot be verified with the given data, nonetheless, it is a possibility. Although the fLOV2/mRuby2 FRET pair (R_0 = 5.9nm) has a shorter Förster radius than mTFP1/Venus (R_0 = 6.3nm), fLOV2's smaller size and surface-accessible fluorophore brings the donor and acceptor closer together. This shorter inter-fluorophore distance may well compensate for the shorter Föster radius when compared to mTFP1/Venus. Assuming this is the case, they may be comparable in terms of FRET function. However, fLOV2/mRuby2 still holds the advantage of being a smaller construct with reduced steric hindrance and interference with target functions.

3T3 fibroblast cells were also used for these experiments. Expression in 3T3's was much more difficult than in 293T's and very few data points were acquired as a result. The few cells that were able to be tested for FRET efficiency of mRuby2-coil-fLOV2 seemed to indicate lower FRET efficiency of the same construct in 3T3's when compared to 293T's. This may be a function of expression level and maturation and must be further explored to expand the applicability of this FRET pair in a diverse array of cell types. Once again, Kozak sequence inclusion is an important factor to consider. Codon optimization for specific species may also improve both expression level and the correct folding of the protein, as abnormal translation speed due to the abundance of rare codons in the mRNA sequence may lead to misfolding and aggregation.[36]

The reversal of fluorescent protein orders was briefly investigated to create recombinant proteins with fLOV2 on the N terminus and mRuby2 on the C terminus. However, little difference was seen in the FRET potential of the reversed proteins and they were not used in further studies.

3.6 Conclusion

In this chapter, fLOV2 was introduced and explored as a fluorescent protein tag for research use *in vitro*. Compared to GFP and its homologs, fLOV2 holds certain advantages such as having a much smaller mass and being able to anaerobically mature and function. Specifically, the pairing of fLOV2 with mRuby2 was examined in more depth and characterized for their FRET properties. Comparing to currently available protein FRET pairs, fLOV2/mRuby2 show promise with its photophysical properties. Its Förster radius and resulting FRET efficiency is comparable to many of the best FRET protein pairs available presently, and the smaller size of fLOV2

reduces the bulk of the whole recombinant protein. Much remains to be done to verify and measure fLOV2 fluorescent properties at a more accurate level. Intracellular FLIM measurements must be conducted to verify fLOV2 function within the cell as compared to in solution. An accurate quantum yield measurement of fLOV2 is necessary to fully characterize its capabilities as a fluorescent reporter. Furthermore, crystallography of fLOV2/mRuby2 FRET constructs would be very useful in determining their FRET properties. Despite the lack of comprehensive information regarding this FRET pair, current data suggest much promise and fLOV2/mRuby2 warrants a more broad look and study of its possibly applications in intracellular activity sensing.

Since the conception of this FRET pairing between fLOV2 and mRuby2, an improved mRuby3 has been published by the group that made mRuby2 and is worth investigating as a possible FRET acceptor for fLOV2 in future studies.[37]

3.7 References

1. Valeur, B. & Berberan-Santos, M. N. A brief history of fluorescence and phosphorescence before the emergence of quantum theory. J. Chem. Educ. 88, 731–738 (2011).

2. Stokes, G. On the Change of Refrangibility of Light. *Philos Trans R Soc Lond*. 142, 463-562 (1852).

3. Lakowicz, J. *Principles of Fluorescence Spectroscopy*. 5-7. (Springer Science & Business Media, 2013).

4. Zimmer, M. Green fluorescent protein (GFP): Applications, structure, and related photophysical behavior. *Chem. Rev*. 102, 759–781 (2002).

5. Shimomura, O., H. Johnson, F. & Saiga, Y. Extraction, Purification and Properties of Aequorin, a Bioluminescent Protein from the Luminous Hydromedusan, Aequorea. J. Cell. Comp. *Physiol*. 1353, 223–239 (1962).

6. Prasher, D. C., Eckenrode, V. K., Ward, W. W., Prendergast, F. G. & Cormier, M. J. Primary structure of the Aequorea victoria green-fluorescent protein. *Gene* 111, 229–233 (1992).

7. Chalfie, M., Tu, Y., Euskirchen, G., Ward, W. W. & Prasher, D. C. Green fluorescent protein as a marker for gene expression. *Science*. 263. 802-805 (1994).

8. Heim, R., Cubitt, A. B. & Tsien, R. Y. Improved green fluorescence. *Nature* 373, 663–664 (1995).

9. Chudakov, D., Matz, M., Lukyanov, S. & Lukyanov, K. Fluorescent Proteins and Their Applications in Imaging Living Cells and Tissues. *Physiol Rev*. 90, 1103–1163 (2010).

10. Shaner, N. C., Steinbach, P. A. & Tsien, R. Y. A guide to choosing fluorescent proteins. *Nat Methods*. 2, 905–909 (2005).

11. Chapman, S. et al. The photoreversible fluorescent protein iLOV outperforms GFP as a reporter of plant virus infection. *Proc. Natl. Acad. Sci*. U. S. A. 105, 20038–43 (2008).

12. Mukherjee, A., Walker, J., Weyant, K. B. & Schroeder, C. M. Characterization of Flavin-Based Fluorescent Proteins: An Emerging Class of Fluorescent Reporters. *PLoS One* 8, (2013).

13. Förster, T. Intermolecular Energy Migration and Fluorescence. *Ann Phys*. 2. 55-75 (1948).

14. Day, R. N. & Booker, C. F. Characterization of an improved donor fluorescent protein for Förster resonance energy transfer microscopy. *J. Biomed. Opt*. 13, 031203 (2008).

15. Patterson, G. H., Piston, D. W. & Barisas, B. G. Förster Distances between Green Fluorescent Protein Pairs. *Anal. Biochem*. 284, 438–440 (2000).

16. Vogel, S. S., Thaler, C. & Koushik, S. V. Fanciful FRET. *Sci. STKE* 2006, re2 (2006).

17. Riedl, J. et al. Lifeact: a versatile marker to visualize F-actin. *Nat. Methods* 5, 605–607 (2008).

18. Hink, M. A. et al. Structural dynamics of green fluorescent protein alone and fused with a single chain Fv protein. *J. Biol. Chem*. 275, 17556–17560 (2000).

19. Buckley, A. M., Petersen, J., Roe, A. J., Douce, G. R. & Christie, J. M. LOV-based reporters for fluorescence imaging. *Curr. Opin. Chem. Biol*. 27, 39–45 (2015).

20. Herrou, J. & Crosson, S. Function, structure and mechanism of bacterial photosensory LOV proteins. *Nat. Rev. Microbiol*. 9, 713–723 (2011).

21. Wu, Y. I. et al. A genetically encoded photoactivatable Rac controls the motility of living cells. *Nature* 461, 104–108 (2009).

22. Wang, H. et al. LOVTRAP: an optogenetic system for photoinduced protein dissociation. *Nat. Methods* 13, 755–8 (2016).

23. Swartz, T. E. et al. The Photocycle of a Flavin-binding Domain of the Blue Light Photoreceptor Phototropin. *J. Biol. Chem*. 276, 36493–36500 (2001).

24. Salomon, M., Christie, J. M., Knieb, E., Lempert, U. & Briggs, W. R. Photochemical and mutational analysis of the FMN-binding domains of the plant blue light receptor, phototropin. *Biochemistry* 39, 9401–9410 (2000).

25. Christie, J. M. et al. Structural tuning of the fluorescent protein iLOV for improved photostability. *J. Biol. Chem*. 287, 22295–22304 (2012).

26. Drepper, T. et al. Reporter proteins for in vivo fluorescence without oxygen. *Nat. Biotechnol.* 25, 443–445 (2007).

27. Lam, A. J. et al. Improving FRET dynamic range with bright green and red fluorescent proteins. *Nat Methods* 9, 1005–1012 (2012).

28. Takagi, T. & Doolittle, R. F. Amino acid sequence studies on factor XIII and the peptide released during its activation by thrombin. *Biochemistry* 13, 750–6 (1974).

29. Grashoff, C. et al. Measuring mechanical tension across vinculin reveals regulation of focal adhesion dynamics. *Nature* 466, 263–6 (2010).

30. Lakowicz, J. *Principles of Fluorescence Spectroscopy*. 353-382. (Springer Science & Business Media, 2013).

31. Rizzo, M. a & Piston, D. W. High-contrast imaging of fluorescent protein FRET by fluorescence polarization microscopy. *Biophys. J*. 88, L14–L16 (2005).

32. Ventre, I. et al. Dimerization of the quorum sensing regulator RhlR: Development of a method using EGFP fluorescence anisotropy. *Mol. Microbiol*. 48, 187–198 (2003).

33. Sullivan, K. F. Fluorescent Proteins. 402-403. (Academic Press, 2007).

34. Liu, T. et al. Quantitatively mapping cellular viscosity with detailed organelle information via a designed PET fluorescent probe. *Sci. Rep*. 4, 5418 (2014).

35. Kozak, M. An analysis of 5'-noncoding sequences from 699 vertebrate messenger RNAs. *Nucleic Acids Res*. 15, 8125–8148 (1987).

36. Nedialkova, D. D. & Leidel, S. A. Optimization of Codon Translation Rates via tRNA Modifications Maintains Proteome Integrity. *Cell* 161, 1606–1618 (2015).

37. Bajar, B. T. et al. Improving brightness and photostability of green and red fluorescent proteins for live cell imaging and FRET reporting. *Sci. Rep*. 6, 20889 (2016).

3.8 Figures

Figure 3.1   A typical Jablonski diagram illustrating the energy conversions involved in fluorescence.

Internal conversion

S_2

S_1

hν   hν

hν

hν

S_0

Absorption

Fluorescence emission
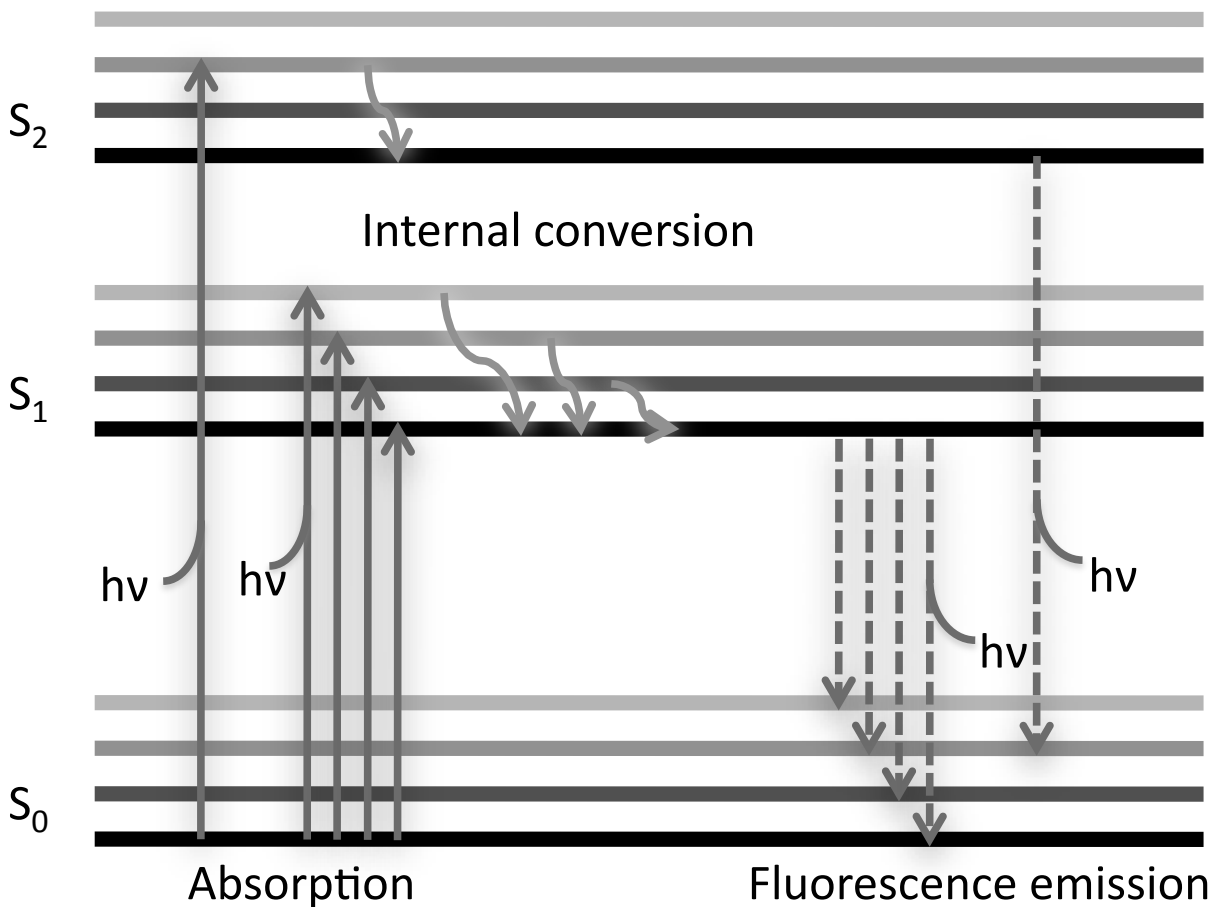
Figure 3.2   A typical FRET efficiency profile displaying the inverse sixth relationship to distance with an R_0 of 5nm. Two example regions on the profile show the dramatic differences seen when the working distance of the FRET pair is near and far from its R_0. Example 1 shows the amount of FRET change measureable when a FRET sensor is designed to work close to R_0. When the distance between donor and acceptor changes from 4nm to 6nm, FRET efficiency sees a large drop from 0.79 to 0.25. However, a similar distance change elsewhere on the profile provides a much less measureable change in FRET efficiency. In Example 2, while the distance change is also 2nm, the FRET efficiency only changed by 0.09 from 0.12 to 0.03. A smaller FRET change is much more susceptible to influence by noise in the data.
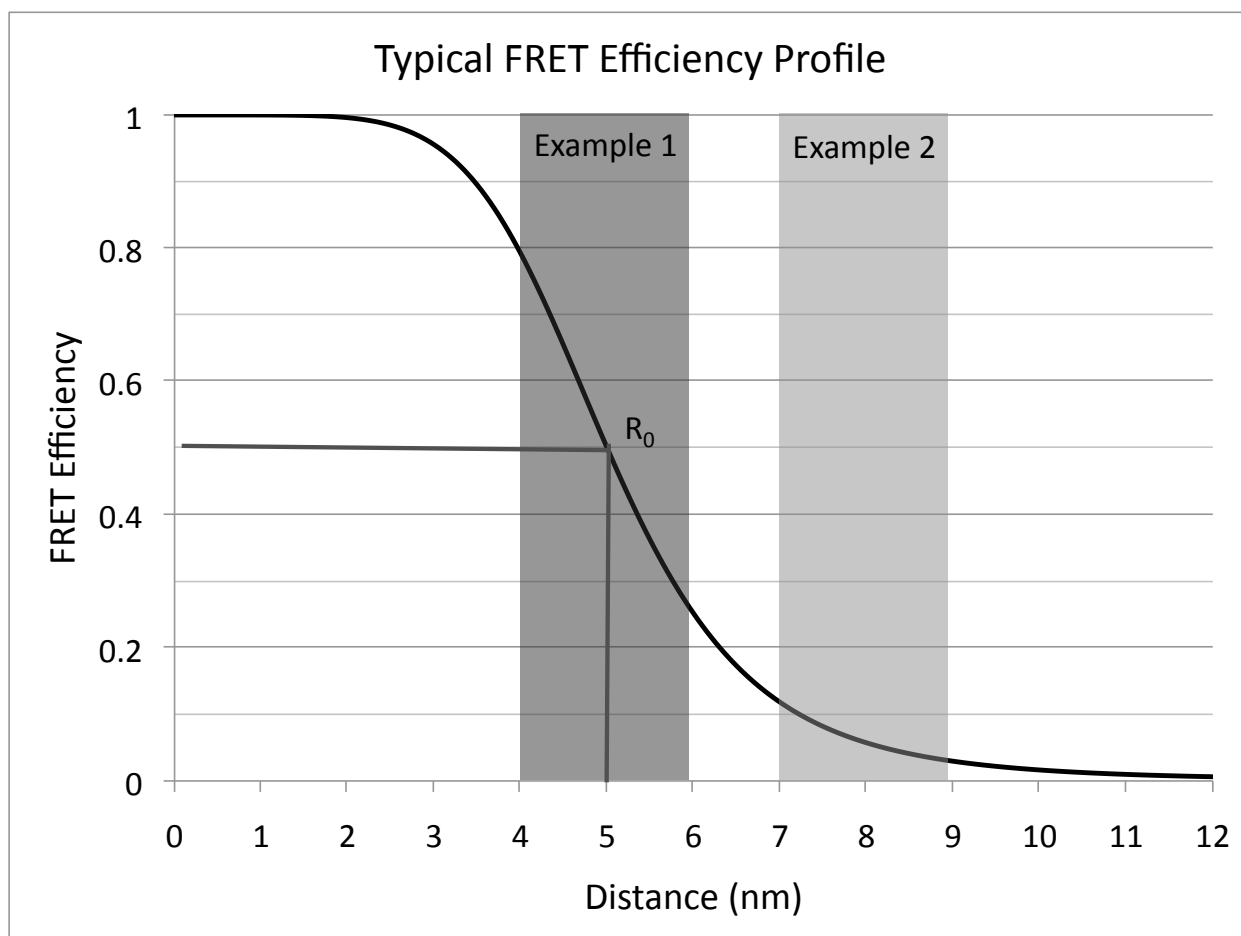
Figure 3.3   The spectral overlap of new FRET pair fLOV2 and mRuby2 (a) is compared to that of previously published FRET pairs Clover and mRuby2 (b)[27], and mTFP1 and Venus (c)[14]. Spectra in (b) and (c) were generated using published data from cited sources. The fLOV2-mRuby2 pairing displays noticeably bigger Stokes shift in both donor and acceptor compared to both published FRET pairs. Compared to Clover as a donor for mRuby2, fLOV2 also has much less absorption overlap with mRuby2, reducing the direct excitation of mRuby2 during FRET measurement and therefore reducing signal noise.
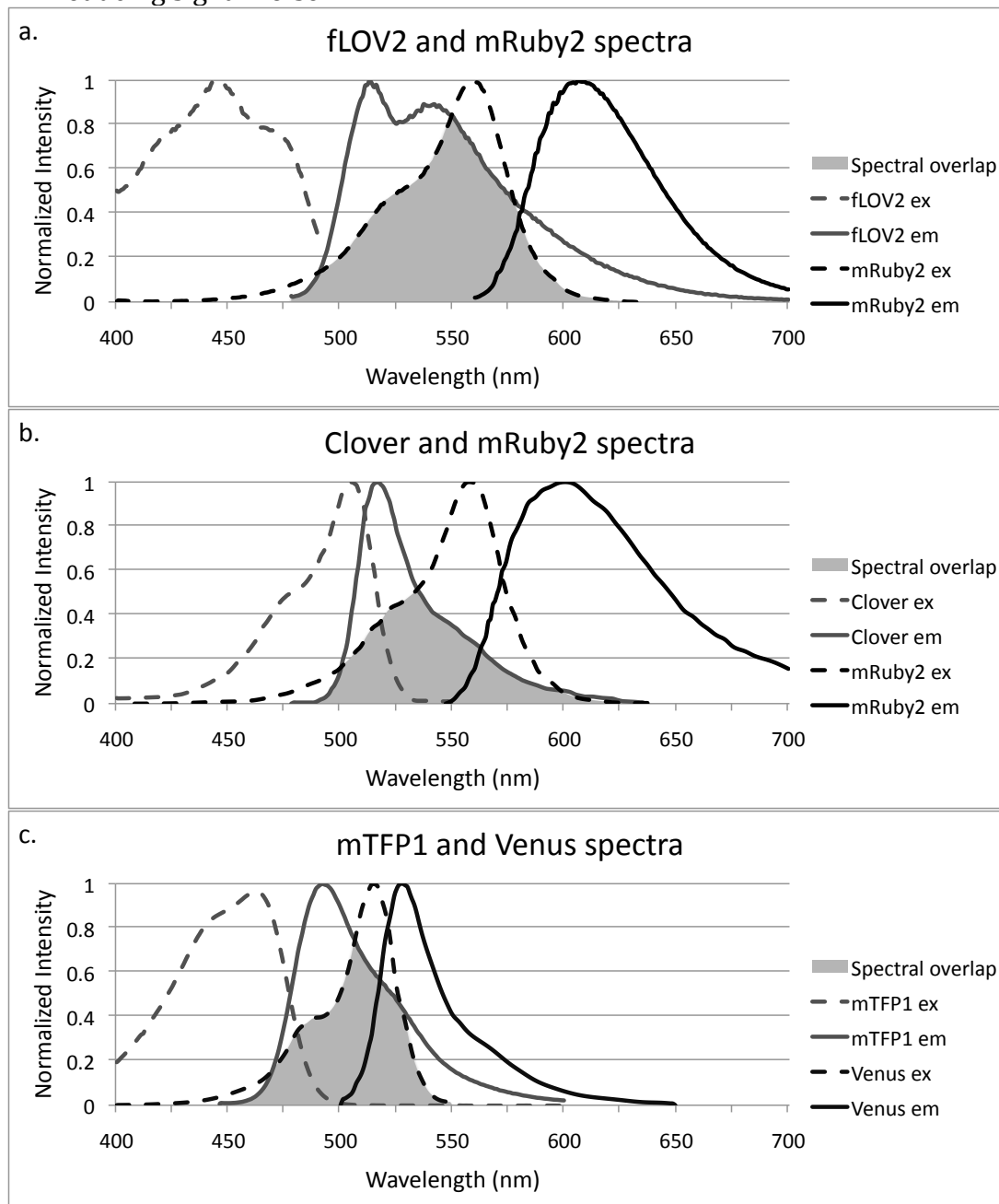
Figure 3.4 Comparing emission channels and filters used in imaging the following 3 FRET pairs: fLOV2/mRuby2 (a), Clover/mRuby2 (b), and mTFP1/Venus (c).
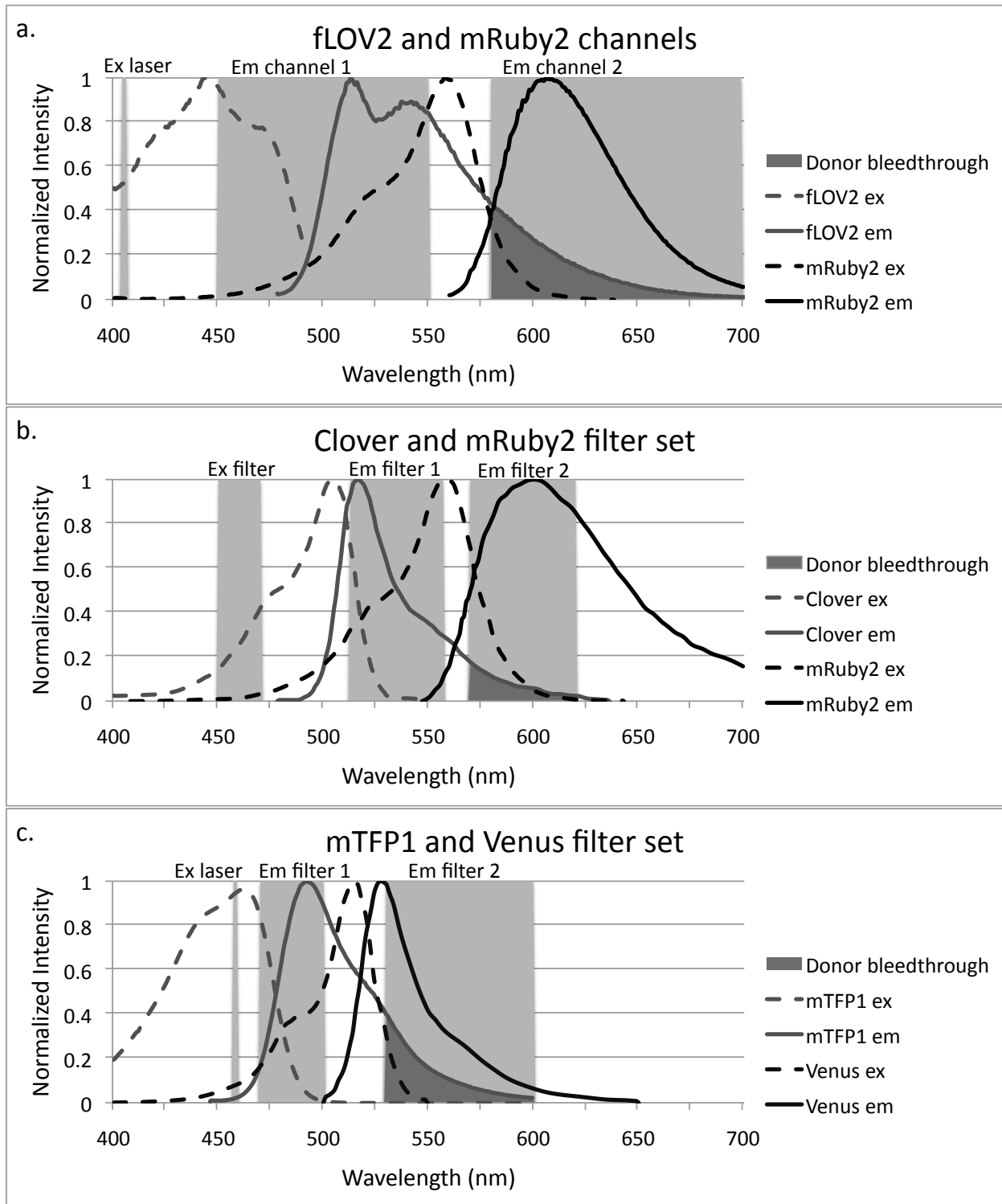
Figure 3.5 Minimal mRuby2-fLOV2 maturation as measured by absorption spectra change over time. Spectra are taken at indicated time points and averaged over 3 samples (a). The time course distinctly shows a gradual emergence of the mRuby2 absorption peak at 559nm for samples matured at all 3 temperatures, which is not present immediately after expression and purification. Visual inspection of all samples confirms appearance of pink hue in solution, which is characteristic of bright red fluorescent proteins such as mRuby2 (b). Unequally matured protein samples also hint at presence of FRET (c). While it is possible, though unlikely to have such a big effect, that the increase in mRuby2 emission in the more matured RT and 37°C samples is due to direction excitation of mRuby2, the simultaneous decrease in fLOV2 fluorescence suggest FRET is taking place.
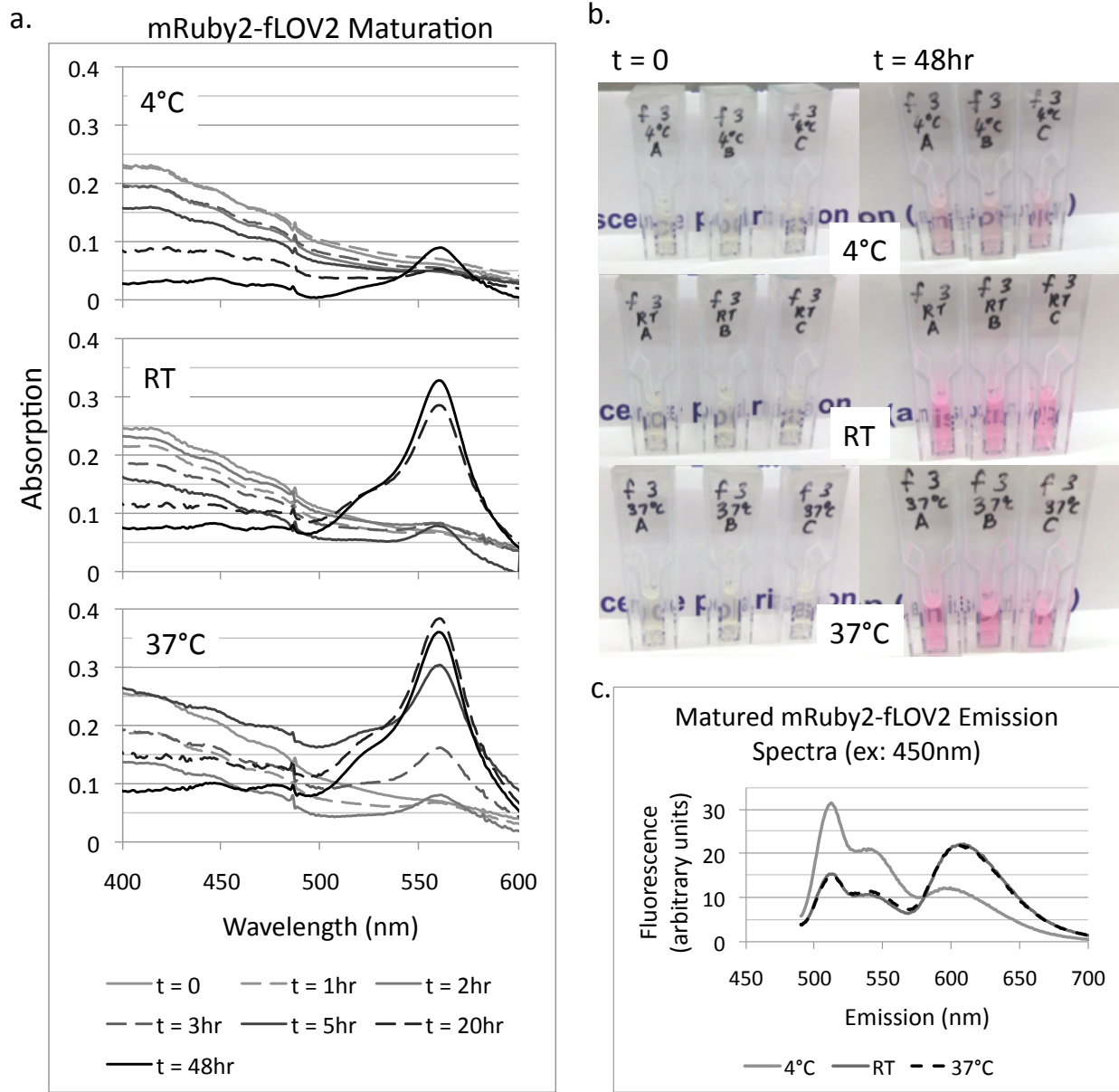
Figure 3.6 Thrombin cleave time course of mRuby2-thr-fLOV2. Proteins in solution were fully cleaved by 40 minutes (a). 445nm was used for excitation wavelength and emission was taken across the spectra of both donor and acceptor. Further measurements past 40 minutes did not change fluorescence profile. Using integrated fluorescence of fLOV2 between 480nm and 540nm, the FRET efficiency of this conjugate protein was calculated to be 43%. Anisotropy of fLOV2 averaged between 500nm and 540nm changed from 0.27 before cleave to 0.18 after cleave. Separated fLOV2 and mRuby2 peaks before and after thrombin cleave shows increase in fLOV2 fluorescence and decrease in mRuby2 fluorescence (b).
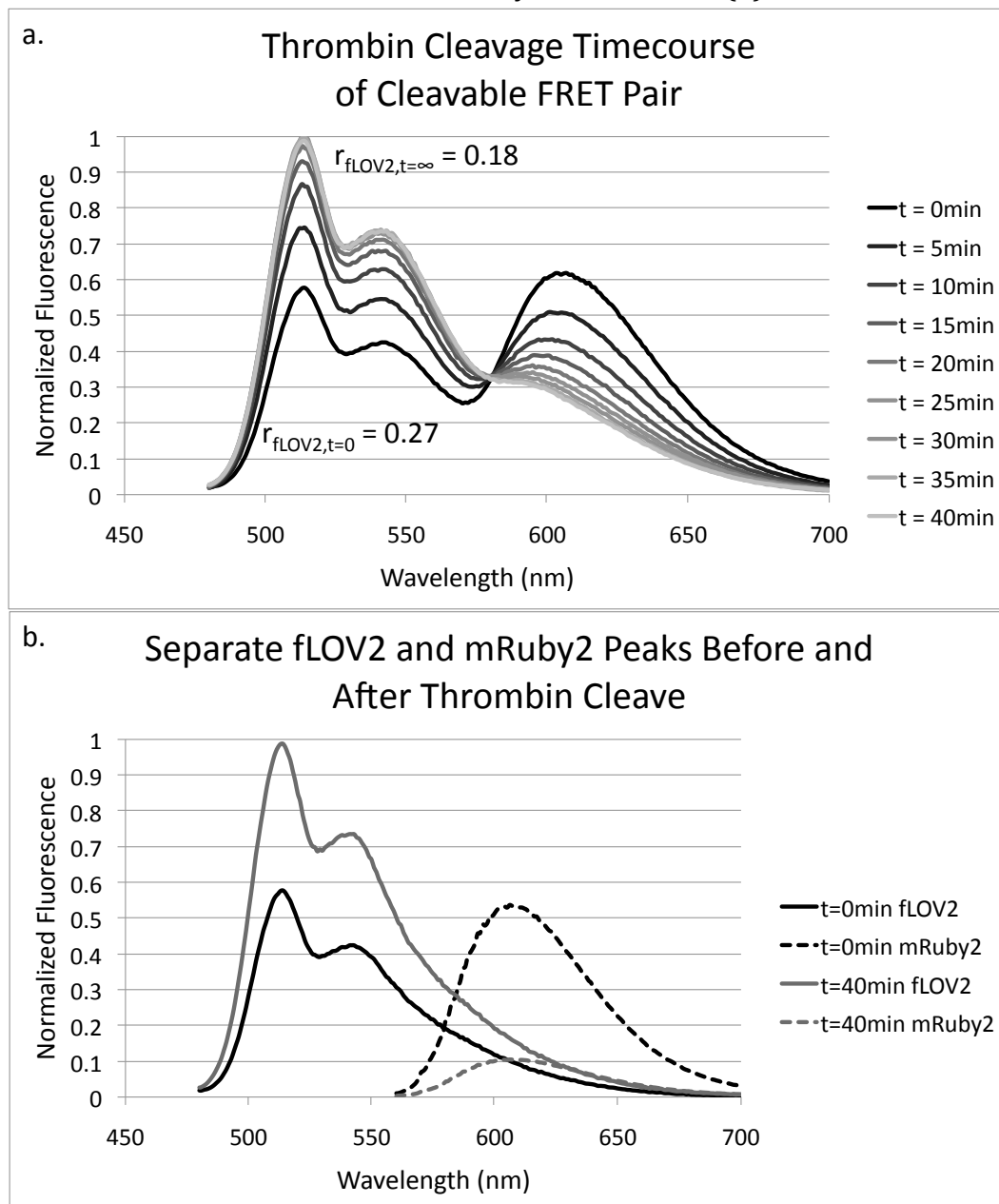
Figure 3.7   Cartoon representations of the three fLOV2/mRuby2 FRET constructs showing their relative spacing differences (a-c) match the measured FRET efficiency in 293T cells (d). The minimal mRuby2-fLOV2 and the mRuby2-coil-fLOV2 constructs were not statistically different in FRET efficiency, although the minimal construct was theorized to have a shorter spacer. Both were statistically higher in FRET efficiency when compared to the mRuby2-thr-fLOV2 construct (p = 0.003 for minimal construct, p = 0.0002 for mRuby2-coil-fLOV2). 6 cells each were measured for minimal mRuby2-fLOV2 and mRuby2-thr-fLOV2. 17 cells were measured for mRuby2-coil-fLOV2.
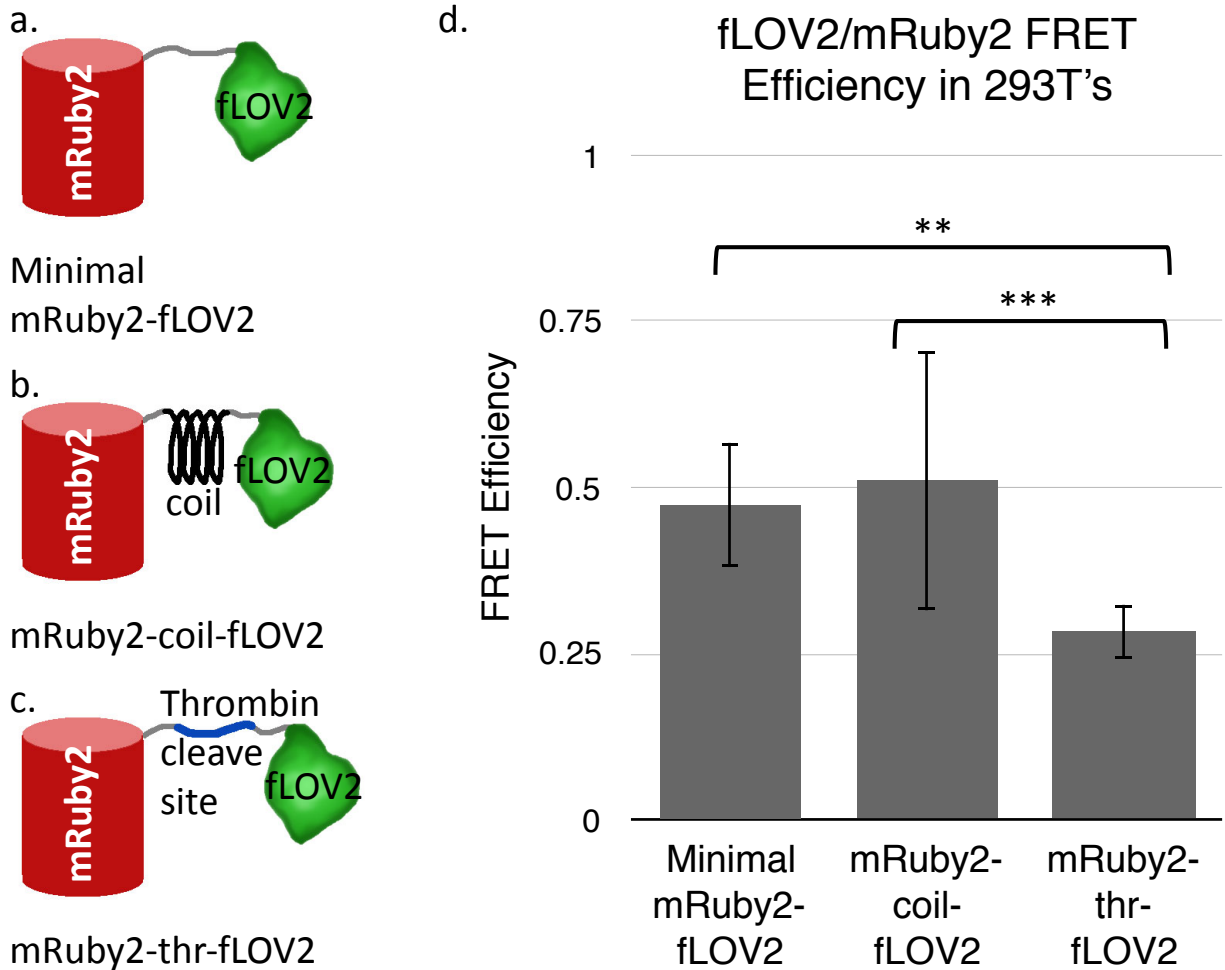
Figure 3.8   fLOV2 fluorescence levels in a characteristic 293T cell before and after mRuby2 acceptor photobleaching shown in each of the three FRET constructs. It is visually discernable that mRuby2-thr-fLOV2 had the least amount of fLOV2 fluorescence increase after mRuby2 bleaching, and therefore exhibited the least amount of FRET.
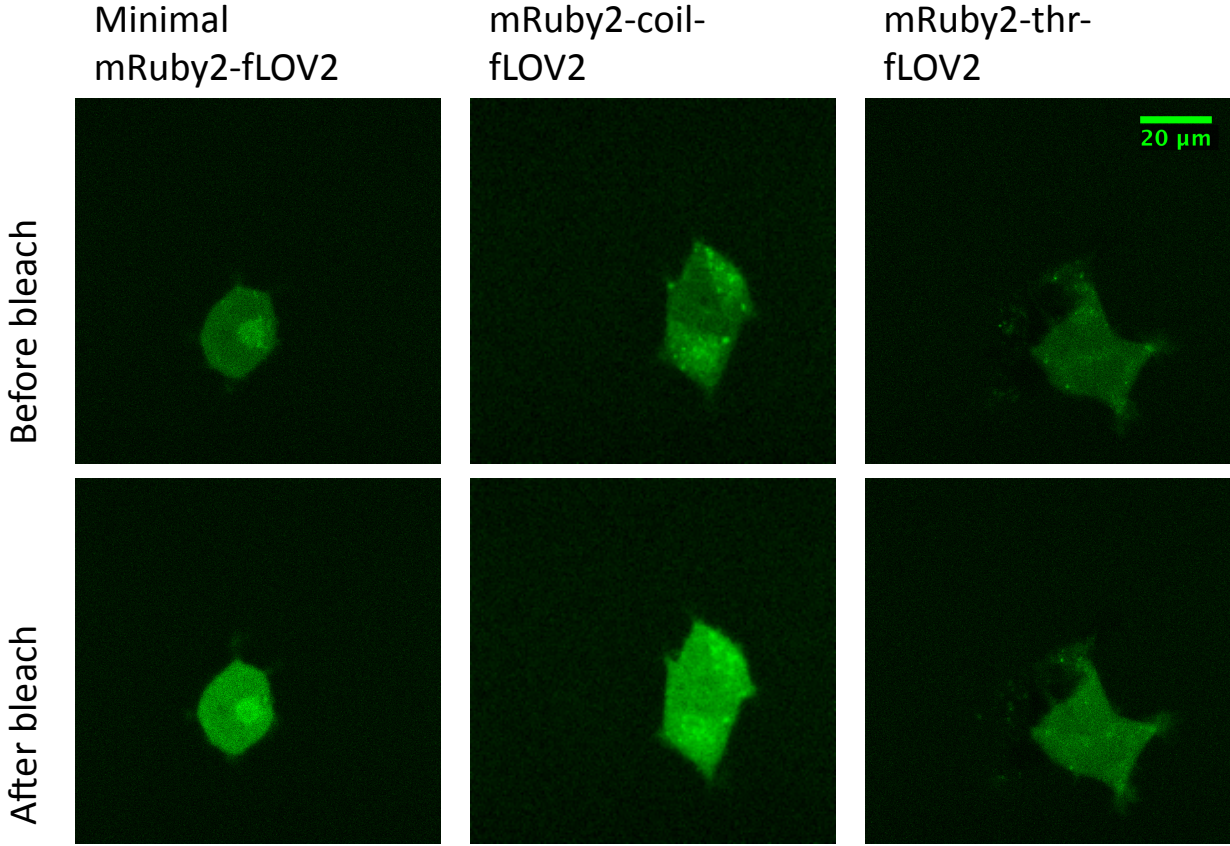
3.9 Tables

Table 3.1 Plasmid constructs used in expressing fLOV2 and mRuby2 proteins and protein conjugates for FRET pair evaluation. PL0100 mRuby2-pBAD was a gift from Michael Davidson (Addgene plasmid # 54771).[27] PL0400 VinculinTS was a gift from Martin Schwartz (Addgene plasmid # 26019).[29]

Code	Name	Source	Vector	Expression
PL0100	mRuby2	AddGene 54771	pBAD	Bacterial
PL0200	fLOV2	Unpublished work by AH	pSKB3	Bacterial
PL0201	mRuby2-fLOV2	PL0100, PL0200	pSKB3	Bacterial
PL0202	mRuby2-thrombin cut site-fLOV2	PL0201	pSKB3	Bacterial
PL0400	Vinculin Tension Sensor (Vin-TS)	AddGene 26019	pcDNA3.1	Mammalian
PL0301	mRuby2-fLOV2	PL0201	pcDNA3.1	Mammalian
PL0302	mRuby2-thrombin cut site-fLOV2	PL0202	pcDNA3.1	Mammalian
PL0303	mRuby2-flagelliform-fLOV2	PL0301, PL0400	pcDNA3.1	Mammalian

Table 3.2 Primers used in generating recombinant protein constructs. F and R indicate direction of binding to template. (P) indicates phosphorylation on the 5' end.

Code	Description	Sequence	Restriction Sites
PR01	mRuby2-F	ATATACCATGGGACACCACCATCATCATCATGGTATGGCAAGC	NcoI
PR02	mRuby2-R	ATATAGCTAGCTGAACCGGATCCCTTGTACAGCTCGTCCATCC	BamHI, NheI
PR03	Thrombin-F	(P)-CGTGGTTCAGCTAGCGAGAAGAAC	--
PR04	Thrombin-R	(P)-CGGAACCAGGGATCCCTTGTACAGCTCGTC	--
PR05	mRuby2-mutate-F	(P)-AGCATGACTGGTGGACAG	--
PR06	mRuby2-mutate-R	(P)-TGCCATACCATGATGATGATGATG	--
PR07	mRuby2-F	ATATAGGTACCATGGTGTCTAAGGGCGA	KpnI
PR08	fLOV2-R	ATATACTCGAGTCAATCCAACTGAACCCC	XhoI

Table 3.3 Buffers used in protein purification and characterization, and the formula of each.

Base buffer (pH 7.9)	Homogenizer prep buffer
o 300mM NaCl o 20mM HEPES	o Base buffer o 10mM imidazole o 1mM PMSF
Lysis buffer	**NiNTA eluting buffer (pH 7.9)**
o Base buffer o 10mM imidazole o 1 crushed pellet of SIGMAFAST Protease Inhibitor per 30mL o Lysozyme o 1mM PMSF	o 300mM NaCl o 20mM HEPES o 250mM imidazole
NiNTA prep buffer	**Final exchange buffer (pH 7.9)**
o Base buffer o 10mM imidazole	o 150mM NaCl o 20mM HEPES
NiNTA prep buffer	
o Base buffer o 25mM imidazole	

CHAPTER 4

Design of a Nesprin Tension Sensor for Nuclear Tension Analysis

4.1 Intracellular Sensors of Mechanotransduction

Mechanotransduction has long been known as a contributing factor in regulating cellular behavior. Aside from the myriad of biochemical signals present in the native environment of a cell, its physical context also provide cues to direct processes such as differentiation, migration, and gene expression. In the context of tissues in the body, cells respond to external mechanical signals by passing this information inwardly to effect change in its internal mechanisms. The process of this information transfer has been a topic of study for the past few decades. Both protein interactions in signaling pathways and direct physical transference of force have been found to carry this mechanical information as well as lead to downstream changes in gene expression and cell function. Many tools and methods have been developed to study these processes, much of which involve the use of FRET.

4.1.1 FRET Sensors

A recent development in the application of FRET in intracellular signal imaging is the creation and calibration of tension sensor capable of measuring force on the piconewton scale.[1] The previously mentioned vinculin tension sensor with a spider-silk peptide spring between a FRET pair is only one of quite a few types of tension sensors that have been developed of late.[2] Meng et al. published in 2008 a FRET tension sensor using a peptide alpha helix as the spring element between the FRET donor and acceptor.[3] Several years later, the same group developed another tension sensor using a spectrin repeat, which consists of 3 alpha helices folded tightly into one another.[4] When force is applied, the helices are not the stretchy element. Rather, the 3 helices separate against their most optimal conformation, providing a nonlinear transmission of force across the FRET sensor to create a more compliant tension sensor. Another tension sensor takes advantage of the naturally flexible shape of talin, a focal adhesion protein, to measure force across a FRET pair.[5]

Tension-based FRET sensors for cell imaging have elevated force transmission studies within the cell to a more quantitative level. The next step is to discover new pathways and proteins to study using these tension sensors.

4.2 Reaching into the Nucleus

In the broader field of cell biology, mechanotransduction itself is a fairly new concept. Within the field of mechanotransduction, nuclear mechanotransduction is only in its infancy. Despite the importance of mechanical cues in gene expression, it is not well understood whether physical transference of force plays a role in this process alongside signaling pathways.

It has become clear, through the past couple of decades of study, that the cell contains distinctly mechanical elements manifested in its networks of microtubules, actin filaments, and

intermediate filaments. Only recently have we discovered that within the nucleus lies its own network of lamin fibers. Studies of genetic diseases such as Emery-Dreifuss muscular dystrophy and Hutchinson-Gilford progeria syndrom laid out the importance of the nucleoskeleton in direction cell function, but how do the external forces of the cell's environment affect the nucleoskeleton?[6] The coexistence of these network structures has lead to speculation that they communicate directly through mechanical forces.[7]

Studies in the past decade have revealed the structures that connect the networks within and without the nucleus. The linker of nucleoskeleton and cytoskeleton (LINC) is a complex of proteins that extend through either side of the nuclear membrane and bind to lamin on the inside, and to various cytoskeletal elements on the outside.[8-10] On the cytoplasm side of the LINC complex is a vast family of proteins called nesprins. Nesprins, in their many differently expressed and spliced forms, bind to cytoskeletal proteins such as F-actin, kinesin, and plectin. Nesprin's long chain-like form can reach several hundred nanometers into the cytoplasm to interact with these cytoskeleton elements.[11] On the other end, nesprins are anchored to the outer layer of the nuclear envelope via a transmembrane domain near its C terminus. The very end of the protein, however, reaches into the intermembrane space to bind with SUN proteins, which in turn reach across the inner layer of the nuclear envelope to connect with lamin A. This interlinked structure is the key to understanding the transmission of physical forces between the cytoplasm and the nucleoplasm.

4.2.1 Nesprin as a Tension Sensor

A detailed study of the proteins in the LINC complex isolated nesprin as the ideal candidate for a tension sensor. Its modular structure with repeats of spectrin motifs form a large straight chain between the cytoskelton and the nuclear membrane, with its LINC complex connections reaching directly across the barrier to the lamin matrix. Prior research on nesprin 2G led to the development of a truncated "mini" version consisting of only the head and tail domains of this enormous protein.[12] This mini-N2G retain a lot of the functionality of the full N2G protein. It was able to localize to the nuclear membrane and bind to SUN proteins in the intermembrane space, as well as bind to actin filaments in the cytoplasm. This connection between the cytoskeleton and the LINC complex, combined with its modular structure, provided a perfect space to insert a FRET sensor.

As previously mentioned, Grashoff et al. recently developed and published a tension sensor utilizing FRET to detect a change in distance between two parts of a protein caused by tension on the protein.[2] This sensor was developed for vinculin to study mechanical forces in focal adhesions. However, the spring-like structure of the FRET construct can be applied to any protein sensor that may be stretched and pulled on due to tension applied across its length. The convergence of these two studies led to the idea of combining both to form a nesprin 2G FRET tension sensor with the tension sensing element of the vinculin tension sensor placed between the head and tail domains of mini-N2G. As the two domains are far apart in the original protein to begin with, the separation caused by the insertion of a FRET sensor is unlikely to cause change in their functionalities.

It must be stated, at this point, that at the time of writing this dissertation, the idea of the mini-N2G FRET sensor had been explored and published by another group.[13] Seeing as the idea was independently conceived, although Arsenovic et al. may have concluded their studies earlier, we still sought to finish the development of our FRET sensor and characterize it as well as incorporate the newly developed fLOV2/mRuby2 FRET pair in this aspect.

4.3 Materials and Methods

4.3.1 DNA Constructs

The molecular cloning and construct design processes used were previously described in detail in section 3.4.1. The following section will only discuss the specific constructs used in this chapter. Plasmids containing constructs referred to in this chapter and primers used in generating these constructs are listed in Table 4.1 and Table 4.2, respectively. All plasmids were made in pcDNA3.1 as a vector and expressed in mammalian cells, excepted those previously described in Chapter 3 and PL0700 which used pEGFP-C1 as a mammalian expression vector.

PL0700 GFP-mini-N2G was a gift from Gregg G. Gundersen.[12] Mini-N2G without the leading GFP (PL0701) was generated as an intermediate construct. It was cloned from PL0700 using the primers PR40 and PR41, and inserted into pcDNA3.1 using restriction sites HindIII and XbaI.

Mini-N2G with mRuby2-coil-fLOV2 between its head and tail domains (PL0702) will be referred to as mini-N2G-RL. Mini-N2G with mTFP1-coil-Venus between its head and tail domains (PL0703) will be referred to as mini-N2G-TV. Both tension sensor DNA constructs were generated by first cloning the whole length of PL0701 and inserting restriction sites for KpnI and XhoI between the head and tail domains using phosphorylated primers PR47 and PR48. The PCR product was ligated back together and referred to as PL0701b. PL0702 was generated by cloning the FRET construct from PL0303 using primers PR07 and PR44. The PCR product was then inserted into PL0701b using KpnI and XhoI to create PL0702. PL0703 was generated by cloning the FRET construct from PL0400 using primers PR45 and PR46. The PCR product was then inserted into PL0701b using KpnI and XhoI to create PL0703. PL0400 VinculinTS was a gift from Martin Schwartz (Addgene plasmid # 26019).[2]

The headless mini-N2G-RL construct (PL0704) was generated by cutting out the segment of PL0702 from the beginning of mRuby2 to the end of the N2G tail domain using the restriction enzymes KpnI and XbaI, then ligating it back into pcDNA3.1.

The headless mini-N2G-VT construct (PL0705) was generated by cutting out the segment of PL0703 from the beginning of mTFP1 to the end of the N2G tail domain using the restriction enzymes KpnI and XbaI, then ligating it back into pcDNA3.1.

The four single fluorescent protein constructs of fLOV2 (PL0801), mRuby2 (PL0802), mTFP1 (PL0803), and Venus (PL0804) were generated from previous plasmids. fLOV2 was cloned from PL0301 using primers PR08 and PR24 and inserted into pcDNA3.1 using KpnI and XhoI to generate PL0801. mRuby2 was cloned from PL0301 using primers PR07 and PR23 and inserted into pcDNA3.1 using KpnI and XhoI to generate PL0802. Due to the similarities in DNA

sequence of mTFP1 and Venus, multiple steps were taken to clone both. PL0400 was first cleaved using ApaI. There being 2 restriction sites of ApaI, PL0400 was separated into two strands, one 1400 base pair strand containing Venus, and one 8800 base pair strand containing mTFP1. The two strands were separated by gel electrophoresis and purified to be used as the template for PCR. Both were cloned using primers PR52 and PR53 and were inserted into pcDNA3.1 using KpnI and XhoI to generate PL0803 and PL0804.

fLOV2 was codon optimized for mammals, specifically rats, using Integrated DNA Technologies (IDT), and the DNA sequence (I_0801op) was synthesized by IDT. The full and headless mini-N2G-RL constructs with codon optimized fLOV2 (PL1702 & PL1704) were synthesized via intermediate constructs due to useful restriction sites present in the N2G regions. I_0801op was cloned with primers PR55 and PR58 to add NheI and XhoI restriction sites before and after the gene and inserted into PL0303 to create PL1303a. This construct has no stop codon and was therefore only used as an intermediate. The full mRuby2-coil-fLOV2(op) sequence was then cut out of PL1303a using KpnI and XhoI and ligated into PL0702 to create PL1702. The same segment of DNA was ligated into PL0704 to create PL1704.

The Kozak consensus sequence was added to the start codon regions of PL0703 and PL1702 to create PL0703K and PL1702K. PL0705 and PL1704 already contained a fair amount of the Kozak sequence and were not exhibiting expression issues and therefore were not treated to this edit. The N2G head region was cloned from PL0702 using primers PR48 and PR59, with PR59 containing the Kozak sequence. The PCR product was then ligated into PL0703 and PL1702 to replace the original N2G head segment.

4.3.2 Cell Culture

The cell culture protocols were same as previously described in section 3.4.5 except for those detailed below.

NBT-II rat bladder tumor cells were obtained from American Type and Culture Collection (ATCC). NBT-II cells were maintained in growth medium and passaged every 2 to 3 days when 75% confluenced was reached at a ratio of 1:20.

Plasmids were transfected as previously described. Briefly, NBT-II's were seeded at 25,000 cells per well in a 24-well plate 24 hours prior to transfection. Transfection was conducted in penicillin/streptomycin-free transfection medium with 1.5μL Lipofectamine2000 and 500ng DNA plasmid per well. The transfection medium was replaced with fresh growth medium after 6 hours. Cells were passaged 18-24 hours after transfection onto 35mm glass bottom dishes coated with 10μg/mL of fibronectin from human plasma (Sigma-Aldrich). Fibronectin was coated onto the glass bottoms of the dishes by incubation at room temperature for 30 minutes. The dishes were quickly rinsed with 1x PBS before cell seeding. Cells were imaged after a further 24 hours of growth.

The expression of transfected proteins were observed on a Zeiss LSM 700 laser scanning confocal microscope prior to obtaining FRET data. Both a 20x air objective and a 63x oil objective were used for these observations.

4.3.3 FRET Imaging

Prior to imaging, cells were changed to HEPES-buffered phenyl-red-free growth medium to reduce autofluorescence in FRET measurements. Expression and cell health were checked on the Zeiss LSM 700 using methods detailed in Chapter 3. FRET data was taken using a Zeiss LSM 710 AxioObserver equipped with a temperature and carbon dioxide controlled incubation chamber with heated stage for live cell imaging (courtesy of Molecular Imaging Center at the UC Berkeley Cancer Research Laboratory).

Spectral imaging and linear unmixing
FRET images were taken and analyzed using protocols based on previously published methods.[13,14] The spectral imaging technique was used to collect all FRET data on the Zen 2010 software. The incubation chamber was warmed up for 30 minutes prior to imaging. A 63x oil objective was used for all experiments. Images were acquired using a 34-channel spectral detector, collecting fluorescence for 7 bins evenly spread across the range of 453nm to 725nm. The number of bins was chosen based on fluorescence intensity and noise levels in the measurement. Images were acquired in 16 bit and averaged over 4 takes to reduce background noise.

For cells expressing the fLOV2/mRuby2 FRET pair or either of the fluorescent proteins alone, the 458nm and 561nm lasers were used at 80% and 5% power, respectively. A combination 458nm/561nm dichroic filter was used to filter out both laser lines. The individual spectra of fLOV2 and mRuby2 alone were first taken as references for linear unmixing of images taken of cells expressing both fluorescent proteins. The same was done for the mTFP1/Venus FRET pair, using the 458nm and 514nm lasers at 80% and 5% power, respectively, and a combination 458nm/514nm dichroic filter. After acquisition, each image was linearly unmixed on the Zen 2010 software using the previously recorded spectra of the donor and acceptor. Background fluorescence was negligible and the inclusion of background channels did not significantly affect the data; therefore background channels were not included in the linear unmixing process

4.4.4 ASBT Calculations

For the analysis of each FRET pair, control sets of images were taken using cells expressing the acceptor only for calculations of Acceptor Spectral Bleedthrough (ASBT).[14] For all acquisition, the donor excitation image (DE) was first taken, and then the acceptor excitation image (AE) of the same region was taken immediately after. Each image required 15.5 seconds for acquisition, and laser lines were switched manually in between. At least 20 cells were imaged for each sample set.

In order to remove acceptor bleedthrough caused by direct excitation, a ratiometric value of ASBT was first calculated using acceptor-only samples. Table 4.3 outlines the group of images involved in ASBT analysis and their origins. In the following text, these images will be referred to by their names used in Table 4.3. For this analysis to apply, control images must be taken using the same microscope settings as the data. The following analysis was done using a

MATLAB program written by the author of this thesis. Figure 4.3 shows select intermediates in the ASBT calculation and FRET analysis steps.

Determining bleedthrough using acceptor-only control
After linear unmixing, pixels saturated in the Acc_AE-ch2 image are set to 0 in both Acc_AE-ch2 and Acc_DE-ch2 to remove artifacts in calculation. Each Acc_DE-ch2 and Acc_AE-ch2 image is then background subtracted using the average intensity of a fluorescence-free region comprising 1% of the total image area. Pixels with negative intensity after background subtraction are set to an intensity of 0. This ratio is a platform-dependent measure of the amount of direct excitation of the acceptor fluorophore using the excitation wavelength of the donor. A ratio of Acc_DE-ch2/Acc_AE-ch2 is calculated on a per-pixel basis for each pair of unmixed images. The ratios of all the individual pixels across all imaged cells are then aggregated and binned into intensity ranges based on the intensity value of the pixel in the Acc_AE-ch2 image. An average ratio ra(j) for each intensity bin j is calculated according to the following equation where there are m pixels in each intensity range.[14]

$$ra(j) = \frac{\displaystyle\sum_{i=1}^{i=m} \frac{Acc\_DE-ch2_i}{Acc\_AE-ch2_i}}{m}$$

Eqn 1.

The table of ra(j) is output from the program for future use. Since the data was taken separately from the ASBT control, the ASBT corrections were done on an intensity range basis.

FRET calculations
The nesprin FRET sensors were localized to the nuclear membrane, and steps were taken to analyze only the nuclear membrane. After linear unmixing of each set of data, a binary mask was calculated for each cell to include only the nuclear membrane, in the opensource software ImageJ using a pre-written script. Masks were calculated based on intensity and continuity of fluorescent regions and occasionally included bright speckles in the cytoplasm. When necessary, the masks were manually cleaned up to remove unwanted pixels in the cytoplasm. For analysis of TAN lines versus smooth nuclear membrane, masked regions of TAN lines were manually identified and separated. If an image contained multiple cells, a separate mask was created for each cell and each cell was analyzed as a separate data point. The following analysis was done using a second MATLAB program written by the author of this thesis.

Similar to that done for the acceptor-only controls, images first had saturated pixels removed and were background subtracted. Pixels in which either fluorophore was missing were removed from all images. The ImageJ masks were then applied to each cell. The matrix of each image was then flattened and all non-nuclear membrane pixels were removed. The following analysis was done for each cell. Using the FRET_AE-ch2 image, all pixels in the cell were binned into the intensity ranges designated by the ra(j) output file. The ASBT was then calculated for each pixel in the cell by multiplying FRET_AE-ch2 pixels by the appropriate ra(j) value depending on the intensity bin of the pixel. The final corrected acceptor channel pixel values were calculated by subtracting the ASBT from FRET_DE-ch2 on a pixel by pixel basis to generated FRET_DE-ch2$_{ASBT}$. Finally, the ASBT-corrected FRET ratio is calculated by FRET_DE-ch2$_{ASBT}$/FRET_DE-ch1 for each pixel. Pixels with ASBT-corrected FRET ratios over 20 were considered outliers and removed from further analysis.[13]

For each cell, the cell-average ASBT-corrected FRET ratio was computed. Each pixel was then once again intensity binned by the intensity of the FRET_DE-ch1 image and aggregated into a group-wide analysis. Bins in which there were fewer than 3 pixels were removed from analysis. The output of this program, therefore, provided the average ASBT-corrected FRET for each individual cell and the average ASBT-corrected FRET for each intensity range using pixels aggregated across 30+ cells. Both cell-based and range-based analysis were considered. The range-based analysis considered all the cells as a population, while the cell-based analysis takes in account the individual variability of cells within a population.

Statistical analysis of FRET data was conducted using GraphPad Prism. Analysis of data containing 2 variables were conducted using 2 way ANOVA with Sidak's multiple comparisons test. Analysis of pairs of data were conducted using the student t-test.

4.4 Results and Discussion

4.4.1 Nesprin Tension Sensor Expression in 3T3 and NBT-II Cells

The full constructs mini-N2G-RL and mini-N2G-VT were the first nesprin tension sensors synthesized and expressed *in vitro*. Initial attempts to express these proteins gave very little fluorescence levels. When compared to the original GFP-mini-N2G constructs, the tension sensors showed little to no nuclear membrane localization when expressed in both NIH 3T3's and NBT-II's (Figure 4.4 and Figure 4.5). Imaging using the acceptor fluorophore to avoid autofluorescence of the cells showed that the majority of fluorescence in the donor channel was autofluorescence. However, the headless controls for both RL and VT versions of the tension sensors appeared to express much better and showed fairly clear nuclear localization (Figure 4.4 and Figure 4.5).

Due to the lack of nuclear membrane localization, various attempts were made to improve the tension sensors. First, an attempt was made to increase the distance between the FRET construct and the nuclear membrane in case the bulk of the FRET pair contributed to the inability of the recombinant protein to localize to the nuclear membrane. This was done by cloning the second half of N2G head region, including everything after the CH domains, and inserting it between the FRET construct and N2G tail region. The entire protein is therefore lengthened by this segment of 191 amino acids. This attempt did not improve expression and increased the bulk of the tension sensor. It was not used for future experiments.

At the same time as these attempts to improve in vitro expression of the nesprin tension sensor constructs, Arsenovic et al. published a very similar nesprin tension sensor to the mini-N2G-VT construct using the same source papers as inspiration.[13] While the initial constructs were conceived independently of this paper, the continuing experiments attempt to replicate some of their published results.

Codon optimization of fLOV2
While both mini-N2G-FRET constructs showed low expression, the mini-N2G-RL protein appeared to have even lower levels of expression as compared to the mini-N2G-TV protein when tested in multiple cell types. One factor considered was the codon optimization of fLOV2. All

other portions of both constructs were previously published in mammalians cells *in vitro* without issue. While each amino acid may correspond with multiple synonymous codons in the translational process, with the exception of methionine and tryptophan, not all codons of the same amino acid are made equal. For any given amino acid, the frequencies of occurrence for its codons are species-dependent. Those species that are evolutionarily closer to each other tend to have similar codon usage profiles, whereas organisms far apart on the phylogenetic tree tend to greatly differ in this aspect.[15,16]

fLOV2, derived from a plant protein, is naturally optimized for plant expression and not mammalian expression as is required for the experiments in this chapter. It has been shown that optimizing codons to the expressing species can improve the expression level of introduced recombinant proteins.[17] Furthermore, there is evidence to show that the use of rare codons can impede in not only expression levels, but protein function as well. This may be due to the decreased translation rate near the rare codons, leading to abnormalities in the secondary and tertiary structures of the final product. While protein structure is highly dependent on the primary sequence, the process of protein folding takes place along side translation and not after. Therefore, the rate at which the peptide sequence exits the ribosome can have significant impact on the protein taking shape even as it is being translated.[18]

When compared to commercially available (Integrated DNA Technologies) charts of codon frequency, the original fLOV2 DNA sequence contained multiple extremely rare codons (<10% occurrence for a specific amino acid) in mammals. Specifically, 5 codons were extremely rare in mice (3T3) and 2 codons were extremely rare in rats (NBT-II). Although it is unclear the exact algorithm and reasoning IDT used for selecting which codons should be used, it was verified that in the optimized sequence, no extremely rare codons for mice or rats were present. The codon optimization by IDT appears to have only minor positive impact on the expression level of fLOV2-containing recombinant proteins (Figure 4.6). This may be due to the complex nature of codon frequency.

For proteins with complex secondary and tertiary structures, translational speed is often built into the DNA sequence of the gene. While rare codons slow down translation, this is not necessarily a negative effect. It may be required, in certain circumstances, to modulate translation rate for the correct folding of specific regions. Studies replacing rare codons with frequent ones have shown that this can have a negative impact on protein function as well.[19] These complexities make codon optimizing difficult and it is not clear at the present time what the best course of action for optimizing expression is. One proposed method is to match codon frequency between the native organism and the intended expression host for maximum folding compatibility. Although theoretically sensible, this method may not necessarily provide the best sequence given that evolutionarily distant organisms will also have very different chaperone proteins. Whether or not this is a concern for fLOV2 is uncertain. Optimization of fLOV2 was completed using IDT algorithms, and it is unclear their specific method. A future improvement of fLOV2 DNA sequence may take advantage of published *Avena sativa* codon usage tables for manual frequency-matched optimization. Other options include screening through a library of random silent mutations. Nevertheless, the "optimized" sequence was retained and used for further experiments.

Kozak sequence

Comparing the full constructs to the headless control constructs, it was found, interestingly, that the headless constructs showed better nuclear membrane localization (Figure 4.4 and Figure 4.5). Upon further inspection of the DNA sequences, it was concluded that the full constructs lacked a Kozak consensus sequence around the start codon, which, in many cases, improve the expression level of proteins.[20,21] As an artifact of the molecular cloning process, the headless constructs already contained the most essential components of the Kozak sequence, and this presence may have explained the differences in expression and localization when both groups of constructs contained identical membrane localization regions. While the full constructs also contain a large nesprin head domain not present in the headless constructs, it was sufficiently far away from the transmembrane domain that it should not have interfered in its function.

The optimal Kozak sequence for vertebrates was determined to be GCCACCatgG, with the G immediately following the start codon and the A in the -3 position playing the most important roles and some variability from species to species in the other positions.[20,21] The G in the -6 position and the C's in the -1 and -4 positions all occur with very high frequency as well. The two headless constructs contained the following sequence around the start codon: GGTACCatgG. While it was not the fully optimal Kozak sequence, it contained the most important elements and was evidently enough to ensure adequate expression. The full constructs, however, contained the following sequence around the start codon: AAGCTTatgG. It was missing most of the Kozak consensus sequence and this discrepancy most likely lead to the poor expression in all cell types tested. Both full constructs mini-N2G-RL and mini-N2G-TV were edited to include the exact sequence of GCCACCatgG around the start codon. This change dramatically improved expression and localization.

Whereas previous versions of mini-N2G-FRET constructs showed poor expression and localization in both cell types, especially 3T3's, the Kozak sequence improved versions (mini-N2G-RL-K and mini-N2G-TV-K) showed very clear localization to the nuclear membrane in both 3T3's and NBT-II's (Figure 4.7). The localized proteins are bright and clearly distinguishable against background noise in the acceptor channel. Their expression levels and localization appeared to be on par with the headless constructs.

While the above methods improved nuclear membrane localization of expressed proteins, background fluorescence was still a problem for imaging of both fLOV2 and mTFP1 donor proteins. In all of the images, the donor channel was not clear, even for the headless constructs, and did not show discernable nuclear membrane localization (Figures 4.4-4.7). However, spectral imaging methods and the use of a different set of lasers reduced these artifacts and autofluorescence was not a significant issue in the FRET data for the mTFP1/Venus FRET pair. Imaging the FRET constructs with spectral methods on the Zeiss LSM 710 using 458nm as the donor excitation of both, instead of 405nm for fLOV2 and 488 for mTFP1 on the Zeiss LSM 700 in channel mode, appeared to reduce noise for the mTFP1/Venus FRET pair (Figure 4.8). However, this was not the case for the fLOV2/mRuby2 FRET pair. Both full and headless constructs of the TV version showed nuclear membrane localization in both donor and acceptor channels. The proteins also displayed FRET in both 3T3's and NBT-II's. Due to the difficulties in imaging fLOV2/mRuby2, mTFP1/Venus was used for most of the following experiments. In

the cases where fLOV2/mRuby2 was used, the acceptor channel was used for identifying the nuclear membrane for calculating binary image masks.

4.4.2 FRET Imaging and Analysis

Spectral imaging and linear unmixing
As previously discussed in Chapter 3, spectral separation is of great concern when imaging FRET, especially when FRET is evaluated as a ratio of acceptor to donor emission levels. In the majority of cases, when the donor emission and acceptor excitation overlap sufficiently for efficient FRET to occur, there also exists a significant overlap between the emission spectra of both fluorophores. Imaging methods using band-pass filters that collect within a range of wavelengths for each of the fluorophores are unable to fully separate the contributions of donor and acceptor fluorophores to the longer wavelengths. Using an acceptor with larger Stokes shift can improve separation, but without further analysis, it's not possible to completely remove donor contribution to the acceptor channel. Spectral imaging provides a method of computationally separating the two spectra.

Fluorophores each have their signature emission profile. While it's not possible to distinguish the contribution of multiple fluorophores to one or two channels, when many channels are used, a new distinct summed profile of all present fluorophore emerges. Given enough data points (e.g. channels), this summed profile is able to be separated into its individual component parts when the component spectra are known. The initial publication of this method used as few as 4 channels to separate 5 fluorescent proteins successfully.[22] To apply this method, each fluorophore of interest must first be imaged using the same settings across all channels to obtain its specific spectral signature. It is then a relatively simple process of determining the correct multiplier for each component spectrum within the summed spectrum.

With recent improvements in microscopy technology, the application of this method is easier than ever. The Zeiss LSM 710 series is able to use spread light across a 34 channel detector for simultaneous collection of the entire lambda stack. The corresponding software also includes an authomated algorithm for linearly unmixing images taken in lambda mode. The availability of this technology makes it possible to collect a large amount of data using spectral imaging. The use of a large number of channels helps to distinguish more fluorophores when necessary. However, the drawback is that each channel is then collecting much less bright and prone to interference by background noise. The choice of number of channels is therefore a case-specific one based on the measurable intensity of the fluorophores of choice and the number of fluorophores present. Given that these FRET experiments contained only the donor and acceptor in each sample, it was not necessary to use too many channels. Ultimately, 7 channels were used for analysis after trial and error.

ASBT correction
Spectral imaging and linear unmixing is able to remove error from bleedthrough between channels caused by emission spectra overlap. However, without further analysis, acceptor emission due to sensitization from the donor is spectrally indistinguishable from acceptor emission due to direct excitation from the laser. Acceptor Spectral Bleedthrough (ASBT) correction is a method of removing the signal contamination caused by acceptor fluorophores

directly excited by the donor excitation wavelength.[14] By first measuring fluorescence intensities as the result of both donor and acceptor excitation wavelengths in a sample that contains only acceptor fluorophore, we are able to compute the rate of acceptor fluorophores being excited by donor excitation wavelength. In a typical FRET measurement, the sample is excited by the donor excitation wavelength only, and data is taken in both donor and acceptor channels. In order to apply ASBT correction, each FRET measurement must also be coupled with the same exact image excited by the acceptor excitation wavelength. This second image can then be used to estimate the amount of fluorescence in the acceptor channel of the FRET image that was not caused by sensitization from the donor. The contaminating fluorescence can then be subtracted from the acceptor channel to obtain a more accurate measurement of FRET ratio. Some of the intermediate steps of this method is shown in Figure 4.3. This method is used throughout the following FRET analyses.

4.4.3 Comparing Full Construct and Headless Control

The first verification that the tension sensor was functional was to compare between the full constructs and the headless controls. While observation showed us that the N2G tail region is correctly localized to the nuclear membrane, further manipulation was necessary for ascertaining whether the N2G head region was bound to actin fibers as expected in the full construct. It was expected that the full construct would be under tension due to its connections on both side. It would therefore display lower FRET than the headless construct, which has no connections on the N terminus and should have the FRET sensor in its relaxed conformation, giving the shortest distance between donor and acceptor.

mTFP1/Venus FRET constructs
When expressed in 3T3's, headless mini-N2G-TV measured higher in FRET than mini-N2G-TV-K, as expected. This difference is statistically significant when a paired t-test is conducted, with individual intensity bins of both proteins paired together for comparison (Figure 4.9a). This was repeated on 3 separate occasions with the same relative result, albeit with different exact values of FRET ratios, perhaps due to differences in growth conditions on these days of experiments. The first experiment measured at least 23 cells in each sample group, and the latter two experiments each measured at least 40 cells in each sample group.

When expressed in NBT-II's, the same difference was not seen. FRET of both constructs in NBT-II's was measured on 4 separate occasions, and each experiment measured at least 39 cells in each sample group. In 2 experiments, the headless construct exhibited higher FRET as expected. However, in the other 2 experiments, the full construct exhibited higher FRET (Figure 4.9b). Interestingly, the differences seen in all 4 experiments were statistically significant.

One possible explanation of the NBT-II data is that NBT-II's are epithelial cells and are under lower tension than 3T3's. 3T3's migrate outwards after division while NBT-II's continue to grow in a connected monolayer and do not spread horizontally the way 3T3's do. The squamous shape in which these cells grow places them under less horizontal tension than compared to 3T3's. This, however, does not explain why 2 of the experiments showed the full FRET sensors seemingly under compression. The tension sensor construct consisting of the spider silk peptide spring located between the donor and acceptor fluorescent proteins has not been previously

tested for measurement of compression in a force-controlled environment and conjectures about cells or just the nesprin protein undergoing compressive rather than tensive forces cannot currently be verified using this tension sensor. This is, however, an interesting direction to explore for future applications of this tension sensor. Using optical tweezers and a well-characterized small molecule FRET pair, it may be possible to ascertain the ability of the spider silk peptide coil to compress and to match change in FRET to the amount of compressive force applied, similar to the characterization for the tension sensing capabilities of this peptide spring.

The fLOV2/mRuby2 FRET constructs were tested in NBT-II's in 1 experiment, measuring 50 cells in the headless control sample and 41 cells in the full construct sample. The results showed almost identical FRET levels between the headless and full constructs. This would seem to agree with the mTFP1/Venus FRET pair results implying that nesprin in NBT-II cells are under no significant tension.

4.4.4 TAN lines

Transmembrane actin-associated nuclear (TAN) lines are associated regions between actin filaments and the LINC complex and are instrumental in nuclear movement.[12] TAN lines form along the length of actin filaments and connect to lamin on the inside of the nuclear envelope. Nesprin2G, the basis protein of mini-N2G, is known to associate with TAN lines. The function of TAN lines suggests that they are an active formation. Following this line of thought, it was hypothesized that nesprin2G located on TAN lines are under higher tension, due to its active nature, compared to nesprin2G located at smooth regions of the nuclear membrane, which may be under more steady state tension. Previous literature has established the ability of mini-N2G to localize to TAN lines and rescue nuclear movement functions in nesprin2G knockouts.[12] It is therefore expected that the mini-N2G-FRET constructs should retain this functionality and would be able to measure the difference in tension, if any, between nespring2G located at TAN lines versus elsewhere on the nuclear membrane.

Arsenovic et al. showed that their mini-N2G FRET sensor, similar to mini-N2G-TV described in this chapter, localized to TAN lines.[13] Here, we test the hypothesis that nesprin2G located in TAN lines may be under higher tension when compared to nesprin2G located in smooth areas of the nuclear membrane.

For all TAN line data, the TAN lines of each cell was paired with smooth regions of the same cell for comparisons instead of aggregating data across all cells of the same sample. This was done to reduce effects of population variability so that each cell is only compared to itself. 2 way ANOVA was conducted to evaluate the interaction between protein construct (headless vs. full) and protein location (smooth membrane vs. TAN line). Both fLOV2/mRuby2 and mTFP1/Venus FRET sensors were tested in NBT-II cells for these experiments. At least 20 cells were measured for each sample group. No variable interaction was found in either mini-N2G-RL or mini-N2G-TV samples.

The fLOV2/mRuby2 FRET sensor measured lower FRET in TAN lines. The difference is statistically significant. The headless control construct also showed lower FRET in TAN lines, but not statistically significant. The mTFP1/Venus FRET sensor data had a similar trend.

However, the headless control also showed a statistically significant difference between smooth membrane and TAN lines. The headless control should not be affected by tension and this data is an indication of artifacts in the measurement process.

For each cell, the smooth membrane images were taken before the TAN line images. Although the images were taken at difference planes of the cell, this may still have caused some level of photobleaching in both the donor and acceptor proteins prior to TAN line measurement, which would lower the calculated FRET ratio. While confocal microscopy limits the exposure to excitation lasers to the imaging plane, for these experiments the imaging plane was thickened to 3µm in order to offset the dimming effect of spreading collected fluorescence across 7 channels. Photobleaching of donor protein should not affect FRET ratio, especially with the aid of ASBT correction to remove signal contamination from direct excitation of acceptor. However, photobleaching of acceptor protein leaves donors without acceptors and directly lowers the FRET ratio. These two photobleaching effects on FRET ratio do not cancel each other out unless both the donor and acceptor are bleached on the same protein.

Assuming photobleaching is the primary contributor to the lower FRET ratio in the TAN line data of the headless controls, the FRET difference in the tension sensors may still indicate a higher tension on the TAN lines. In both the RL and TV FRET constructs, the headless control showed a 10% lower FRET ratio in the TAN line measurements. If this is caused by photobleaching, and assuming the full constructs bleached similarly, the FRET ratio in TAN lines are still lower than the rest of the nuclear membrane when the 10% drop is adjusted for. There can be no assumption of significance in this case.

The data from this experiment is inconclusive and the experiment must be repeated. The effect of photobleaching may not be easy to remove post-hoc. However, it may be possible to devise an experimental setup to account for its effects. Nevertheless, the preliminary data suggests a higher tension in nesprin2G located at TAN lines and it is worth exploring further with repeated experiments and improved analysis.

Aside from the effect of TAN lines on nesprin2G tension, the two versions of the tension sensor appeared to show no baseline tension at all in the tension sensor. The mini-N2G-RL tension sensor displayed no significant difference in tension in the full construct as compared to the headless control. Although the trend seems to suggest lower FRET in the full construct, indicating tension across nesprin2G as expected. The mini-N2G-TV tension sensor, however, displayed significantly higher FRET in the full construct, which cannot currently be interpreted due to the lack of compression characterization on this construct

4.5 Conclusion

In this chapter, a nesprin2G tension sensor was designed and synthesized to measure the transmission of force from the cytoskeleton to the nucleoskeleton. While the mTFP1/Venus version of the tension sensor was published by Arsenovic et al. as the author of this thesis was developing it, an attempt was made to expand upon its use as well as applying a second FRET pair, fLOV2/mRuby2, to the sensing element of this tension sensor in tandem with mTFP1/Venus.

Comparison of the mTFP1/Venus full construct versus headless control in 3T3's agrees with the expected outcome as well as the published data. The full construct had lower FRET compared to the headless control, which is theoretically in a relaxed state. This suggests that cytoskeleton connection to the full construct places it until tension, stretching the peptide spring and reducing FRET in the sensor. The same experiment conducted in NBT-II cells, however, gives a completely different picture. NBT-II's appear to be under no steady state tension at all, or perhaps even under compression. The tension sensor is not currently characterized for measuring compression. This is, however, an interesting direction to expand upon the use of mini-N2G tension sensors. Further experiments indicated preliminarily that TAN lines on the nuclear membrane are under higher tension than the rest of the nuclear membrane.

While some interesting observations were made in these experiments, much could be improved upon. While the spring constant of the peptide spring has been previously measured, the FRET efficiency, rather than FRET ratio, must be used to back calculate the distance between the donor and acceptor fluorophores in order to provide an estimate of the force applied to the tension sensor. Further improvements upon experimental design may remove measurement artifacts such as those seen in the TAN line tension data, allowing for clear conclusions in future studies.

4.6 References

1. Freikamp, A., Cost, A. & Grashoff, C. The Piconewton Force Awakens : Quantifying Mechanics in Cells. *Trends Cell Biol*. xx, 1–10 (2016).

2. Grashoff, C. et al. Measuring mechanical tension across vinculin reveals regulation of focal adhesion dynamics. *Nature* 466, 263–6 (2010).

3. Meng, F., Suchyna, T. M. & Sachs, F. A fluorescence energy transfer-based mechanical stress sensor for specific proteins in situ. *FEBS J*. 275, 3072–3087 (2008).

4. Meng, F. & Sachs, F. Visualizing dynamic cytoplasmic forces with a compliance-matched FRET sensor. *J. Cell Sci*. 124, 261–269 (2011).

5. Austen, K. et al. Extracellular rigidity sensing by talin isoform-specific mechanical linkages. *Nat. Cell Biol*. 17, 1597–1606 (2015).

6. Worman, H. J., Ostlund, C. & Wang, Y. Diseases of the nuclear envelope. Cold Spring Harb. *Perspect. Biol*. 2, 1–18 (2010).

7. Wang, N., Tytell, J. D. & Ingber, D. E. Mechanotransduction at a distance: mechanically coupling the extracellular matrix with the nucleus. *Nat. Rev. Mol. Cell Biol*. 10, 75–82 (2009).

8. Crisp, M. et al. Coupling of the nucleus and cytoplasm: Role of the LINC complex. *J. Cell Biol.* 172, 41–53 (2006).

9. Haque, F. et al. SUN1 interacts with nuclear lamin A and cytoplasmic nesprins to provide a physical connection between the nuclear lamina and the cytoskeleton. *Mol. Cell. Biol*. 26, 3738–51 (2006).

10. Padmakumar, V. C. et al. The inner nuclear membrane protein Sun1 mediates the anchorage of Nesprin-2 to the nuclear envelope. *J. Cell Sci*. 118, 3419–3430 (2005).

11. Taranum, S. et al. Cytoskeletal Interactions at the Nuclear Envelope Mediated by Nesprins. *Int. J. Cell Biol*. 2012, 1–11 (2012).

12. Luxton, G. W. G., Gomes, E. R., Folker, E. S., Vintinner, E. & Gundersen, G. G. Linear arrays of nuclear envelope proteins harness retrograde actin flow for nuclear movement. *Science* 329, 956–959 (2010).

13. Arsenovic, P. T. et al. Nesprin-2G, a Component of the Nuclear LINC Complex, Is Subject to Myosin-Dependent Tension. *Biophys. J*. 110, 34–43 (2016).

14. Chen, Y., Mauldin, J. P., Day, R. N. & Periasamy, A. Characterization of spectral FRET imaging microscopy for monitoring nuclear protein interactions. *J. Microsc*. 228, 139–152 (2007).

15. Nagata, T., Uchijima, M., Yoshida, a, Kawashima, M. & Koide, Y. Codon optimization effect on translational efficiency of DNA vaccine in mammalian cells: analysis of

plasmid DNA encoding a CTL epitope derived from microorganisms. Biochem. *Biophys. Res. Commun*. 261, 445–451 (1999).

16. Webster, G., Teh, A. Y.-H. & Ma, J. K.-C. Synthetic gene design - The rationale for codon optimization and implications for molecular pharming in plants. *Biotechnol. Bioeng*. 1–34 (2016). doi:10.1002/bit.26183

17. Makoff, A. J., Oxer, M. D., Romanos, M. A., Fairweather, N. F. & Ballantine, S. Expression of tetanus toxin fragment C in E.coli: High level expression by removing rare codons. *Nucleic Acids Res*. 17, 10191–10202 (1989).

18. Marin, M. Folding at the rhythm of the rare codon beat. *Biotechnol. J*. 3, 1047–1057 (2008).

19. Komar, A. A., Lesnik, T. & Reiss, C. Synonimous codon substitution affects ribosome traffic and protein folding during in vitro translation. *FEBS Lett*. 462, 387–391 (1999).

20. Kozak, M. Interpreting cDNA sequences: some insights from studies on translation. Mamm. *Genome* 7, 563–574 (1996).

21. Kozak, M. An analysis of 5'-noncoding sequences from 699 vertebrate messenger rNAS. *Nucleic Acids Res*. 15, 8125–8148 (1987).

22. Zimmermann, T., Rietdorf, J., Girod, A., Georget, V. & Pepperkok, R. Spectral imaging and linear un-mixing enables improved FRET e⁄ciency with a novel GFP2 ^ YFP FRET pair. *FEBS Lett*. 531, 0–4 (2002).

4.7 Figures

Figure 4.1   Diagram of the 4 mini-N2G tension sensors. The tension sensor is sandwiched between the head and tail regions of N2G so that force transmitted from cytoskeleton actin filaments to the LINC complex can be measured via FRET change in the sensor. The calponin homology (CH) domain binds F-actin and the transmembrane domain anchors the constructs to the nuclear membrane. The headless controls are unable to bind F-action and are used to verify FRET changes are not artifacts in measurement.

miniN2G-RL

Headless-miniN2G-RL

miniN2G-TV

Headless-miniN2G-TV

mRuby2   mTFP1   N2G head   N2G tail

fLOV2   Venus   CH domain   Transmembrane domain

Peptide spring
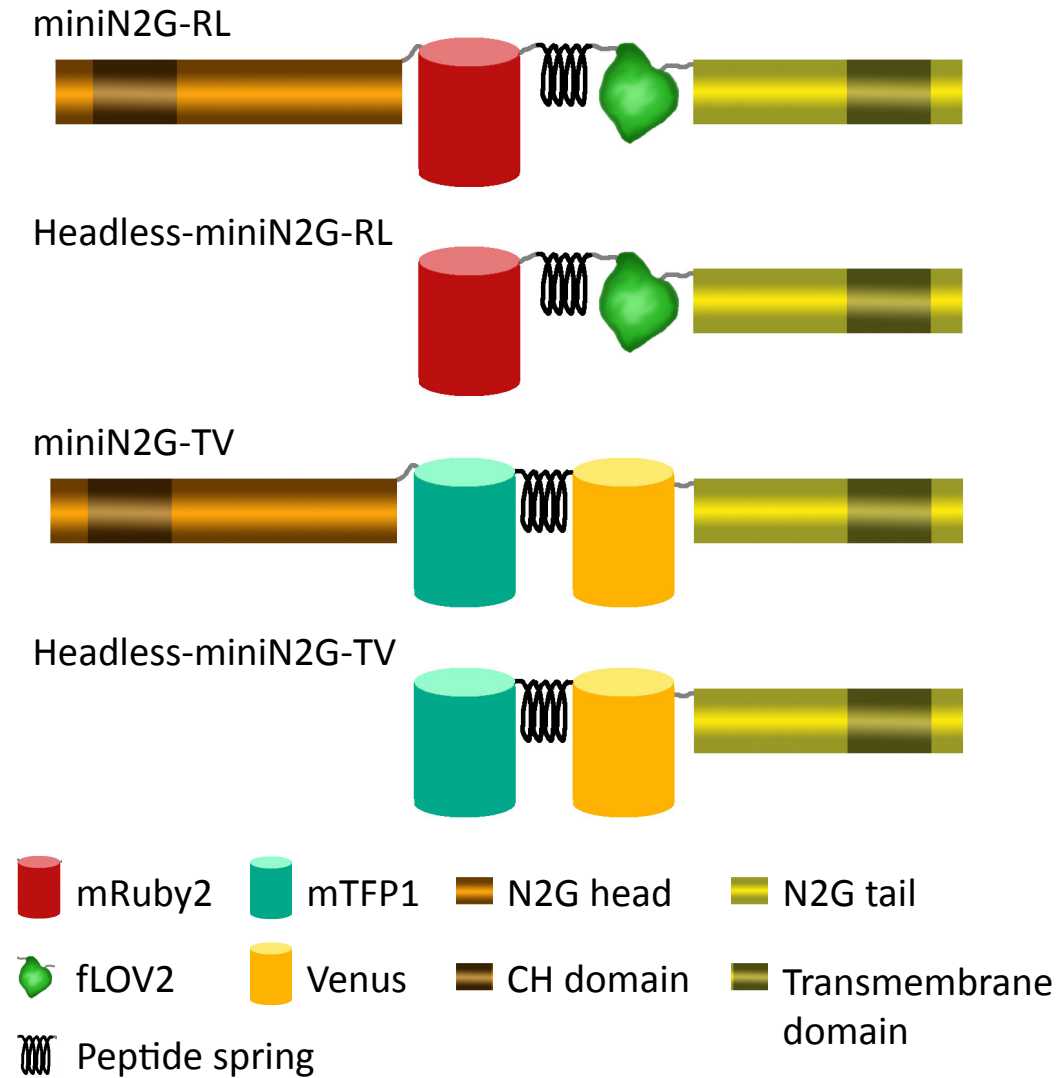
Figure 4.2 Diagrams showing the function of mini-N2G tension sensors. When under no tension, the full constructs will exhibit high FRET (a). Intracellular tension is transmitted to the tension sensor via bound F-actin. The tension stretches out the peptide spring and reduces FRET (b). The headless constructs are not attached to F-actin and exhibit high FRET regardless of tension (c).

a.   Zero force ➜ High FRET
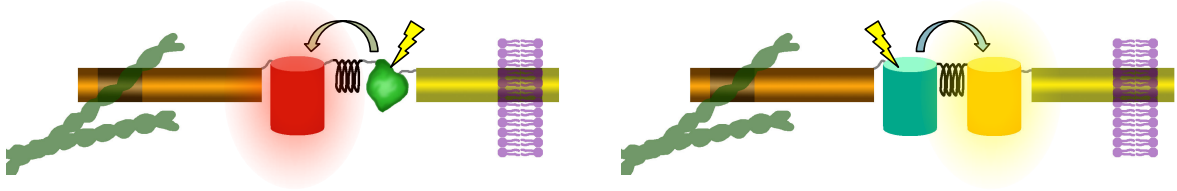
b.   Under tension ➜ Low FRET
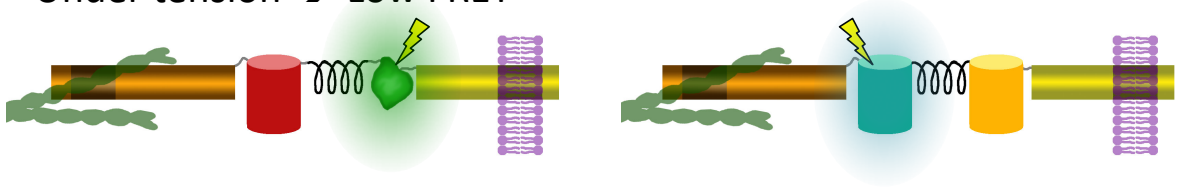
c.   Headless constructs have high FRET regardless of F-actin tension

F-actin   Nuclear membrane
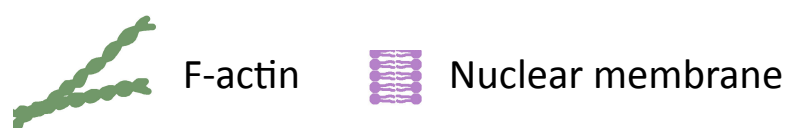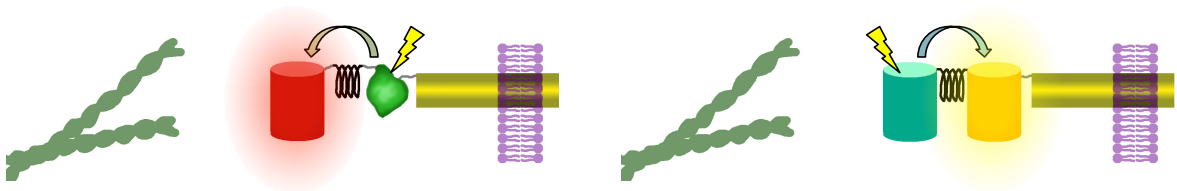
Figure 4.3   Select images in the FRET calculation process. The acceptor-only control
images are shown (a) as well as intermediates in the ASBT corrected FRET calculation
process (b).
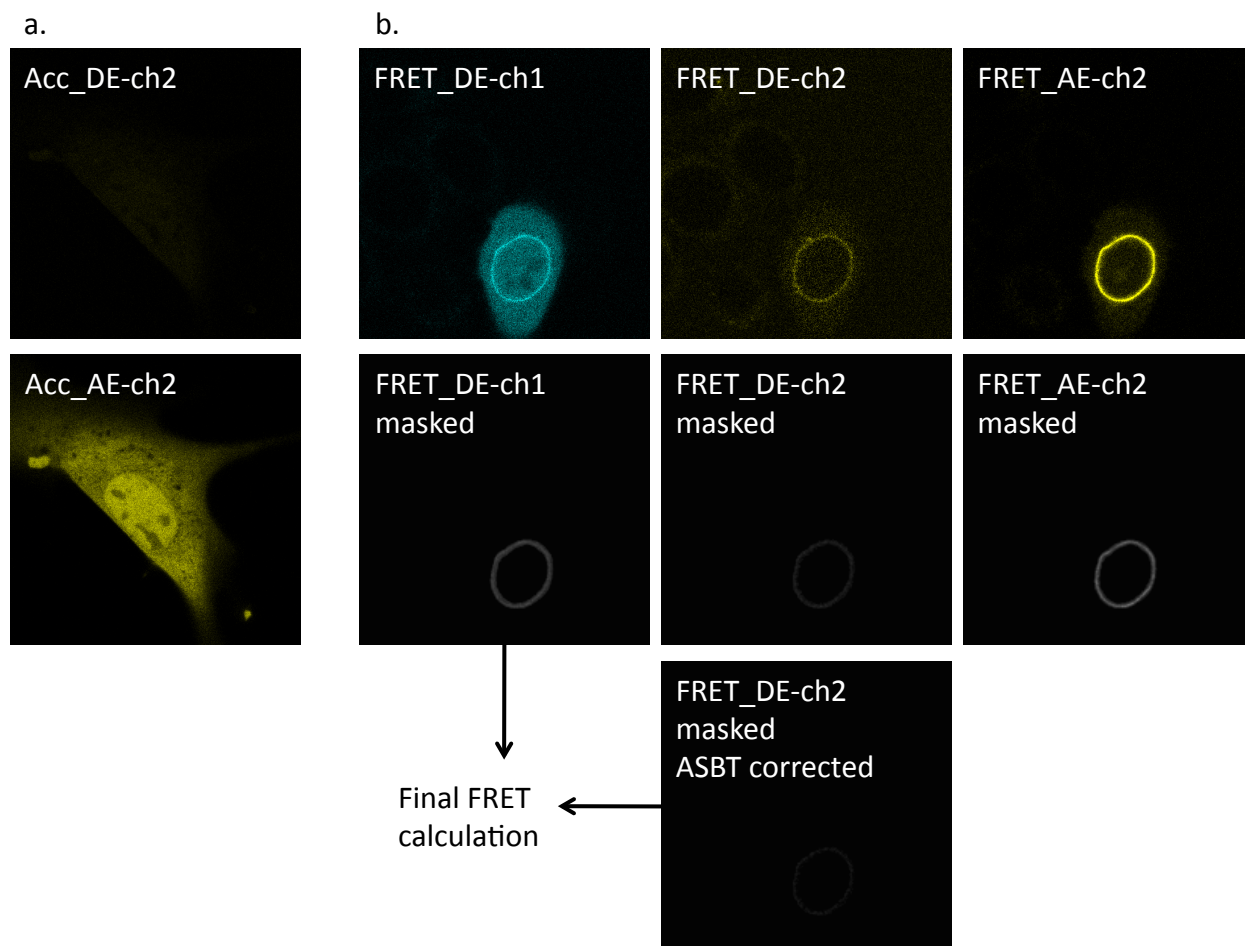
Figure 4.4   Nesprin tension sensor constructs expressed in NIH 3T3 fibroblasts. The original GFP-mini-N2G construct is shown for comparison (a). FRET sensors were imaged using both donor (left column) and acceptor (right column). The full constructs mini-N2G-RL (b+c) and mini-N2G-TV (f+g) display very little expression and no nuclear membrane localization. The headless constructs in RL (d+e) and TV (h+i) both display better expression levels compared to the full constructs as well as nuclear localization.
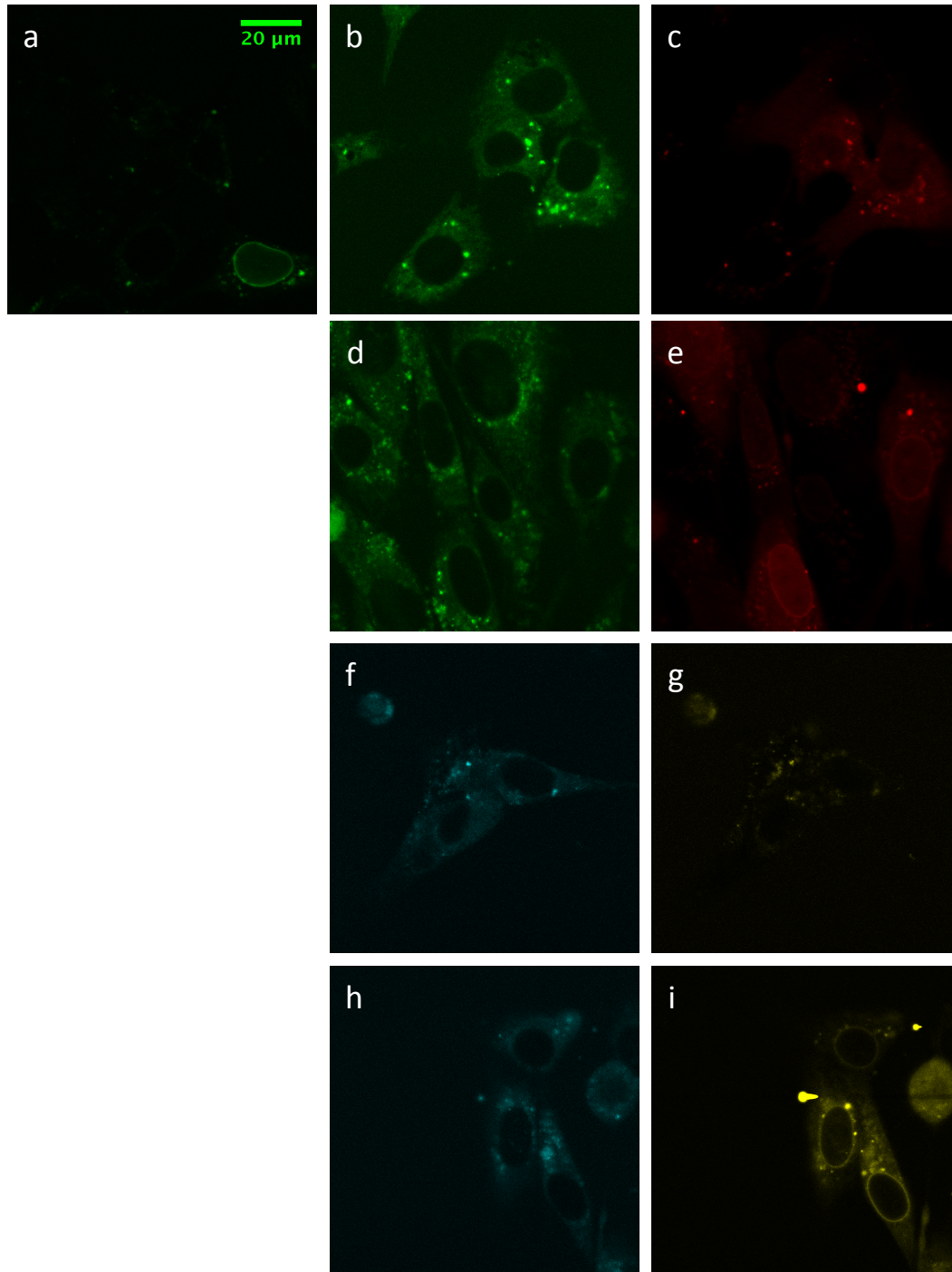
Figure 4.5   Nesprin tension sensor constructs expressed in NBT-II's. All the proteins appeared to have expressed better in NBT-II's than 3T3's, however, the relative expression and localization relationships were similar. The left side images show the donor channel and the right side images show the acceptor channel. The full constructs displayed lower expression for both the RL (a+b) and TV (e+f) versions. The headless constructs had better expression and clear nuclear localization, even more prominent than in 3T3's (c+d, g+h).
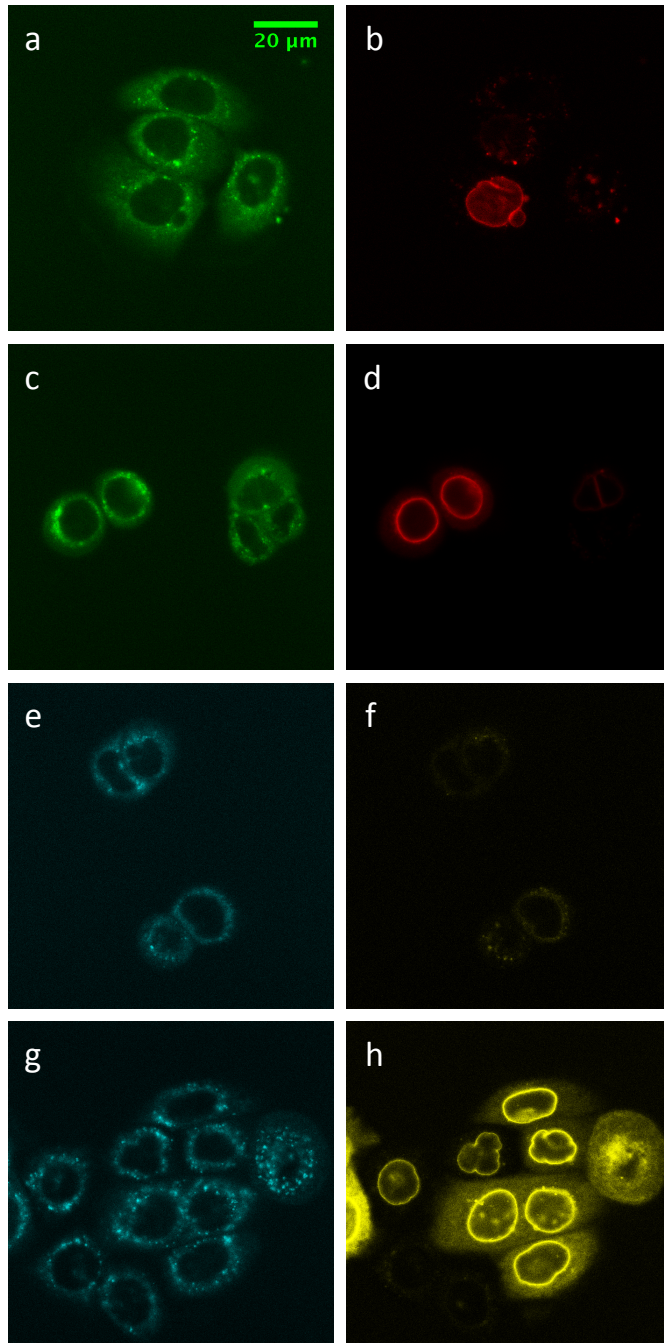
Figure 4.6   3T3's expressing codon optimized mini-N2G-RL (a+b) and headless mini-N2G-RL (c+d). Both donor channel (a+c) and acceptor channel (b+d) are shown. The codon optimization did not appear to dramatically improve expression and localization.
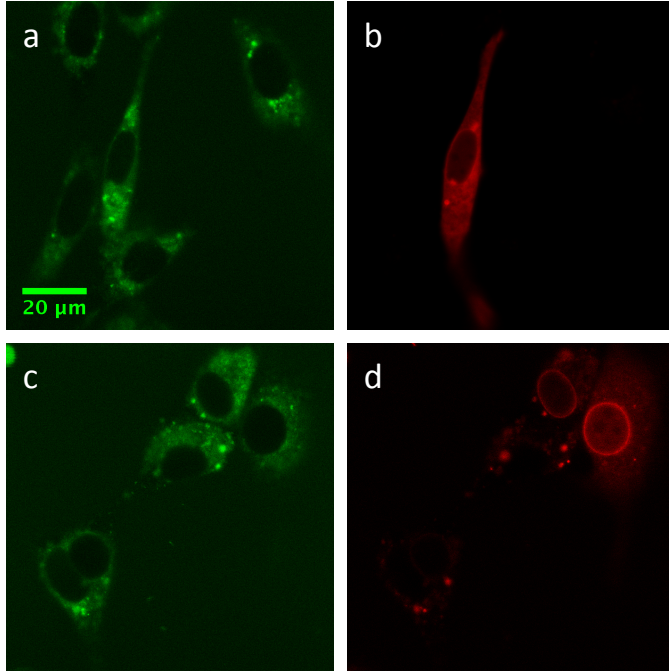
Figure 4.7 Kozak sequence improved mini-N2G-FRET constructs express and localize much better in both 3T3's (a-d) and NBT-II's (e-h). This improvement is seen in both the fLOV2/mRuby2 version (a,b,e,f) and the mTFP1/Venus version (c,d,g,h). Both donor channel (a,c,e,g) and acceptor channel (b,d,f,h) are shown.
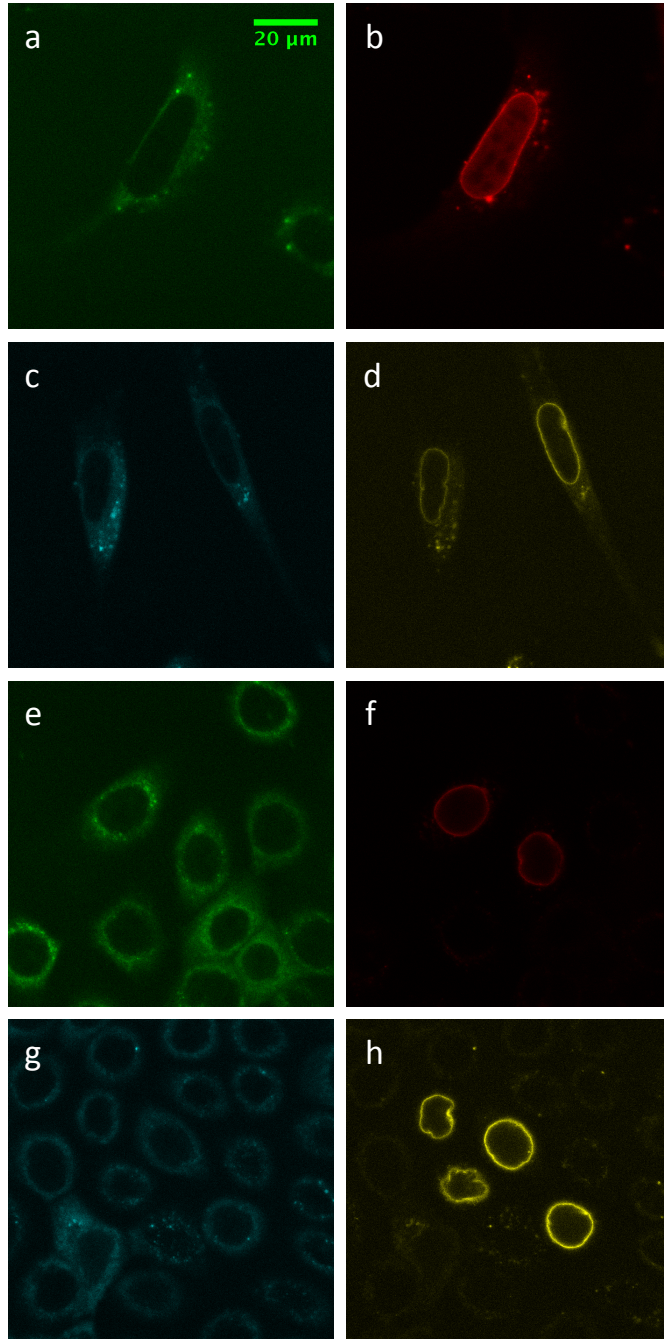
Figure 4.8 Finalized mTFP1/Venus FRET constructs expressed in both 3T3 and NBT-II cells showed clearer imaged on the Zeiss LSM 710 when imaged using spectral methods. The donor channel showed clear nuclear localization, which was not previously seen using other imaging methods. The FRET channel was also very clear.
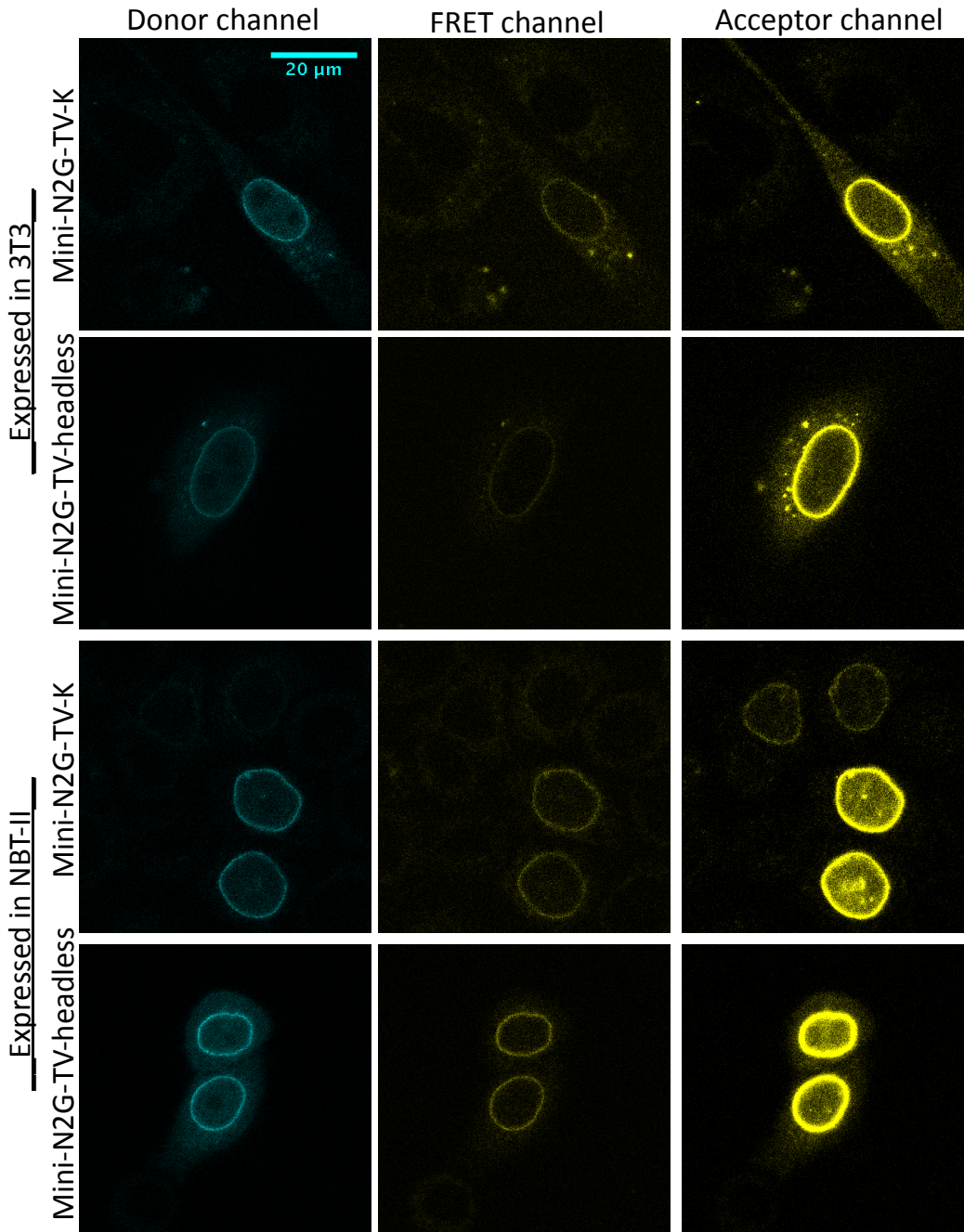
Figure 4.9   mini-N2G-TV full and headless constructs expressed in 3T3's and NBT-II's showed different results. In 3T3's, the full FRET sensor displayed lower FRET than the headless control in all experiments. Whereas, in NBT-II's, the results varied and the overall effect is inconclusive.

a

b
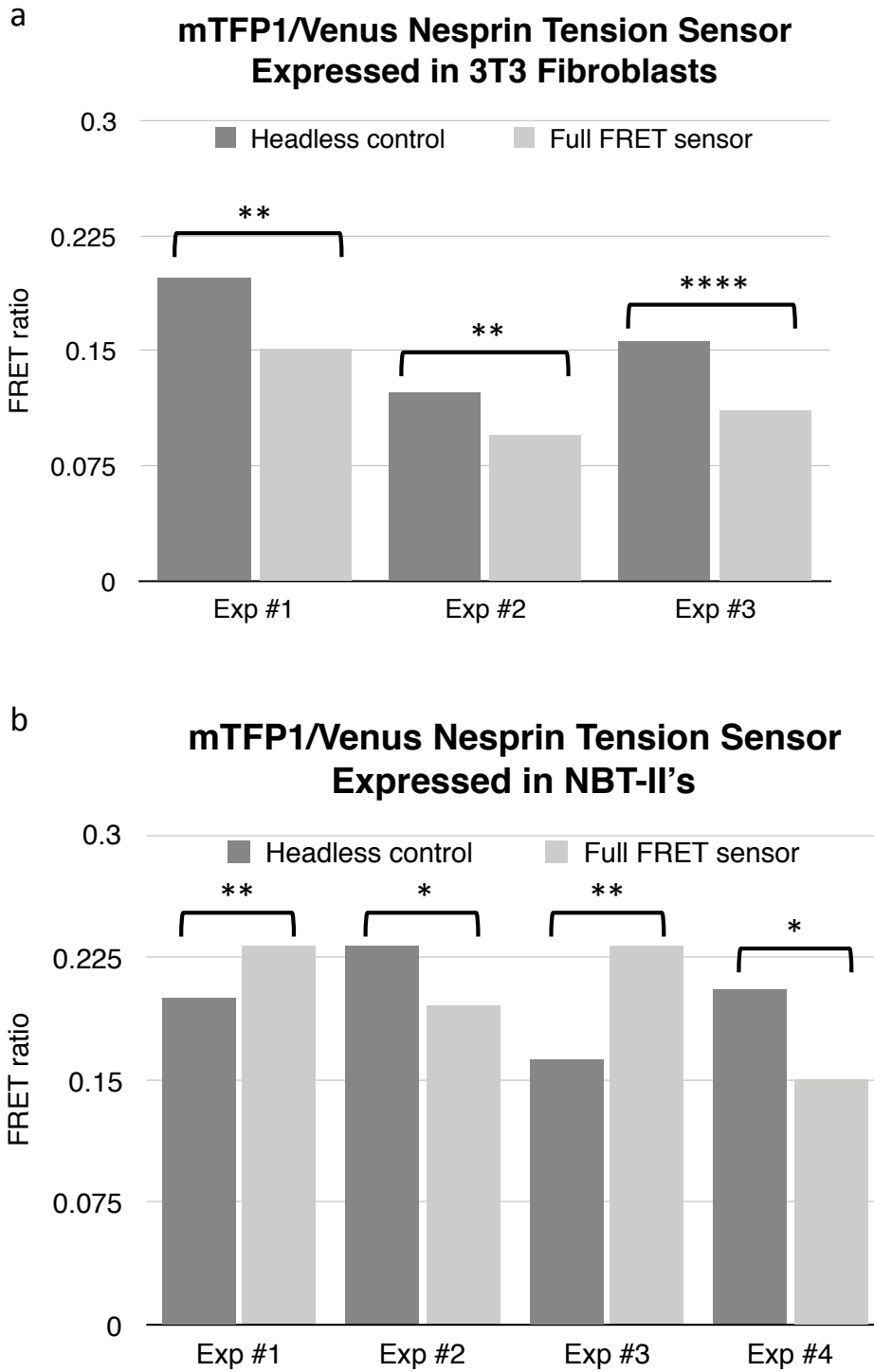
Figure 4.10   TAN line tension analysis using both FRET pairs expressed in NBT-II cells. The RL tension sensor showed lower FRET on TAN lines while its headless control displayed not statistically significant difference (a). The TV tension sensor, however, showed lower FRET in TAN lines in both the full and headless constructs (b). This may be an indication of measurement artifact. However, preliminarily, it does appear that nesprin2G is under higher tension at TAN lines as compared to other regions of the nuclear membrane.
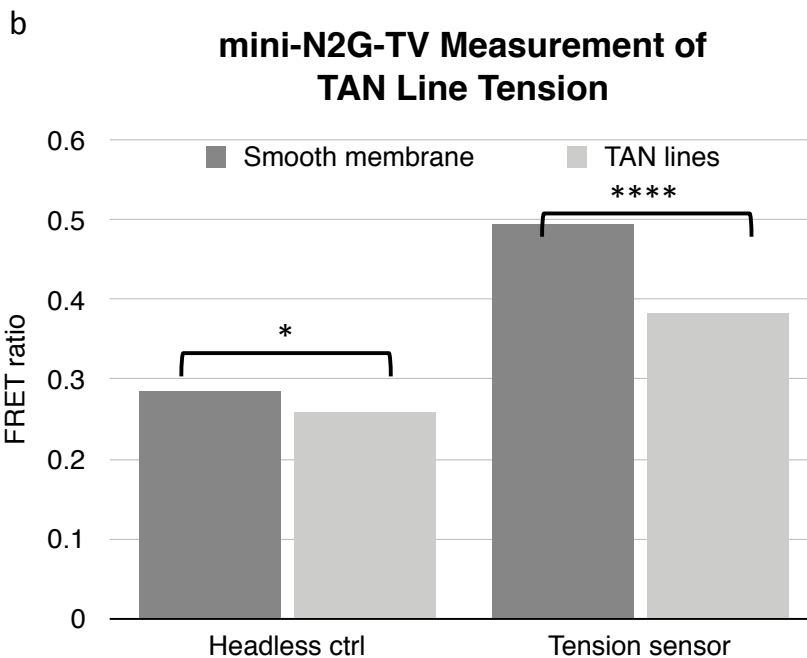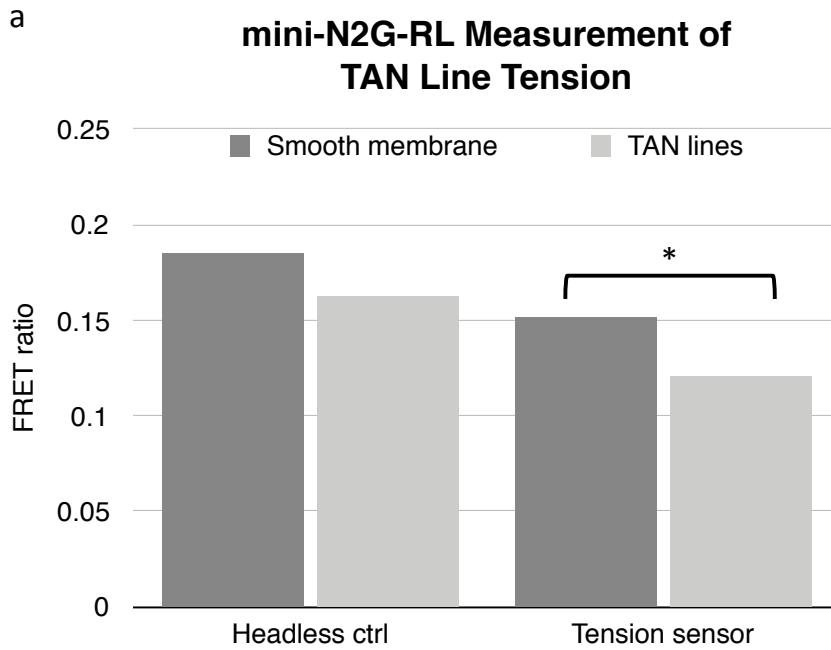
4.8 Tables

Table 4.1   Plasmid constructs used in expressing nesprin tension sensor and related protein conjugates. PL0400 VinculinTS was a gift from Martin Schwartz (Addgene plasmid # 26019).[2] PL0700 was a gift from Gregg G. Gundersen.[12]

Code	Name	Source
PL0301	mRuby2-fLOV2	See Chapter 3
PL0303	mRuby2-coil-fLOV2	See Chapter 3
PL0400	Vinculin Tension Sensor	Addgene 26019
PL0700	GFP-Mini-N2G	Gregg G. Gundersen
PL0701	Mini-N2G	PL0700
PL0702	Mini-N2G-RL	PL0701, PL0303
PL0703	Mini-N2G-TV	PL0701, PL0400
PL0704	Headless mini-N2G-RL	PL0702
PL0705	Headless mini-N2G-TV	PL0703
PL0703K	Mini-N2G-TV, +Kozak sequence	PL0703
PL0801	fLOV2	PL0301
PL0802	mRuby2	PL0301
PL0803	mTFP1	PL0400
PL0804	Venus	PL0400
PL1303a	mRuby2-coil-fLOV2 (codon optimized, STOP removed)	PL0303
PL1702	Mini-N2G-RL, codon-optimized fLOV2	PL0702, PL1303a
PL1704	Headless mini-N2G-RL, codon-optimized fLOV2	PL0704, PL1303a
PL1702K	Mini-N2G-RL, codon-optimized fLOV2, +Kozak sequence	PL1702

Table 4.2 Primers used in generating recombinant protein constructs. F and R indicate direction of binding to template. (P) indicates phosphorylation on the 5' end.

Code	Description	Sequence	Restriction Sites
PR07	mRuby2-F	ATATAGGTACCATGGTGTCTAAGGGCGA	KpnI
PR08	fLOV2-R	ATATACTCGAGTCAATCCAACTGAACCCC	XhoI
PR23	mRuby2-STOP-R	ATATACTCGAGTCACTTGTACAGCTCGTCCAT	XhoI
PR24	M-fLOV2-F	ATATAGGTACCATGGAGAAGAACTTCGTCATT	KpnI
PR40	N2Ghead-begin-F	ATATTAAGCTTATGGCTAGCCCTGTGCTGCCC	HindIII
PR41	N2Gtail-end-R	CAGTTATCTAGAcTAGGTGGGAGGTGG	XbaI
PR44	fLOV2-noSTOP-R	ATCGACTCGAGATCCAACTGAACCCCAAT	XhoI
PR45	Pre-mTFP1-F	ATCGAGGTACCGAAAAAGATGAGGTCGAG	KpnI
PR46	Post-Venus-R	ATCGACTCGAGTGCTTTCTGCTCTGGGAA	XhoI
PR47	N2Gtail-begin-F	(P)-AGTCTCGAGCTTCaCAGCAAGCTCAG	XhoI
PR48	N2Ghead-end-R	(P)-ACTGGTACCtTCCAGGAGTGGGATGAAG	KpnI
PR52	XFP-F	ATATAGGTACCATGGTGAGCAAGGGCGAGGAG	KpnI
PR53	XFP-R	ATATACTCGAGTCACCTGTACAGCTCGTCCATGC	XhoI
PR55	Codon optimized fLOV2-F	CGACTGCTAGCGAGAAGAATTTTGTCATTTGTG	NheI
PR58	Codon optimized fLOV2-noSTOP-R	CTGGACTCGAGGTCAAGCTGAACTCCTATAAAATACTG	XhoI
PR59	Kozak-N2ghead-begin-F	ATATAAAGCTTgccaccATGGCTAGCCCTGTGCTG	HindIII

Table 4.3   Fluorescence images involved in ASBT analysis. Raw images are spectral imaging data prior to linear unmixing, and unmixed images are those post-processing with channel 1 referring to the donor channel and channel 2 referring to the acceptor channel.

* Acc_DE-ch1, Acc_AE-ch1, and FRET_AE-ch1 were unmixed from raw data but contain only background noise and were not used in analysis.

† FRET_DE-ch1 was used in the calculation of ASBT itself, but was used in the final FRET analysis.

Sample	Excitation	Raw Image	Unmixed Donor	Unmixed Acceptor
Acceptor only	Donor	Acc_DE	Acc_DE-ch1*	Acc_DE-ch2
	Acceptor	Acc_AE	Acc_AE-ch1*	Acc_AE-ch2
FRET pair	Donor	FRET_DE	FRET_DE-ch1†	FRET_DE-ch2
	Acceptor	FRET_AE	FRET_AE-ch1*	FRET_AE-ch2

CHAPTER 5

Current Conclusions and Looking Forward

5.1 Conclusions

This dissertation explored the development of several imaging tools in the service of studying cellular mechanotransduction *in vitro*, both external and internal to the cell itself.

Chapter 2 reframed a small molecule biophotonic imaging tool in the form of a polymer crosslinker. Taking advantage of its unique photoswitching capabilities, NISO was placed in the context of the physical environment of *in vitro* cell culture. As a molecule that changes both conformation and optical properties, NISO crosslinker is able to both effect a change in bulk material stiffness as well as reflect this change in a visual manner via its color and absorption transformation in the MC state. In this chapter, it was established that, when crosslinked into either PMA or PA polymers, NISO switching leads to measurable stiffness decrease in the MC state as compared to base stiffness.

Furthermore, NISO is versatile in the types of functional groups it can use. While this chapter only explored the use of maleimide and methacrylate functional groups, it is possible and quite simple to attach a variety of different reactive groups for different purposes. NISO-crosslinked hydrogel displayed no negative effect on cell health, and the photoswitching process, when controlled, is not damaging to cells.

Chapter 3 explored a more basic tool that can be applied in a variety of different ways. A novel FRET pair was formed between fLOV2 and mRuby2 with photophysical properties comparable to many presently available FRET pairs with the added advantage of fLOV2 being a much smaller protein. While more characterization remains to be conducted, this FRET pair shows much promise.

Chapter 4 looked into developing a specific tension sensor for the purposes of studying physical force transmission from the cytoskelton to the nucleoskeleton. The mini-N2G-FRET sensor was designed and developed using both the previously published FRET pair of mTFP1/Venus and the currently under development FRET pair fLOV2/mRuby2. At the time of development, another research group published the same tension sensor construct with mTFP1/Venus. While ideas converged on these fronts, the application of fLOV2/mRuby2 remains novel. It remains to be seen, however, if it holds any advantages in this specific FRET sensor. Preliminary data showed that the FRET sensor was able to sense tension in nesprin 2G as compared to the unbound control constructs. Further study indicated possible higher tension in N2G at the location of TAN lines on the nuclear membrane.

5.2 Looking Forward

Each chapter of this thesis has focused on a different aspect of developing *in vitro* tools and platforms for investigating cellular mechanotransduction. Whilel promising, each tool still has a long way to go before it is fully fleshed out and functional.

Looking forward, there is much to consider for the future directions of these projects. NISO properties must be fully characterized to bring a convergence upon its optical and physical switch properties. With these studies complete, it still remains to be seen the exact effect of NISO switching on the behavior of cells.

As it applies to the FRET pair and the FRET sensors, both also require further characterization. A full 3D model of interactions between the donor and acceptor would dramatically improve understanding of its properties and lay out possible ways to improve their coupling and energy transfer efficiency. At the same time, the nesprin FRET sensor would greatly benefit from simultaneous measurements of mechanotranduction pathway activity both in the cytoskeleton and within the nucleus. Perhaps this is reason to develop more activity sensors, specifically for interactions such as those between the LINC complex and the lamin network supporting much of the nuclear structure. The next step is to step into the nucleus.